UNIVERSITÉ PARIS XI
U.F.R. SCIENTIFIQUE D'ORSAY

Habilitation à Diriger des Recherches

soutenue le

jeudi 10 décembre 2015

par Sébastien Procureur

Micromegas: a tracking detector for high energy physics and beyond

Président du jury:	Étienne Augé
Rapporteur:	Denis Bernard
Rapporteur:	Amos Breskin
Rapporteur:	Rob Veenhof
Examinateur:	Ioannis Giomataris
Examinateur:	Fabio Sauli
Invitée:	Héloïse Goutte

Le savant est d'un naturel étroit. Dans l'esprit du savant un coin seulement est éclairé, épaisses ténèbres partout ailleurs. Au fond de ces hommes utiles et spéciaux il y a presque toujours une antipathie incurable pour toutes les choses de sentiment, d'imagination, de foi, de poésie, d'art, de religion, c'est-à-dire pour tout le grand côté de l'humanité. Questionnez Laplace sur Mozart, Cuvier sur Raphaël, Arago sur Virgile, tous sur Jésus-Christ, et vous verrez quelle barbarie ! Dans l'intelligence limitée de l'homme, la science d'une chose n'est souvent que l'ignorance profonde de tout le reste.

Victor Hugo

Contents

Preamble **v**

1 Introduction to the Micromegas detector **1**

1.1 Ionization 2

1.2 Diffusion and drift 6

1.2.1 Presence of electric and magnetic fields 7

1.3 Amplification and signal formation 10

1.3.1 Gain and first Townsend coefficient 11

1.3.2 Gain fluctuations 12

1.3.3 Signal formation 13

1.4 Choice of the gas mixture 14

2 Characterization and performance of Micromegas **17**

2.1 Manufacturing 17

2.1.1 The Printed Circuit Board 17

2.1.2 The bulk technology and the micro-mesh 18

2.1.3 The resistive film 20

2.1.4 Material budget 20

2.2 Integration 21

2.2.1 High voltage and cooking 21

2.2.2 Gas circulation 22

2.3 Readout electronics 23

2.3.1 General principles 23

2.3.2 Electronics for large capacitance: the Clas12/Dream readout system 26

2.4 Characterization and performance of standard detectors 28

2.4.1 Gain measurement 28

2.4.2 Electron transparency 31

2.4.3 Energy resolution 32

2.4.4 Efficiency 32

2.4.5 Spatial resolution 34

2.4.6 Time resolution 35

2.5 Specific performance of resistive Micromegas 37

2.5.1 Gain and efficiency 37

2.5.2 Ageing and high fluxes 38

2.5.3 Effects of dust 39

2.5.4 Time resolution 41

3 Elements of tracking and reconstruction 43

3.1 Introduction to tracking 43

3.2 Track finding 44

3.2.1 Local methods 44

3.2.2 Global methods - example of the Hough transform 45

3.3 Track fitting 46

3.3.1 The Least Squares Method 46

3.3.2 The Kalman Filter 48

3.3.3 Recent developments 51

3.4 Tracking performance 52

3.4.1 Tracking resolutions 52

3.4.2 Effect of the background 54

3.4.3 Misalignments 55

3.5 Event reconstruction 57

3.5.1 Vertexing 57

3.5.2 Physics analysis 59

4 Micromegas and discharges 61

4.1 Introduction to discharges and breakdown 61

4.1.1 The Paschen law 61

4.1.2 The second Townsend coefficient and generation mechanism 62

4.1.3 The streamer mechanism and the Raether limit 63

4.2 Discharges in Micromegas 64

4.2.1 Manifestation and consequences 64

4.2.2 Past measurements 65

4.3 Simulation of discharges in hadron beams 67

4.3.1 A Geant4-based model 67

4.3.2 Large energy deposits and discharges 68

4.3.3 Effect of the gas and detector materials 69

4.4 Recent discharge rate measurements and simulation 71

4.4.1 Effect of the beam energy and type 71

4.4.2 Effect of an external magnetic field 73

4.4.3 Effect of an additional GEM foil 77

4.4.4 From the Raether limit to a charge density limit 78

4.4.5 Comparison with data 78

4.5 Reduction of discharge effects 79

4.5.1 Reduction of voltage drop through individual strip polarization . . 80

4.5.2 Reduction of reloading time through optimization of the filter components 81

4.5.3 Micro-mesh segmentation 82

4.5.4 Resistive technologies 83

5 Micromegas with genetic multiplexing 85

5.1 Introduction 85

5.2 Principle of multiplexing 85
    5.2.1 Double sided multiplexing 86
    5.2.2 Genetic multiplexing 88
    5.2.3 2D multiplexing 92
5.3 Characterization of prototypes 93
    5.3.1 1D prototype 93
    5.3.2 2D prototypes 94
5.4 Applications to muon tomography 97
    5.4.1 Principles of muon tomography 97
    5.4.2 Selected applications and simulation 98

Preamble

The scientific goal of this document is to provide an introduction to the Micromegas-based trackers used nowadays in physics. Apart from the second one, each chapter is a little more general, and will hopefully trigger the interest of a wider community — related to gaseous detectors, tracking, discharges or muon tomography. The variety of topics covered in this document originates from my somehow random journey in physics, which is evidently the fate of any scientist. In October 2006 I joined the famous CEA/DSM/Dapnia/SPhN/Clas group, known today as the CEA/DRF/Irfu/SPhN/LSN laboratory, to study the feasibility of a cylindrical Micromegas vertex tracker for the Hall B spectrometer of JLab. The project combined many new challenges which had to be addressed: first curved detectors, low radiation length, operation in 5 T magnetic field, use of 2 m long cables for the remote electronics and very high luminosity. My first task was to develop simulation tools based on Garfield and Geant4 to quantify the benefits of the Micromegas option with respect to the Silicon tracker. In parallel, many prototypes were built and characterized at lab to check the performance of curved detectors. The issue of the Lorentz angle in strong magnetic fields being of particular interest, we conducted several tests in Building 392 and at JLab with a UV laser which confirmed Magboltz predictions up to 4.2 T field. In 2008 I spent 11 months at JLab to develop a tracking code for charged particle reconstruction in the future Clas12 spectrometer. Several examples of algorithms used in this code are described in Chapter 3. By interfacing this code with several Monte Carlo generators and Geant4, I then validated the performance required by the physics case, optimized the design of several detectors (Silicons, Micromegas, Drift Chambers) and proved the tracking feasibility for luminosities beyond the nominal one. I cannot mention this period without expressing my gratitude to Maurizio Ungaro and Mac Mestayer for their support and for the pleasure I had to work with them.

Back at Saclay in 2009 I developed detailed Geant4 simulations on the interactions of particles with Micromegas. I showed in particular that beam discharges in this detector originate from the production of Highly Ionizing Particles through the nuclear interaction of hadrons with the detector's components (see chapter 4). We then organized three beam tests at Cern/SPS, JLab and Cern/PS to validate this model with different detector geometries, materials as well as different beam types and energies. Meanwhile I extended the validity of this model by taking into account the transverse diffusion of charges to define a surface charge density limit, which quantitatively explained the discharge reduction with GEM foils.

In 2012, while working on the large Clas12 cosmic bench at Sedi, I introduced with R. Dupré and S. Aune the so-called *genetic multiplexing* to reduce the size of electronics readout (see Chapter 5). The first prototype of 1024 strips was thus readout with only 61 channels of a single connector. Following the precious advice of É. Delagnes, I started to investigate applications of this technique for muon tomography. A first grant was obtained in September 2013 within the NRBC-E program to develop a muon scanner for containers to detect contraband materials (M-Cube project). With the unvaluable help of I. Mandjavidze and D. Attié, the prototypes as well as the electronic configuration were improved to reach efficiencies above 95% in 2D. In 2014 I proposed to build a muon telescope based on these detectors, with the goal to join the Diaphane collaboration on volcanology. The telescope was built and successfully tested in 2015 on the Saclay water tower, and triggered the interest of several industrials for potential applications in soil imaging. Today other applications are emerging, in particular for archeology (tumulus, pyramids) and for civil engineering using muon metrology. In parallel, the know-how transfer initiated with the Elvia company several years ago at Irfu was continued within the M-Cube project, and first multiplexed detectors were delivered in December 2015. For sure, the best is still to come...

Je termine ce préambule dans ma langue pour remercier chaleureusement tous mes collègues avec qui j'ai le plaisir d'interagir, à l'Irfu ou ailleurs. Citer des noms est un exercice trop périlleux auquel je ne me risquerai pas, tant la liste serait longue et les oublis inévitables. Je tiens aussi à exprimer toute ma gratitude aux membres de l'éminent jury pour l'honneur qu'ils m'ont fait et pour les corrections qu'ils ont apportés au présent document. Je te remercie enfin, toi qui lis ces lignes (si tu existes), et te souhaite une bonne lecture!

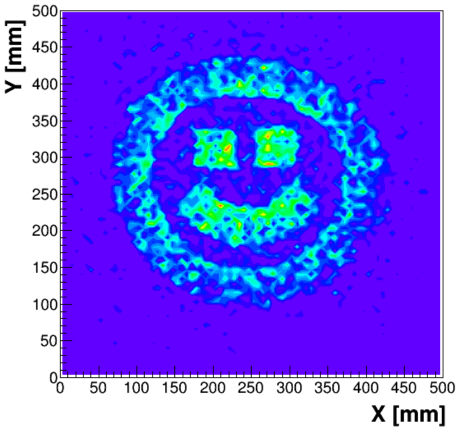

Chapter 1

Introduction to the Micromegas detector

As other MPGDs, the Micromegas (MICRO-MEsh GAseous Structure) [1, 2] has been designed to stand the very high fluxes of modern particle and nuclear physics. This requires a fast evacuation of the charges in the gas volume and therefore a reduction of their drift paths to a few tens of microns. The solution implemented in the Micromegas consists in separating the ionization and the amplification regions by a metallic micro-mesh, as depicted in Fig. 1.1 (left). Primary electrons produced in the ionization of the gas by an incident particle will drift in a moderate electric field. In the vicinity of the micro-mesh, electrons are sucked in the holes due to the strong electric field in the amplification region. This funnel effect is visible from the field lines shown in Fig. 1.1 (right). Once in the amplification gap, electrons are accelerated and gain enough energy between two collisions to further ionize the gas. An avalanche process is initiated, with the creation of thousands of electron-ion pairs. The electrons are collected in a few ns in the anode plane, while the ions slowly drift back to the micro-mesh, both inducing a signal on the readout electronics. Because of the field asymmetry, the vast majority of the upcoming ions doesn't experience the funnel effect as primary electrons do, and is collected by the micro-mesh. Up to a usually negligible fraction of ions drifting back to the ionization region, the charge evacuation time is then determined by the drift time of ions in the amplification gap, typically 100 ns. This allows for safe operation in particularly high flux, up to 450 kHz/cm^2 in current experiments.

Apart from the fast evacuation of ions, a small amplification gap also permits to achieve larger electric fields through the Paschen law, and then larger gains. As an illustration, a 128-micron gap in air can routinely stand high voltages up to 850 V, resulting in a 65 kV/cm field. This should be compared with the dielectric strength of 36 kV/cm usually quoted in the study of electric storms.

In the next sections we will review the different physical process at work from the ionization of the gas to the formation of the signal on the readout elements. Most of these principles are common to all types of gaseous detectors, and more details can be found in the abundant existing literature [3].

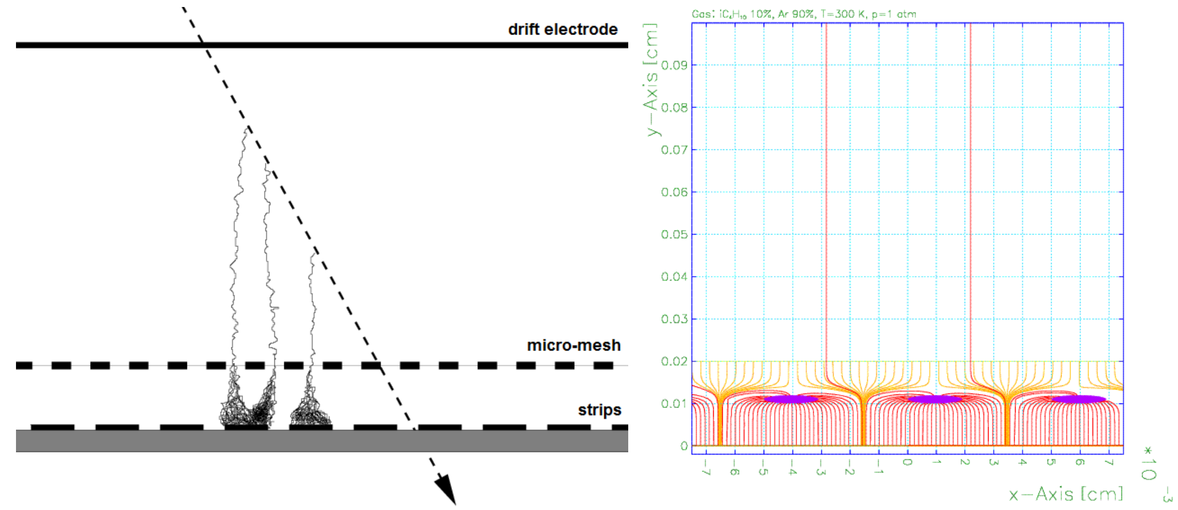

Figure 1.1: *(Left): basic principle of the Micromegas detector, with the charged incoming particle (arrow), primary electrons, and the avalanche process. (Right): illustration of the funnel effect with the electron field lines (yellow) in the vicinity of the micro-mesh (purple).*

1.1 Ionization

The detection of particles usually relies on the creation of electron-ion pairs in the gas, a process called ionization. Primary ionization results from the electromagnetic interaction of an incoming particle with the gas:

$$particle + A \rightarrow particle + A^{+} + e^{-}, particle + A^{++} + 2e^{-}, etc. \tag{1.1}$$

These processes are random and uncorrelated, which means that the number of primary ionizing interactions over a path L follows a **Poisson law**:

$$P(X = k) = \frac{(n)^k}{k!} e^{-n}, \tag{1.2}$$

where n is the mean value, usually expressed in terms of the mean free path λ of the particle in the gas or in terms of the mean number of primary ionizations per unit length N_p:

$$n = \frac{L}{\lambda} = N_p L \tag{1.3}$$

They both depend on the particle velocity and on the gas nature, as shown in Table 1.1 for N_p.
An important consequence of Eq. (1.2) is that a gaseous detector has an intrinsic inefficiency corresponding to the probability e^{-n} that no ionization occurs ($k = 0$). For a 3 mm conversion gap Micromegas, this probability yields only 0.1% in Argon but 2.7% in Neon, and should therefore be taken into account in the design of the detector.
The electrons created in the primary ionizations may have enough energy to further ionize

the gas, increasing the total number of charges left in the vicinity of the incoming particle. The distribution of the total number of pairs and its mean value strongly determine the detector performance, and in particular its efficiency and energy resolution. A complete calculation of this distribution from first principles would require an exact treatment of all quantum transitions between atomic shells as well as of the local field modifications of the polarizable medium, and is nearly an impossible task. However, intense studies started in the early XXth century led to the development of more and more refined models which are now in good agreement with measurements and provide a solid understanding of the mechanisms at work.

The first major piece of this work was brought by Bethe who derived in 1930 a quantum mechanical expression for the average energy loss of an incoming charged heavy particle interacting with an atom [4]. In 1932 he extended this expression for relativistic particles [5], leading to the well-known **Bethe-Bloch equation** valid in any material:

$$-\langle\frac{dE}{dx}\rangle = 4\pi N_A r_e^2 m_e c^2 z^2 \rho \frac{Z}{A}\frac{1}{\beta^2}\left(\frac{1}{2}\ln\frac{2m_e c^2\beta^2\gamma^2 T_{max}}{I^2} - \beta^2 - \frac{\delta(\beta\gamma)}{2}\right), \tag{1.4}$$

with notations as defined in [6]. This formula exhibits in particular a minimum around $\beta\gamma \approx 3$ corresponding to Minimum Ionizing Particles (MIPs).

Though widely used in experimental physics, the Bethe-Bloch equation suffers from two drawbacks in the context of ionization:

- it provides only a mean value, giving no information on potential fluctuations;
- it gives the total energy loss without separating the different contributions.

As an illustration of the latter, the energy loss for a MIP in 1 cm Argon yields 3 keV according to Eq. (1.4). The ionization energy of Argon being 15.76 eV, one can expect about 150 electron-ion pairs, a value far above measurements. The difference results from other processes which contribute to the energy loss, and in particular excitations:

$$particle + A \rightarrow particle + A^* \tag{1.5}$$

Many excitation energy levels being lower than the ionization ones, this process does not necessarily lead to ionization. In practice this problem is overcome by introducing a mean ionization energy, w_i:

$$n_t = N_t L = \frac{\Delta E}{w_i}, \tag{1.6}$$

where n_t is the mean total number of electron-ion pairs, N_t being normalized to unit length similarly to N_p, and ΔE the mean energy loss. By construction, w_i is higher than the ionization potential, see Table 1.1. Though this formulation hides many interaction mechanisms at the microscopic level, the practical interest of w_i lies in its large independence on the energy and type of the incoming particle. Its knowledge for a given material combined with the Bethe-Bloch equation is therefore usually enough to estimate the mean number of electron-ion pairs.

gas	density (g/L)	E_x (eV)	E_i (eV)	w_i (eV)	N_p	N_t	dE/dx_{MIP} (keV/cm)
Ne	0.839	16.62	21.56	36	12	43	1.56
Ar	1.662	11.55	15.76	26	23	94	2.44
Xe	5.483	8.31	12.13	22	44	307	6.76
iC_4H_{10}	2.51	6.5	10.57	23	84	195	5.93
CF_4	3.72	10.0	16.23	54	51	100	7.0
CH_4	0.667	8.8	12.61	27	25	53	1.48
CO_2	1.84	7.0	13.78	33	35.5	91	3.01
C_2H_6	1.263	8.2	11.50	26	41	111	1.15

Table 1.1: *Compilation of physical properties of some gases at NTP frequently used in Micromegas.*

The problem of fluctuations in the ionization energy loss was first investigated by Landau in 1944 [7]. To simultaneously avoid the treatment of all atomic shell structures and use Rutherford scattering on free electrons, he considered only the case where the energy loss is large compared to the binding energy of electrons. His expression for the energy loss distribution, known as the Landau function, exhibits a very long tail[1] which corresponds to the production of high energy electrons in the medium, called δ electrons. Though the Landau model is in fair agreement in some cases with gases, the main assumption on large energy loss makes its validity doubtful for gaseous detectors.

Important progress have been made in the 1970s to refine ionization models for small energy losses, in particular by taking into account the atomic shell structures [8] and the dielectric constant of the medium. The former naturally led to describe the interaction in terms of virtual photon exchange. It culminated in 1980 with the development of the **Photo-Absorption Ionization model** (PAI) in which the photo-absorption cross section for virtual photons is linked to the real photon one. The PAI model provides the full computation of the differential cross section for the energy transfer E in the collision of the incoming particle with atoms, as a function of the photo-absorption cross section $\sigma_\gamma(E)$ [9]:

$$\begin{aligned}\frac{\beta^2\pi}{\alpha}\frac{d\sigma}{dE} &= \frac{\sigma_\gamma(E)}{EZ}\ln\left(\frac{1}{\sqrt{(1-\beta^2\epsilon_1)^2+\beta^4\epsilon_2^2}}\right)+\frac{1}{N\hbar c}\left(\beta^2-\frac{\epsilon_1}{|\epsilon|^2}\right)\theta \\ &+\frac{\sigma_\gamma(E)}{EZ}\ln\left(\frac{2mc^2\beta^2}{E}\right)+\frac{1}{E^2}\int_0^E\frac{\sigma_\gamma(E')}{Z}dE',\end{aligned}\tag{1.7}$$

where ϵ=ϵ_1+iϵ_2 is the complex dielectric constant and:

$$\theta = arg\left(1-\epsilon_1\beta^2+i\epsilon_2\beta^2\right)\tag{1.8}$$

The PAI cross section is illustrated in Fig. 1.2. It turns out that all the atomic shells contribute to the final ionization yield, the low probability of inner shell interactions being compensated by the higher number of secondary electrons.

The clear advantage of this formulation is that the atomic shell structure is absorbed

---

[1] originating from the $1/E^2$ dependence of the Rutherford cross section

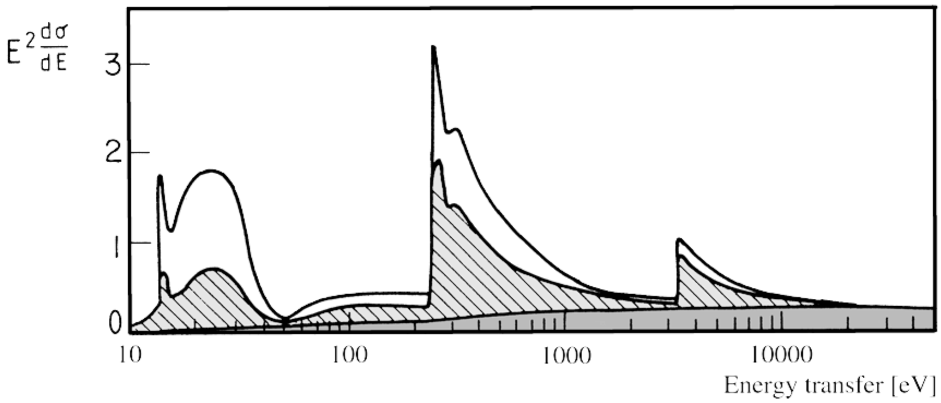

Figure 1.2: *Differential cross section from the PAI model, derived from [9], with the contribution of the different terms of Eq. (1.7). The peaks corresponding to M, L and K shells respectively appear clearly.*

in $\sigma_\gamma(E)$ which is relatively well known through numerous measurements. The final distribution of the ionization energy loss can then be accessed by convoluting the Poisson distribution for primary collisions and the differential probability obtained from the energy transfer cross section. The cross section input and the process separation induced by the PAI model also make it particularly suitable for Monte Carlo techniques, and led to the development of the **Heed** [2] program by I. B. Smirnov [10]. Heed contains in particular a large database of the measured photo-absorption cross sections for a large variety of gases, and uses an approximate shell-dependent reformulation of Eq. (1.7). The relaxation of excited atoms is also implemented through the emission of fluorescent photons and Auger electrons [11] (auto-ionization). As can be seen in Fig. 1.3, both PAI model and Heed are in very good agreement with the experimental data.

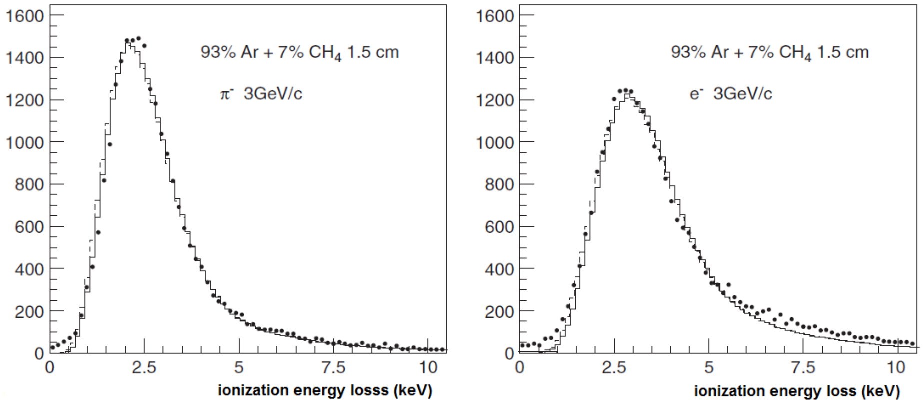

Figure 1.3: *Comparison of the ionization energy loss distribution between measurements (dots), the PAI model (dashed lines) and the Heed simulation (lines) for pions (left) and electrons (right) [10].*

In the case of a gas mixture, the mean number and the distribution of primary collisions

---

[2] High-Energy Electro-Dynamics

is deduced from separate gas elements thanks to the additivity of the Poisson law. But if an excitation energy E_x of one element is higher than the ionization energy E_i of another, an effective transfer can take place through reactions of the type:

$$\begin{aligned} &A^\star + B \rightarrow A + B^+ + e^- \\ &A^\star - > A + \gamma ; B + \gamma - > B^+ + e^- \end{aligned} \tag{1.9}$$

This transfer, called the **Penning effect** or the **Jesse-Sadauskis effect** [12, 13, 14], can slighly increase the ionization yield of the gas mixture, even at small concentrations of B. For this reason, the mean ionization energy w of a mixture cannot be simply inferred from individual w_i values. As an illustration, a (96.5-3.5%) Argon-Ethane mixture has a w value of 24.4 eV, compared to 26 eV for both components.

1.2 Diffusion and drift

In the absence of an electric field in the ionization volume, a significant fraction of the created electron-ion pairs will be lost by neutralizing each other, in reactions like:

$$\begin{aligned} &A^+ + e^- \rightarrow A^* + h\nu(radiative) \\ &A^+ + e^- + B \rightarrow A + B(three - body) \end{aligned} \tag{1.10}$$

The rate of the charge density decrease is proportional to the product of the charge densities n_+ and n_- via the so-called **recombination coefficient** R:

$$\frac{dn_+}{dt} = \frac{dn_-}{dt} = -Rn_+n_- \tag{1.11}$$

In many cases $n_+ = n_- = n$, providing a practical relation for experimental measurement of R:

$$R = \frac{d}{dt}\left(\frac{1}{n}\right) \tag{1.12}$$

Electrons can also form negative ions through collisions with atoms. This process is characterized by the **attachment coefficient** h, defined as the probability to form such a negative ion in a collision. The value of h strongly depends on the electron affinity of a given gas. It is minimal for noble gases because of their full valence shell, making them ideal candidates for gaseous detectors. On the other hand, air and water vapor have large attachment coefficient [15, 16], and concentrations as small as a few ppm can significantly degrade the charge collection, even in the presence of a strong electric field.
The velocity distribution of the remaining charges is given by the Maxwell-Boltzmann statistics [17]:

$$f(v) = 4\pi\left(\frac{m}{2\pi kT}\right)^{3/2} v^2 e^{-\frac{mv^2}{2kT}}, \tag{1.13}$$

resulting in the mean velocity:

$$\bar{v} = \int_0^\infty v f(v)\,\mathrm{d}v = \sqrt{\frac{8kT}{\pi m}} \tag{1.14}$$

This expression shows that electrons have a much higher velocity than ions in gases. However, it should be emphasized that the mean drift velocity in a given direction is zero when no electric field is applied.
Finally, charge density n evolution is given by the classic equation:

$$-\frac{\partial}{\partial t}n + D\Delta n = 0, \tag{1.15}$$

where D is the **diffusion coefficient**. It follows that charges undergo an isotropic diffusion following a Gaussian law whose width in a given direction is $\sigma_x{=}\sqrt{2Dt}$. As an illustration, the diffusion yields around 2 mm in 1 s for oxygen ions in air.

1.2.1 Presence of electric and magnetic fields

Macroscopic picture

The drift of charges in gases in the presence of E and B can be described by the **Langevin equation** [18]:

$$m\frac{\mathrm{d}\overrightarrow{v_D}}{\mathrm{d}t} = e\overrightarrow{E} + e\left(\overrightarrow{v_D} \times \overrightarrow{B}\right) - \frac{m\overrightarrow{v_D}}{\tau} \tag{1.16}$$

where the friction term $-\frac{m\overrightarrow{v_D}}{\tau}$ effectively accounts for collisions in the gas occuring at a frequency $1/\tau$. The steady state solution of this equation is:

$$\overrightarrow{v_D} = \frac{e}{m}\frac{\tau}{1+(\omega\tau)^2}\left(\overrightarrow{E} + \omega\tau\overrightarrow{E} \times \overrightarrow{B} + (\omega\tau)^2\frac{(\overrightarrow{E} \bullet \overrightarrow{B})\overrightarrow{B}}{B^2}\right), \tag{1.17}$$

where $\omega{=}eB/m$ is the Larmor frequency. Three cases are of special interest:

- in the absence of magnetic field, Eq. (1.17) is reduced to:

  $$\overrightarrow{v_D} = \frac{e\tau}{m}E = \mu\overrightarrow{E}, \tag{1.18}$$

  where μ is the mobility. In the case of electrons, μ depends on E through τ as shown in Fig. 1.4, on the contrary to ions for which the mobility is roughly constant. The presence of the electric field may *a priori* modify the charge diffusion equation:

  $$-\frac{\partial}{\partial t}n + D_T\left(\frac{\partial^2}{\partial x^2}n + \frac{\partial^2}{\partial y^2}n\right) + D_L\frac{\partial^2}{\partial z^2}n = 0, \tag{1.19}$$

where z is the direction of the electric field and D_L, D_T are the longitudinal and transverse diffusion coefficients respectively. Though these coefficients are generally not very different, significant anisotropic diffusions have been observed for some gases (see *e.g* [19]). Such an anisotropy can be explained by an energy dependent collision rate of electrons [20, 21], generally leading to a velocity reduction of fast electrons and therefore to $D_L < D_T$.

- in the inclusion of a magnetic field parallel to E, the drift velocity and the longitudinal diffusion stay the same, but the transverse diffusion is reduced:

$$D_T(B) = \frac{D_T(0)}{1 + (\omega\tau)^2}, \tag{1.20}$$

a feature which is particularly important to reduce the spatial resolution of Time Projection Chambers, but which can also degrade it in a standard Micromegas by reducing the cluster size.

- finally, if the magnetic field is perpendicular to E, charges drift with an angle θ_L with respect to E:

$$\tan(\theta_L) = \omega\tau = \frac{v_D B}{E}, \tag{1.21}$$

which reduces the drift velocity in the E direction by a factor $1/1 + (\omega\tau)^2$.

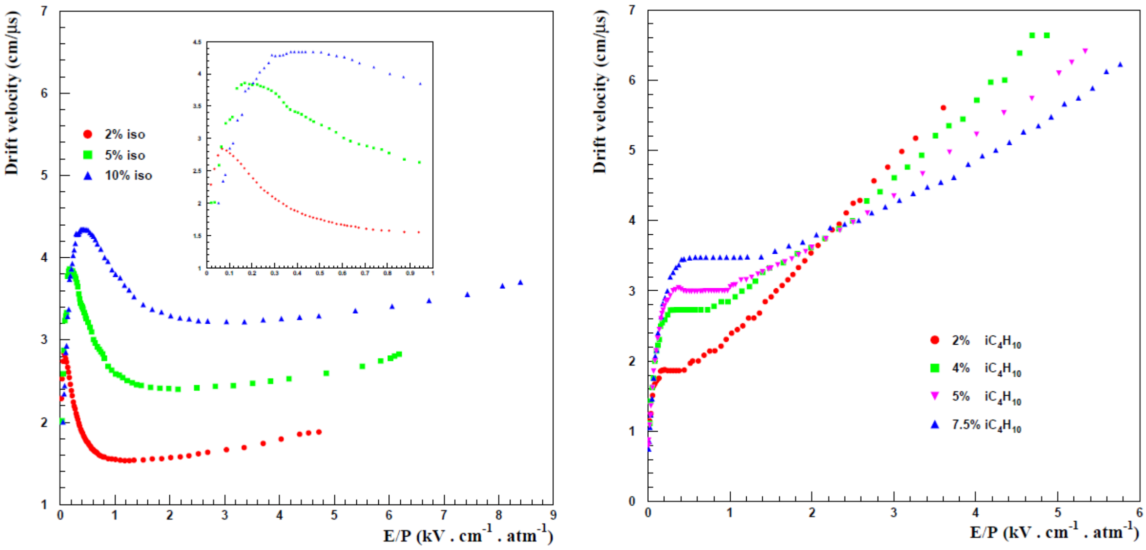

Figure 1.4: *Measured drift velocity of electrons in Argon (left) and Neon (right) - Isobutane mixture as the function of the reduced electric field E/P, illustrating that the electron mobility is not constant [22].*

Microscopic picture

The Langevin equation provides a good description of macroscopic variables, but hides all the microscopic mechanisms at work in the effective friction term, as well as differences of gas mixtures. At the microscopic level, electrons scatter isotropically on atoms or molecules. The electric field increases their energy in a time τ between two collisions, corresponding to an additional drift velocity given by:

$$\Delta v_D = \frac{eE}{m} \times \tau \tag{1.22}$$

This increase is compensated in average by the energy loss during collisions. By neglecting thermal energy one can easily derive the following expressions for the drift velocity and for the velocity v [3]:

$$v_D^2 = \frac{eE}{mN\sigma}\sqrt{\frac{\lambda}{2}} \qquad\qquad v^2 = \frac{eE}{mN\sigma}\sqrt{\frac{2}{\lambda}}, \tag{1.23}$$

where N is the atom density of the gas, σ the collision cross section and λ the mean relative energy loss for a single collision. The ratio of these quantities is simply $\lambda/2$ with typical values of λ rarely above 10^{-1}, which indicates that the drift kinetic energy contributes marginally to the total kinetic energy of electrons.

These expressions also emphasizes the importance of inelastic processes in the electron drift. In the (unrealistic) situation where only elastic collisions occur, $\lambda = 0$, and the drift velocity vanishes. In this case, electrons are constantly accelerated by the electric field without any energy loss, and the mean velocity becomes infinite. On the other hand, the maximum drift velocity would be obtained if electrons could lose all their energy during each collision! In practice the value of λ differs considerably for noble and polyatomic gases. In Argon for example, the first excitation level stands at 11.55 eV, which means that electrons have to acquire a lot of energy before being able to experience inelastic collisions. Their mean velocity is thus high, and the drift velocity stays small. This corresponds naturally to high values of transverse diffusion. Conversely, polyatomic gases like CF_4 or CO_2 have many excitation modes starting from 0.1 eV or less, maintaining electrons at low energy/speed and therefore high drift velocity. In this situation the transverse diffusion is reduced, as illustrated in Fig. 1.5.

This effect is strongly enhanced by the presence in Eq. (1.23) of the cross section σ. This cross section is shown for some noble gases in Fig. 1.6 (left) as a function of the electron energy. A well pronounced minimum is observed at energies between 0.1 and 1 eV, *i.e.* in the region of many polyatomic excitation modes. This minimum arises from quantum mechanics, and corresponds to a particular wavelength at which the atom becomes nearly transparent for the incoming electrons whose mean free path increases. The effect, called the **Ramsauer effect** [24] is particularly pronounced for noble gases like Argon or Xenon. Small additions of polyatomic elements in such gases therefore shift the electron energy close to the Ramsauer minimum, enhancing their drift velocity.

Though Fig. 1.6 (left) indicates that there is no Ramsauer effect in Neon, the cross section

---

[3] A full calculation brings extra factors of 0.855 and 0.854 respectively.

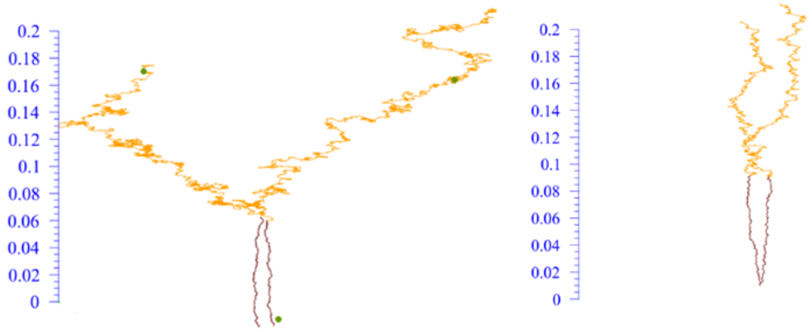

Figure 1.5: *Simulation of electron diffusion in Ar-*CO_2 *mixture, 95-5% (left) and 70-30% (right) [23]. The trajectories are zoomed in on the horizontal axis.*

is reduced at low energy. This particular shape, combined with the λ dependence, is used for example in the Compass experiment, where 10% of CF_4 is added to the Neon-Ethane mixture. The enhanced drift velocity directly affects the time resolution of the detector which goes from 15 to 9 ns.

We have only sketched here the main features of the electron drift in gases. A complete theory of charge transport is beyond the scope of this review, and can be found in [25]. The ion transport is of less importance in our case, but it is worth mentionning the recent work on the so-called *cluster ions* suggesting that ions form bigger aggregates during collisions whose sizes rapidly evolve in time [26].

Similarly to Heed for the ionization part, transport simulation tools are available to design and optimize the performance of gaseous detectors. The widely used **Magboltz** [27] program developed by S. Biagi can compute in particular many drift and diffusion parameters with good accuracy, as illustrated in Fig. 1.7 for the Lorentz angle. It contains the energy dependent cross sections of around 60 gases, with separate contributions from elastic, ionization and excitation modes. These cross sections are collected and made available through the open-access website **LXCat** [28], as examplified in Fig. 1.6 (right) for Argon.

1.3 Amplification and signal formation

As we have seen above, the number of charges created during the ionization of the gas by the incoming particle is usually small, of the order of 100 per cm for a MIP [4]. So far such a small number of charges cannot be identified in typical electronics noise, and gaseous detectors therefore feature an amplification stage to produce a detectable signal.

---

[4] This is in deep contrast with solid detectors like Silicon where the number of electron-ion pairs yields 100 per micron, *i.e.* 10^4 times higher

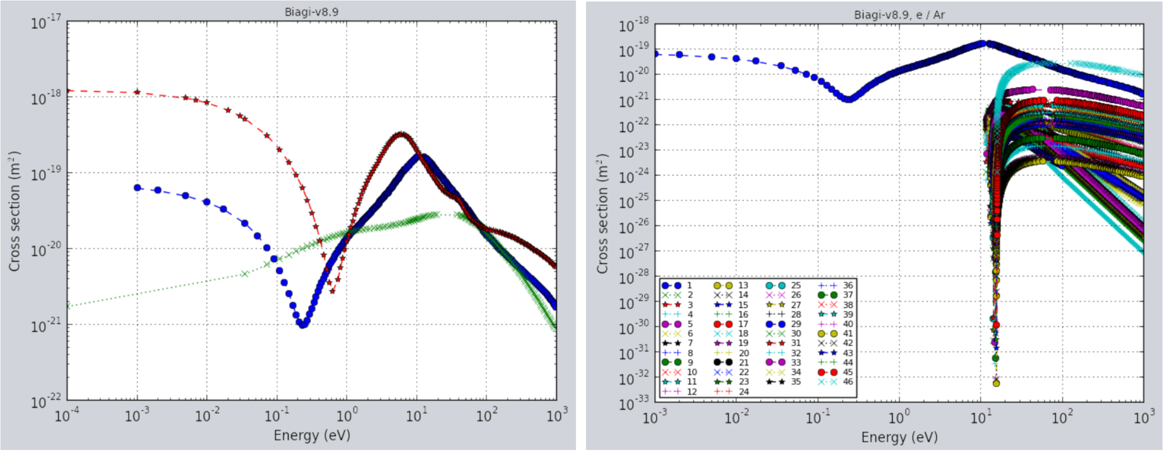

Figure 1.6: *(Left): elastic cross sections for Argon (blue), Neon (green) and Xenon (red) as a function of the electron energy. (Right): elastic (1), excitation (2-45) and ionization (46) cross sections for Argon. Both plots are extracted from [28].*

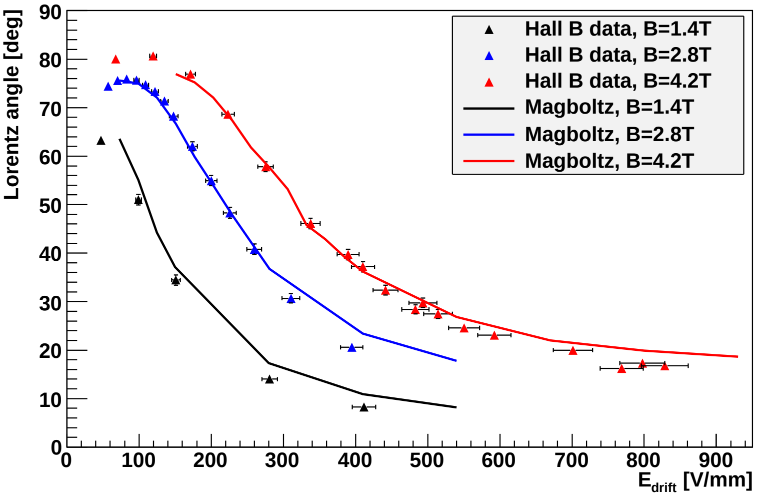

Figure 1.7: *Comparison of the measured Lorentz angle in a Micromegas for different magnetic fields with Magboltz [29]. Gas mixture is Argon-Isobutane (90-10%).*

1.3.1 Gain and first Townsend coefficient

The first physics elements of charge amplification by electric fields in gases were developed by Townsend [30], who introduced in particular the probability that an electron creates an additional electron per unit drift length, α, known as the **first Townsend coefficient**. If we consider $n(x)$ electrons travelling between x and $x + dx$ along the field direction, then the number of created electrons writes:

$$dn(x) = \alpha(x)n(x)dx, \tag{1.24}$$

with straightforward integration:

$$n(x) = n(0)e^{\int_0^x \alpha(y)\,\mathrm{d}y} \tag{1.25}$$

The mean ratio $< n(x)/n(0) >$ between the final and initial number of electrons is called the amplification factor, or the gain G. In the case where α is independent of the position, one gets the well known formula:

$$G = e^{\alpha x} \tag{1.26}$$

α naturally increases with E as electrons acquire more energy between collisions, and the following parametrization was empirically derived by Townsend [30]:

$$\frac{\alpha}{P} = Ae^{-\frac{BP}{E}}, \tag{1.27}$$

where P is the gas pressure, and A, B two gas dependent parameters. In the case of a Penning gas mixture the gain can be significantly increased by the extra-production of electron-ion pairs during the avalanche. In Argon-Isobutane, the most effective Penning transfer is obtained with roughly (95-5%) mixture, a value at which the highest gains are observed.

1.3.2 Gain fluctuations

Though the knowledge of the gain is of primary importance to estimate the performance of a detector, gain fluctuations are also crucial since the occurence of smaller avalanches may directly affect the overall detection efficiency. Similarly to the Bethe-Bloch equation for the energy loss, the first Townsend coefficient expressed as above does not give access to the gain distribution emerging from statistical fluctuations. However, $1/\alpha$ can also be interpreted as the mean free path of electrons between two ionizations. If we consider that the number of ionizations for a given length follows a Poisson distribution, then the electron free path distribution is exponential with a mean value of $1/\alpha$. We can thus derive the probability $p(n, x)$ to get exactly n electrons over a distance x from a single electron, corresponding to the **Furry distribution** [31, 32, 33]:

$$p(n, x) = \frac{1}{\bar{n}}\left(1 - \frac{1}{\bar{n}}\right)^{n-1} \approx \frac{e^{-n/\bar{n}}}{\bar{n}}, \tag{1.28}$$

with $\bar{n}$ defined as $n(x)$ in Eq. (1.25) with $n(0) = 1$. This distribution is in fair agreement at low gains, but its maximum stands at n=1 whatever $\bar{n}$, *i.e.* no ionization, which rapidly turned out to be in contradiction with measurements at higher gains [34].

A much better agreement can be obtained by taking into account the history of the ionizing electrons. One way consists in introducing a cut-off in the exponential distribution of the free path to take into account the minimum energy that an electron has to gain between two ionizations [35]. A n-dependence of α was also proposed, based on the argument that large avalanches contain in average electrons with smaller energies and thus smaller probabilities to ionize. Using a simple, first order formula for this dependence [36, 37], the total electron number in the avalanche is found to follow the well-known **Polya distribution**:

$$p(n,\theta) = \frac{1}{\bar{n}}\frac{(1+\theta)^{1+\theta}}{\Gamma(1+\theta)}\left(\frac{n-1}{\bar{n}}\right)^{\theta} e^{-\frac{n-1}{\bar{n}}(1+\theta)} \tag{1.29}$$

The Furry distribution corresponds to the case $\theta \to 0$, and the Poisson distribution to $\alpha_0 \to \infty$. On the contrary to Furry, the Polya law exhibits a maximum at [38]:

$$n_{max} = \bar{n}\frac{\theta}{1+\theta} \tag{1.30}$$

The Polya law turns out to reproduce the measurements quite well and is still widely used in the community of gaseous detectors. However, its simplistic hypothesis on the n-dependence of α has been discredited by several authors [39, 40], and the observed agreement should be considered as mainly accidental. As can be seen in Fig. 1.8, a full Magboltz simulation taking into account all microscopic processes described in the ionization section now reaches nearly perfect agreement with data.

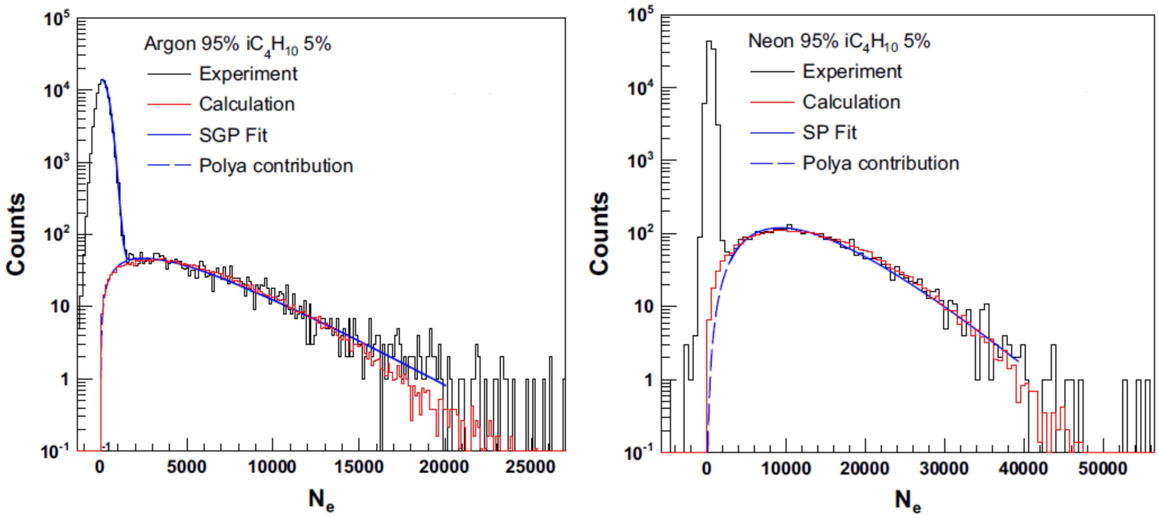

Figure 1.8: *Comparison in Argon (left) and Neon (right) mixture of the electron number distribution in single avalanches between measurements (black), Polya fit (blue) and Magboltz simulation (red) [41].*

1.3.3 Signal formation

As in other gaseous detectors, the current signal appearing on the readout anode of the Micromegas is *induced* by the *movement* of the charges in the amplification region, and not from their actual collection on the electrodes. The current $i_c(t)$ induced by a single charge q at $x(t)$ with a velocity $v(t)$ can indeed be expressed from the **Shockley-Ramo theorem** [42, 43], stating that:

$$i_c(t) = -q \times \overrightarrow{v}(t)\overrightarrow{E_w}(x(t)), \tag{1.31}$$

where the so-called weigthing field $\overrightarrow{E_w}(x(t))$ is the electric field that would exist at the position $x(t)$ of the charge, this charge being removed, with a unit potential on the considered electrode, all other electrodes being grounded.

Let's then consider the case of an electron-ion pair created in the amplification gap of a Micromegas, at a distance l of the readout plane built from a single readout element. The weighting field is constant and equal to $1/d$, d being the amplification gap. The current induced by these two charges then writes:

$$i_c(t) = e\left(-v_-\frac{1}{d}\right) - e\left(v_+\frac{1}{d}\right) = -\frac{e}{d}\left(v_- + v_+\right), \tag{1.32}$$

where v_- and v_+ are the electron and ion drift velocities. Both charges induce a negative current, but the electron contribution is much higher because of its large velocity. The total charge induced on the anode corresponds to the integral of this current during the travelling time of both charges:

$$Q_c = -\frac{e}{d}\left(v_-t + v_+t\right) = -\frac{e}{d}(l + (d-l)) = -e \tag{1.33}$$

It means that the charge induced by a electron-ion pair effectively corresponds to the collected charge on the anode, wherever this pair is produced. However, the relative contribution of the pair depends strongly on l. Because of the avalanche structure, the vast majority of the charges are created very close to the anode plane of the Micromegas. Therefore $l \ll d - l$, and the collected charge on the strips mainly originate from the ion movement, typically 80 to 90%. The induced current for a given geometry can be computed with the well-known **Garfield** package developed by R. Veenhof [44], which integrates the Heed and Magboltz programs mentioned above to form a complete and powerful simulation tool for gaseous detectors in general. As an illustration, Fig. 1.9 shows the computed induced current from an avalanche in a Micromegas, where the electrons and ions contributions appear clearly.

1.4 Choice of the gas mixture

We finish this chapter by a rapid discussion on the choice of the gas mixture, which is often a delicate topic. The final choice is usually a compromise between different criteria — resolutions, efficiency, cost — and strongly depends on the experimental setup.

Most of the gas mixtures are based on noble gases whose full electronic shells give them interesting properties. They have in particular null attachment coefficients, and do not undergo chemical reactions with the detectors components that could lead to long term

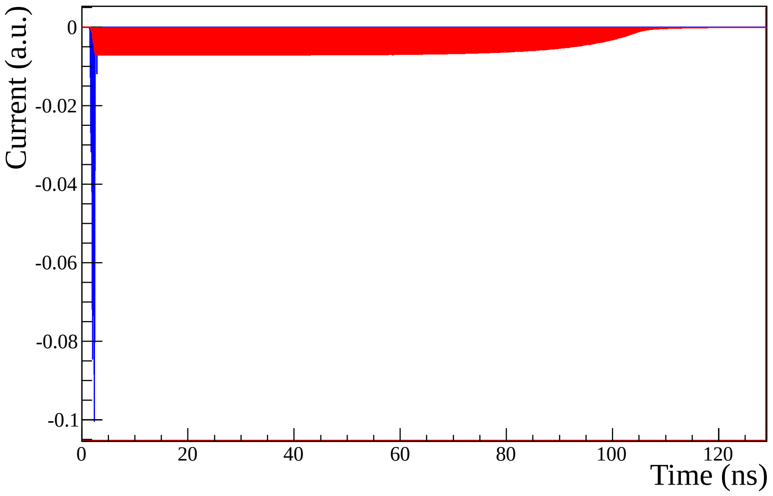

Figure 1.9: *Garfield simulation showing the time evolution of a typical signal on the readout strips, with the electron (blue) and ion (red) contributions [45].*

ageing. Besides, they provide relatively high gains at low electric fields. However, the amplification in pure noble gases is relatively unstable and initiates many secondary avalanches through the copious emission of UV photons (see Chapter 4). These secondary avalanches eventually lead to discharges and significantly deteriorate the energy and spatial resolutions. Furthermore, the absence of inelastic processes at low electron energy increases the transverse diffusion to unreasonable values and diminishes the net drift velocity, as was discussed in Section 1.2.1.

For these reasons, polyatomic gases are frequently combined with noble gas. Their first role is to absorb the UV photons produced during the avalanche, thanks to their numerous rotation and vibration excitation modes [5]. Their high inelastic cross sections are also beneficial to reduce the transverse diffusion and enhance the drift velocity, a process emphasized by the Ramsauer effect. Last but not least, they enhance the ionization yield, directly and indirectly through the Penning effect. On the other hand, their large atomic mass is accompanied by a higher discharge probability in hadron beams (see Chapter 4). In practice these gases are also available with lower levels of purities, which can rise issues on unwanted pollutants [6]. Finally, and depending on the nature of the gas, ageing can also develop with time, by the intrinsic reactivity of the components (DME) or by polymer accumulation (hydrocarbons). Though the fine tuning of a gas mixture usually follows from detailed simulation, we indicate below the main characteristics of the most common gas elements for the Micromegas detector:

---

[5] By doing so they contain the development of discharges, and are often named **quenchers**.

[6] As an illustration, Argon bottles are typically available with a 99.9990% purity level (named as 5.0), when Isobutane only has 3.5.

Noble gases

- Neon: modest ionization yield requiring larger drift gaps; high drift velocity in mixtures; low discharge probability in hadron beams; relatively expensive
- Argon: good ionization yield; low drift velocity, suitable to decrease the Lorentz angle in perpendicular magnetic fields; higher discharge probabilities in hadron beams; very cheap
- Xenon: excellent ionization yield; high discharge probabilities; very expensive, requires a gas recycling system

Helium is in practice rarely used because of its limited ionization yield.

Polyatomic gases

- CO_2: large drift velocity; non flamable; relatively inert; cheap; low achievable gains, making it more suitable for GEM than for Micromegas
- hydrocarbons (CH_4, C_2H_6, iC_4H_{10}): high achievable gains; very good energy resolutions; highly flamable
- CF_4: large drift velocity and reduced transverse diffusion; persistant greenhouse gas (greenhouse warming potential of 6500)
- SF_6: excellent dielectric rigidity; strongest greenhouse gas (greenhouse warming potential of 22800)
- DME (Dimethyl ether): high ionization yield; small Lorentz angle; good quenching properties; highly flamable

Chapter 2

Characterization and performance of Micromegas

Having introduced in the previous chapter the general principles of the Micromegas detector, we will now focus on its practical use and performance. After a short description of the manufacturing process, we will explain the different steps and elements needed to operate it, including the readout electronics. We will then detail its main features and performance, with a special treatment of resistive detectors.

2.1 Manufacturing

2.1.1 The Printed Circuit Board

The first element of the detector is the Printed Circuit Board (PCB) built from an insulated substrate on which strips are etched from laminated Copper sheets. Typical strip thicknesses vary from 9 to 15 microns and can be lowered down to 5 microns if the radiation length is an important issue, see Table 2.1. Depending on the complexity of the layout, the PCB may be single sided (one Copper layer) or multi-layer. In the latter case, the different layers are connected through vias, *i.e.* holes filled with Copper by electroplating. Vias are used in particular in 2D layouts, or with return strips or double sided/multiplexed detectors. Commonly used substrates include epoxy resins, sometimes reinforced with woven fiberglass, or polyimide films like Kapton® foils. To ensure a good rigidity and flatness with a low material budget, the PCB is usually glued on a layer of honeycomb or on a Rohacell foam plate. In the case of cylindrical detectors, the flexibility requires a maximum PCB thickness of about 300 microns.

2.1.2 The bulk technology and the micro-mesh

The most sensitive part of the detector manufacturing is the integration of the micro-mesh on the PCB. Indeed, these two elements define the size of the amplification gap, and largely determine the maximum achievable gain, both the energy and the spatial resolutions, as well as the overall uniformity of the detector. The early Micromegas prototypes were using stretched micro-meshes deposited on fishing lines to define precisely the amplification gap. These lines were rapidly replaced by pillars built from photoimageable films, as in the first Micromegas of Compass [46]. The dead zone resulting from these pillars was found to be negligible, of the order of 1% [47]. However, the micro-mesh stretching was not necessarily optimal, and defects were observed, as illustrated in Fig. 2.1. In addition, the micro-meshes were not amagnetic, and those from the closest detectors to the solenoid were attracted, with the consequence of a gain loss due to a larger gap.

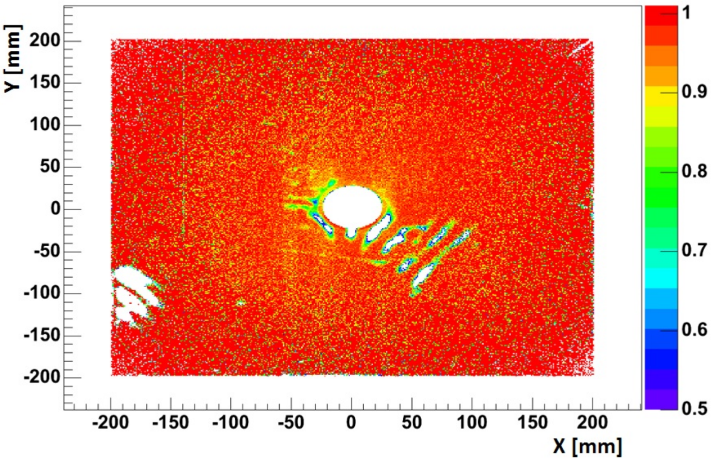

Figure 2.1: *High resolution 2D efficiency plot of a Compass Micromegas. Several zones of unefficiencies are visible, corresponding to regions where the micro-mesh is not properly stretched over the pillars.*

A significant improvement in the manufacturing process was introduced in 2006 with the embeddement of the micro-mesh in the pillars themselves. In this technique a sandwich, or **bulk**, is built from a succession of operations [48]:

- one or several layers of uniform, photo-sensitive films [1] are first laminated on the PCB, as shown on Fig. 2.2 (left). These films have a precise thickness which ensure a good uniformity of the amplification gap. They also determine the size of the gap, *e.g.* 128 microns with two 64 micron layers
- the micro-mesh is stretched and glued on a frame, and laminated between the PCB and an additional layer of photo-sensitive film
- this sandwich is then exposed to UV light for polymerization of the films through a mask which will define the positions of the pillars and the edge walls

---

[1] like Vacrel® or Pyralux®

- the non polymerized part is entirely dissolved in a sodium carbonate bath, with careful rinsing between the different passes
- the detector is finally cooked thermally to harden and dry the polymerized material

All the parameters appearing in the different steps — micro-mesh stretching, lamination temperature and pressure, power and time of UV exposure, concentration and number of passes in the sodium carbonate bath, oven temperature — should be carefully adjusted to the detector configuration and to the machines involved. Fig. 2.2 (right) shows the final pillar embedding the micro-mesh.

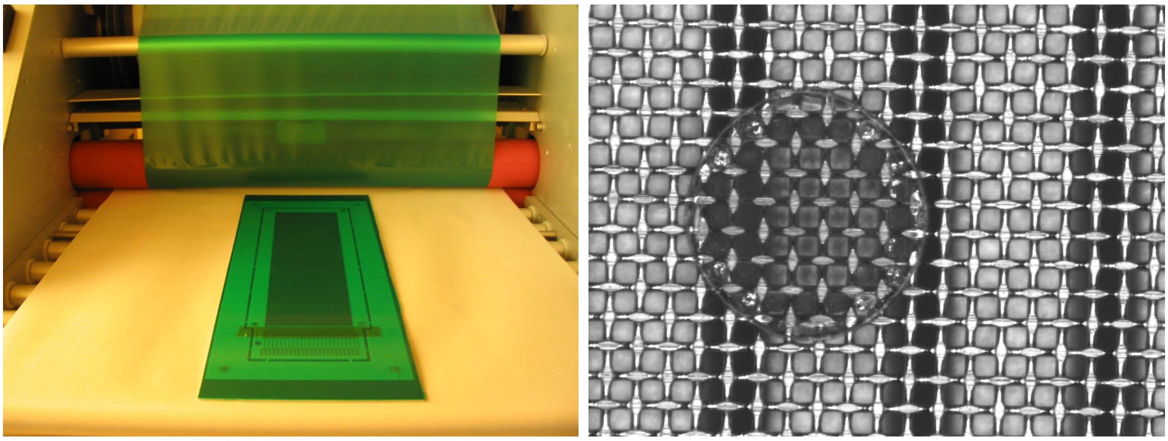

Figure 2.2: *(Left): lamination process, with the photo-sensitive film in green. (Right): picture of a final bulk showing a pillar embedding the micro-mesh. The structure of the woven micro-mesh as well as the underneath strips are also visible.*

This technique considerably improves the robustness of the detector, and ensures a uniform amplification gap, avoiding structures like in Fig. 2.1. Another important advantage is to integrate many processes routinely used in micro-electronics companies. This has opened the way to an industrialization of these detectors, with potentially huge production capabilities. A know-how transfer has in particular been initiated in 2010 with the Elvia group which produced several detectors for Compass. Massive production allows for large scale applications, like the 1200 m^2 of the future Atlas New Small Wheel, or for potential use of Micromegas in the field of muon tomography (see Chapter 5).

On the other hand, the lamination process is practically incompatible with thin, electroformed micro-meshes. Instead, thicker, stainless steel woven meshes were introduced. Though cheaper, these meshes now amount for roughly 1/3 of the total material budget as shown in Table 2.1. In spite of prior lamination, the woven structure also degrades the energy resolution of the detector (roughly 20-25% FWHM at 6 keV). Another manufacturing technique, called the micro-bulk [49], was later implemented for applications in which this resolution is an important parameter. Micro-bulks are still strongly limited in size, but reaches energy resolutions around 10-15% FWHM at 6 keV.

The last step of the detector's manufacturing is the integration of the drift electrode which is attached on a frame glued or screwed on the PCB, this frame defining the drift gap.

In the special case of a TPC, the frame is replaced by a specially designed field cage to maintain a uniform drift field on the edges of the detector.

2.1.3 The resistive film

In the case of resistive Micromegas, a resistive layer is added on the bare PCB [50, 51]. The first detectors were prepared with a resistive ink spread on the PCB, and manually polished to achieve the final desired resistivity. Though this lengthy method was successfully used both at Cern and in industry (Elvia), it was soon replaced by a serigraphic process in which the resistive ink is applied on a Kapton foil through a stencil. This process has the advantages to be more reproducible, with larger production capabilities and to be independent on the bulk manufacturing. The Kapton foil is indeed prepared separately, and pressed on the PCB prior to the first lamination. Serigraphy also allows for a wide variety of patterns, as illustrated in Fig. 2.3, and in particular for the implantation of *ladders*. These ladders are introduced to lower the resistivity, make it more uniform over the active area and to ensure an electric connection even in the case of cut resistive strips. For high rate applications, these ladders also permit a faster evacuation of the charges from the hottest regions. However, we will see in Section 2.5 that these ladders can also spread a leakage current in the presence of dust.

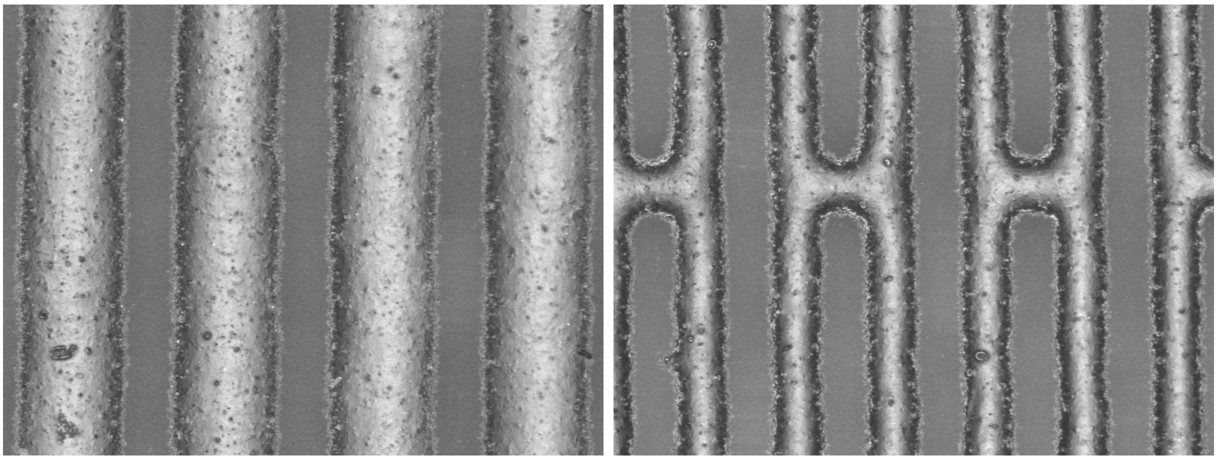

Figure 2.3: *Pictures of resistive strips obtained by serigraphy, without (left) and with (right) connection ladders.*

2.1.4 Material budget

As other gaseous detectors, Micromegas has a relatively low material budget which makes it particularly interesting at medium and low energies. The multiple scattering indeed deteriorates the performance of a tracker and its contribution may ruin the intrinsic spatial resolution of detectors as we will see in Chapter 3. Table 2.1 details the material budget of a typical Micromegas detector in terms of radiation length, and shows the contribution of the different elements. For comparison, the first Compass Micromegas yielded $0.40\%X_0$ [2], three GEM foils alone represent already $0.22\%X_0$, and a 300 micron Silicon $0.32\%X_0$.

element	material	X_0 (cm)	thickness (cm)	opacity	budget (X_0)
PCB	epoxy	32.5	0.010	1	$3.1e^{-4}$
resistive film	glue	35.5	0.003	1	$8.5e^{-5}$
resistive film	Kapton	28.6	0.005	1	$1.7e^{-4}$
resistive film	Carbon strips	~19.3	0.003	0.73	$\sim 1.1e^{-4}$
strip	Copper	1.44	0.0009	0.73	$4.6e^{-4}$
pillars	Pyralux	~30	0.0128	0.008	$\sim 3.4e^{-6}$
micro-mesh	stainless steel	1.76	0.003	0.56	$9.5e^{-4}$
gas	Argon	10971	0.3	1	$2.7e^{-5}$
drift electrode	Copper	1.44	0.0005	1	$3.5e^{-4}$
drift electrode	Kapton	28.6	0.015	1	$5.2e^{-4}$
Total					$\sim 2.98e^{-3}$

Table 2.1: *Contributions to the material budget of a typical Micromegas, in this case a tile from the Clas12 Barrel Vertex Tracker.*

2.2 Integration

2.2.1 High voltage and cooking

Negative high voltages are applied on the micro-mesh and the drift electrode to create the appropriate electric fields. RC components are inserted to filter the high frequency noise of the environment, see Fig. 2.4 [47]. These filters also play an important role in the case of discharges, as we will see in Chapter 4. The nominal current circulating in the micro-mesh ranges from sub nA to a few μA values at high particle rate, and special power supplies are used with precise monitoring. Values larger than a few nA are also routinely observed during the first polarization of the detector. Humidity in the vicinity of the pillars, incomplete polymerization and micro-dust can indeed create a remnant conductivity with the strip plane. This conductivity requires an initial *cooking* of the detector, during which the current can fluctuate significantly, as illustrated in Fig. 2.5 (left).

Resistive strip detectors offer an additional degree of freedom in the polarization scheme, namely to apply a positive high voltage on the resistive strips and ground the micro-mesh. Though this requires the use of power supplies with both polarities, this option allows to ignore possible faulty connections between the micro-mesh and a grounded component of the detector, *e.g.* the frame. Such faulty connection may arise near the micro-mesh cut if a wire is partly detached, as seen in Fig. 2.5 (right).

---

[2] excluding the Copper Kapton used for shielding

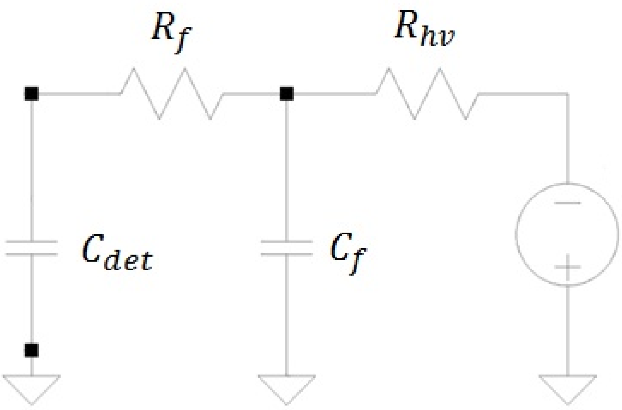

Figure 2.4: *Scheme of the high voltage filter used for the electrode polarization. The same filter is used on resistive strips in the case of reverse polarization. Typical values are* R_{hv} *~ 1-10* $M\Omega$*,* R_f *~ 1* $k\Omega$*, and* C_f *~ 10-100* nF*.*

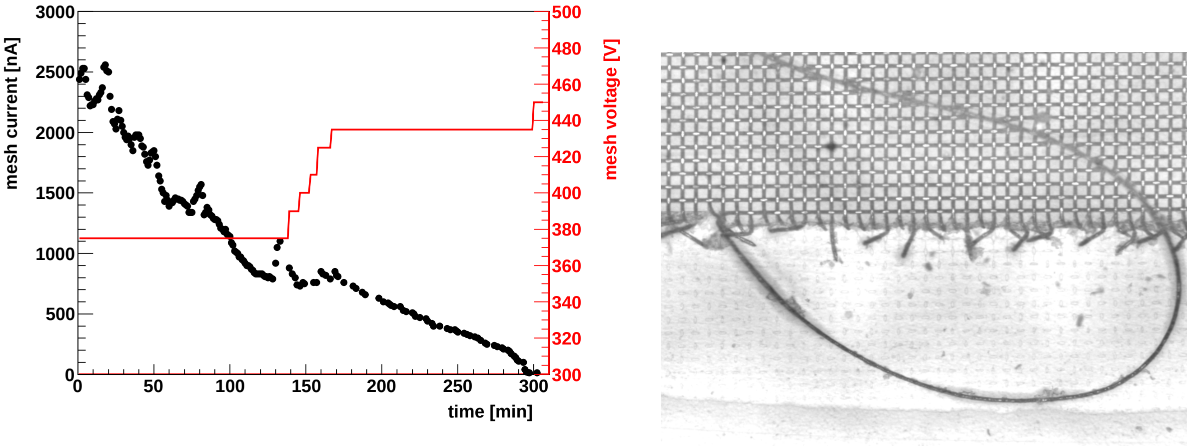

Figure 2.5: *(Left): time evolution of the micro-mesh current on a Micromegas during its initial cooking. Random variations are observed probably due to the burning of dust, with a general, slow current decrease up to usual nA values. (Right): example of a detached wire after the micro-mesh cut.*

2.2.2 Gas circulation

The gas is provided either with pre-mixed bottles or with a gas mixer equiped with flowmeters. The latter, being cheaper on the long term and allowing for concentration studies, usually delivers the gas in normal liters (ln) and the final mixture may then differ from the pre-mixed. Depending on the configuration, the time to fully *flush* a detector roughly corresponds from 3 to 10 renewals of its volume, as shown in Fig. 2.6. Without a gas recycling system or special R&D on the materials, a minimal flow should be maintained to avoid performance degradations due to outgassing components of the detector. Special care should also be taken on the gas pipes from the bottles to the detector in order to avoid dust or polluants. Gas filters can be used, and were found to indeed increase the stability of detectors operation at long term. Bubblers are frequently installed downstream the detectors as a simple way to detect leaks in the gas system. In the case of thin detectors, upstream safety bubblers are also integrated to avoid damaging overpressures.

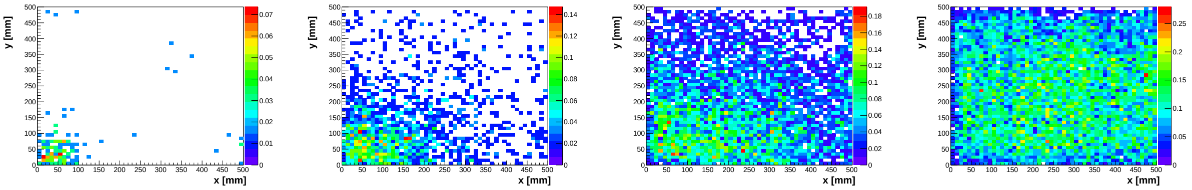

Figure 2.6: *Evolution of the gas circulation in a detector through the measurement of the cosmic flux (per cm^2 and minute) after 1, 3, 5 and 9 volume flushes. The gas enters with a flux of 5 L/h on the bottom left part of the detector whose active volume is 2.5 L. The flux drop on the edges is an artefact of the apparatus.*

2.3 Readout electronics

2.3.1 General principles

The signal induced on the anode elements is readout by a dedicated electronics performing a series of operations until data are sent and recorded on a disk for offline analysis. Though there is a large variety of electronics implementation in practice, modern architectures are frequently divided in two parts to optimize the performance and the cost (see for example [52]. The Front-End (FE) part goes from the integration to the bufferization of the analog signal, followed by a digitization and a potential compression of the selected data. These data are sent to the Back-End (BE) electronics ensuring the data concentration as well as the interface with the DAQ and the trigger system. In this section we will focus on the FE and its various elements as it is designed in close connection with the detectors and determines their overall level of performance through the optimization of the S/N ratio.

The first element of the FE is the protection circuit to protect the electronics against the discharges. If the total charge collected from a MIP approximately yields 10-100 fC, a discharge can release hundreds of nC, *i.e.* at least a million times more. The anode elements are therefore individually decoupled from the ground via a capacitance C_{AC} which limits the current in the case of a discharge. Stress tests with several millions of discharges proved that in this case no damage occurs. This protection circuit can be removed with resistive detectors for which the amplitude of the discharge is considerably smaller and harmless.

The signal is then amplified and integrated by a Charge Sensitive Amplifier (CSA) through a feedback capacitance. The total transfer function is given by:

$$T_F = T_{FCSA} \times \frac{C_{AC}}{C_{AC} + C_{det} + C_{cab}}, \tag{2.1}$$

where C_{det} (resp. C_{cab}) is the detector (resp. cable) capacitance. The second term comes from the charge division of the circuit, while the first term is the transfer function of the CSA only:

$$T_{FCSA} = K \frac{1}{1 + \frac{C_{det}+C_{cab}}{A_0 C_f (1+\frac{C_{det}+C_{cab}}{C_{AC}})}}, \tag{2.2}$$

with A_0 its open loop gain. These formulas show that the input (detector and cable) capacitance modifies the transfer function in the charge division and in the CSA itself. In particular, large capacitances require to increase the coupling C_{AC} and to optimize the CSA to enhance the value of A_0. The effect of the input capacitance is shown in Fig. 2.7 on S and N/S: the latter in particular is found to depend almost linearly with the cable capacitance for a given detector.

The CSA is followed by a filtering stage whose role is to integrate and shape the primary signal resulting from the sum of single avalanche signals shown in Fig. 1.9. The integration window and the length of the output signal are determined by the *peaking time* t_p of the filter. In most cases, the choice of the peaking time results from a compromise between contradictory criteria:

- a large value is favored to fully integrate the ion tails as well as other avalanches originating from different primary electrons. A too small value indeed results in a ballistic deficit reducing the S/N ratio and degrading both the efficiency and the spatial resolution
- a longer integration also reduces the noise by averaging it. At first order, the noise amplitude goes with $1/\sqrt{t_p}$ for reasonably small t_p [53].
- on the other hand, a rapid integration improves the time resolution
- last but not least, a small peaking time shortens the signal and thus limits the pile-up at high flux

Typical values of t_p range from 100 to 200 ns, corresponding to the minimal integration time without ballistic deficit. The overall effect of t_p on S and N/S ratio is illustrated in Fig. 2.7. The signal amplitude is reduced at 100 ns because of the ballistic deficit, but similar at 200 and 400 ns. However 400 ns is more favourable for the S/N ratio because of the further noise reduction.

The next step consists in storing the filtered signal until a potential trigger signal arrives. Due to electronics and detectors response times, a certain delay is indeed necessary to form the trigger [3] and propagate it. During this delay, called the trigger latency, all the signals should be memorized for possible further readout. Modern FE chips use arrays of capacitors (or SCA for Switched Capacitors Arrays) acting as circular buffers in which the filtered signals are sampled in cells, as illustrating in Fig. 2.8 (left). When the trigger signal is issued, the cells of interest are readout, multiplexed and sent to external ADCs for

---

[3] either from these detectors or from a combination in more complex experiments

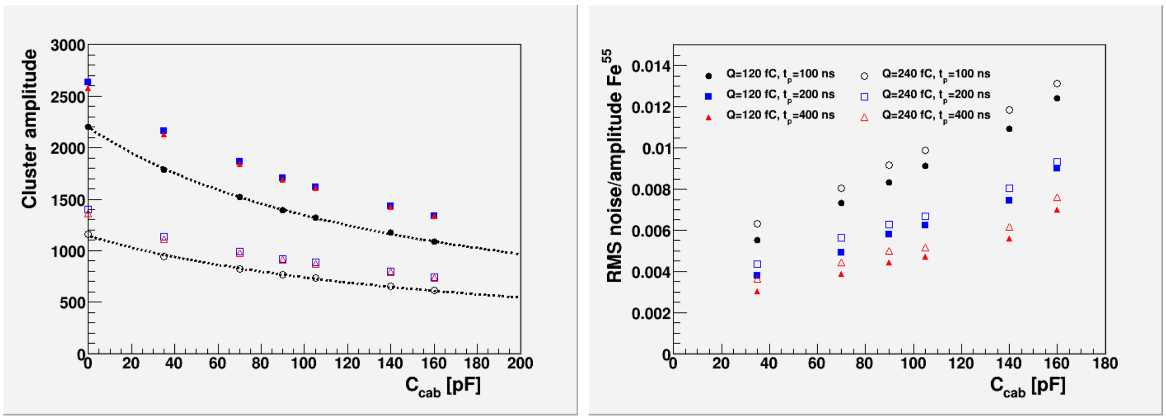

Figure 2.7: *S (left) and N/S ratio (right) measured on Micromegas strips with a* Fe^{55} *source, as a function of the cable capacitance, for different preamplifications and peaking times* t_p *(T2K/After electronics).*

digitization. Depending on the electronics, this readout is accompanied by a pause in the sampling process, or simply by a freeze of selected cells. The number of cells of the circular buffer is primarily determined by the trigger latency L_T, and should always be larger than $L_T \times F_s$, where F_s is the sampling frequency. As can be seen in Fig. 2.8 (right), the SCA occupies a large fraction of the whole chip.

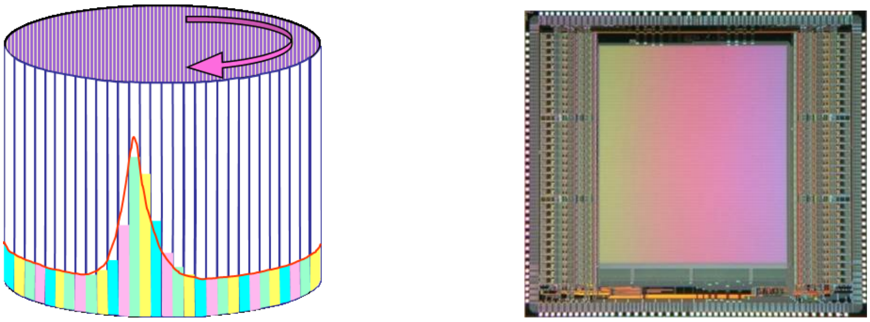

Figure 2.8: *(Left): illustration of the principle of a circular buffer which samples and stores the filtered signal [54]. (Right): picture of the AGET chip and its SCA (inner square) [55].*

Additional signal treatment may be performed by the FE part, for example with an FPGA, to further reduce the amount of data to be transferred to the BE. This can be done by applying a zero suppress procedure as follows:

- first, the pedestal value from each channel is subtracted to the signal. To achieve this, pedestals are calculated on separate data (pedestal run) and stored in the memory of the FPGA.
- Then the coherent noise is calculated for a group of channel and subtracted. This coherent noise originates from the electronics or from the micro-mesh, and can be enhanced for large area detectors and by grounding defects. On the contrary to

pedestals, it has to be evaluated directly on the data of interest, being event and sample dependent. In order to avoid bias from real, large signal, the coherent noise for a given sample is computed from the median values of the group.

- In the last step, only samples above a certain threshold are kept and transmitted. The threshold is defined as a programmable factor of the noise for the considered channel, where the noise is evaluated on a separate run after the coherent mode subtraction.

The pedestal and coherent noise subtraction is illustrated in Fig. 2.9. In this case the subtraction was performed offline to see the effect on the data.

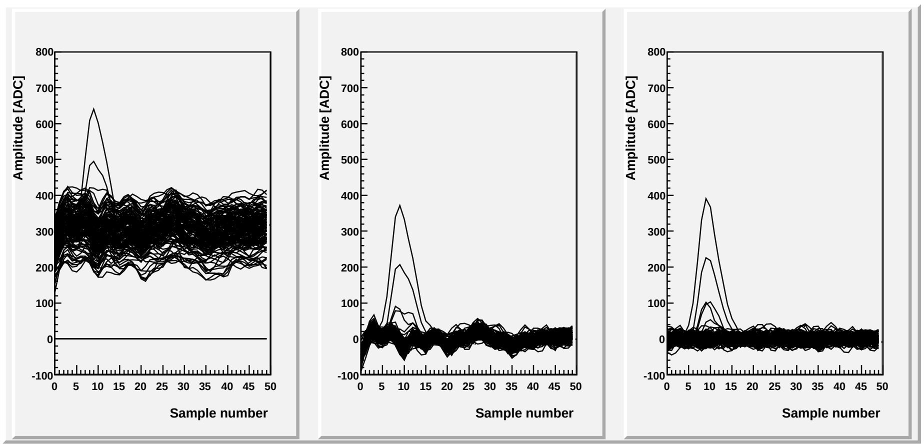

Figure 2.9: *Data from 64 strips of a Micromegas detector readout with the T2K/After electronics, as a function of the sample number. (Left): raw data; (middle): data after pedestal subtraction; (right): data after pedestal and coherent noise subtractions.*

2.3.2 Electronics for large capacitance: the Clas12/Dream readout system

We describe in this Section one of the most recent Micromegas readout systems, developed for the Clas12 Vertex Tracker (MVT). Its design has been driven by typical though challenging criterias of modern physics experiments: large area detectors, high flux of particles, high trigger rate, operation in a fringe magnetic field, high radiation level. The system is based on the dedicated Dream [4] asic [56] which benefitted from earlier developments of the After (T2K) and Aget chips.
A specific feature of the MVT is an unusually large input capacitance coming both from the detectors themselves (typically 70 to 100 pF) and from the electronic cables (75 to 110 pF). None of the available chips, including the APV, were designed for such high values, and early investigations revealed that the noise level would be prohibitive without significant

---

[4] Deadtimeless REadout Asic for Micromegas

modifications of existing electronics.
The block diagram of the Dream Asic is represented in Fig. 2.10, and the main characteristics are summarized in Table 2.2. In addition to an adapted CSA, a new SCA management was introduced to allow for simultaneous writing and reading. The external trigger indeed freezes a programmable number of cells and the sampling operation continues with the remaining ones. Once the frozen cells have been readout, they reintegrate the circular buffer. The 16 μs trigger latency requirement of Clas12 and the 20.8 MHz sampling frequency imposes a 512-cell deep buffer. The chip also contains a discriminator which compares the filtered signal with a programmable threshold set by a 7-bit DAC. This function, though not a requirement for Clas12, permits self-triggering operation and is exploited for muon tomography applications.

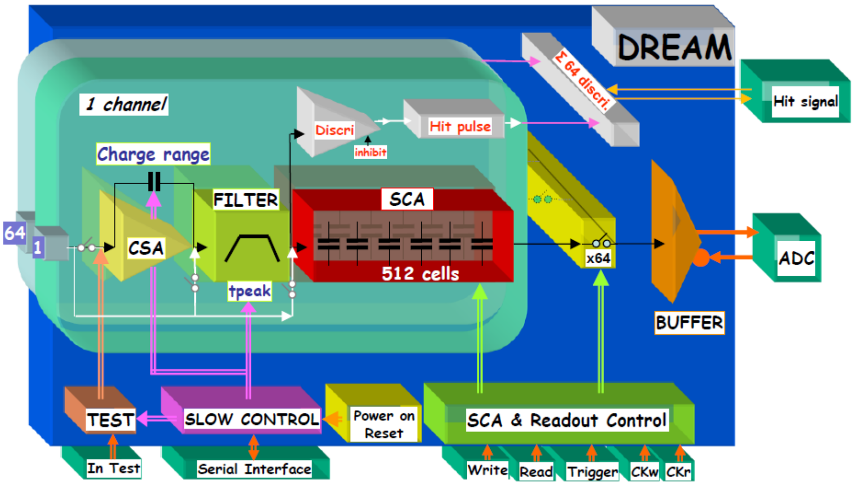

Figure 2.10: *Block diagram of the Dream Asic with the main analog elements described in the previous section, as well as the discriminator for the auto-trigger mode [57].*

The Front-End Unit (FEU) includes 8 Asics with their optional protection circuits for a total of 512 channels, an 8-channel flash ADC, and a FPGA system for the zero suppress mode. It also comprises a 2.5 Gbit/s optical link transceiver establishing a synchronous communication with the Back End Unit (BEU). The FEU receives the system clock as well as the trigger signals from the BEU, and returns event fragments built by the FPGA.
Detailed studies have been performed to quantify the gain of the Dream Asic, in particular with respect to After. In terms of S/N, an improvement of 13% has been observed in different configurations corresponding to 120-140 pF input capacitances. This improvement reaches 23% in the region of interest for Clas12 (roughly 200 pF), equivalent to 5 V difference on the high voltage.

polarity of input signal	positive or negative
channel number	64
input dynamic range (gain)	50, 100, 200, 600 fC (selectable per channel)
peaking time	50 to 900 ns (16 values)
SCA cell number	512
readout frequency	up to 20 MHz
sampling frequency	1 to 50 MHz
threshold range for triggering	5 or 17.5% of the input dynamic range
threshold value for triggering	7-bit DAC common to all channels
power consumption	<10 mW/channel

Table 2.2: *Characteristics of the Dream Asic.*

2.4 Characterization and performance of standard detectors

We have seen in the previous sections how to prepare and operate a Micromegas from its manufacturing to the readout electronics. We will focus here on the characterization of its performance which is usually accessed through different radiations and setups. The specific case of the resistive detectors will be studied in the next section.

2.4.1 Gain measurement

The detection capability primarily depends on the S/N ratio of the setup. In the signal part, the gain of the detector naturally plays a central role, and its value is therefore of utmost importance. As defined in Chapter 1, the intrinsic gain G is the mean number of electron-ion pairs created from a single primary electron. Its precise measurement for a given detector, though essential, is not an easy task because of various complications:

- the total charge recorded *in fine* on the electronics is reduced by different factors, *e.g.* the signal loss by capacitance effect or the micro-mesh transparency. The former can be overcome by reading the signal directly on the micro-mesh, and the latter can be practically neglected with an appropriate ratio of electric fields in the amplification and in the conversion gaps.
- The transfer function of the gain measurement chain is non trivial and should be measured separately (calibration).
- The gain usually depends on the position within the detector (inhomogenities).
- It also varies with the pressure, as explicited in Eq. (1.27).
- Last but not least it requires a precise knowledge on the mean number of primary electrons.

All in all, the precision of the gain estimate rarely goes below 20%.
In order to have a well controlled number of primary electrons, monochromatic sources like lasers or low energy radioactive elements are prefered. Among the latter, the 5.9 keV X-ray of the Fe^{55} is often chosen for simplicity. The incoming photon initiates a photo-electric effect releasing an electron from the K-shell [5]. For Argon, the binding energy of the K-shell is 3.2 keV, and the released electron carries the remaining 2.7 keV. De-excitation of the atom proceeds either by fluorescence, with the emission of a photon which escapes the detector, or by Auger effect [11], emitting an additional 3.2 keV electron. The electrons rapidly release their energy by ionization, leaving a spectrum composed of a 5.9 keV peak (2 electron case) and a so-called escape peak at 2.7 keV (1 electron and 1 lost photon), as shown in Fig. 2.11. To avoid any confusion, it should be kept in mind that the shape of this double spectrum depends on the atomic weight of the noble gas. The escape peak (fluorescence) indeed amounts for 15% in Argon, while it is negligible in Neon and reaches practically 90% in Xenon [58]. In a standard Argon-Isobutane (95-5%) mixture, 5.9 keV corresponds roughly to 230 primary electrons. With a laser, a proper attenuation stage allows for single electron emission [59, 60].

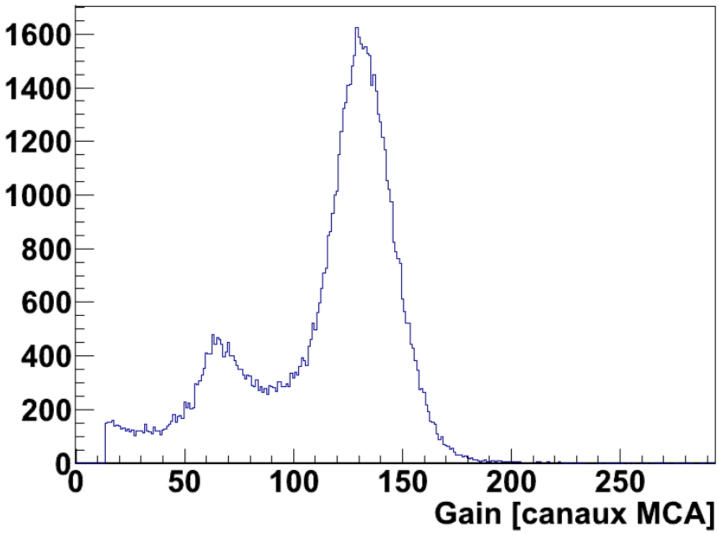

Figure 2.11: *Typical* Fe^{55} *spectrum obtained with a Micromegas readout by a MCA in a Argon-Isobutane (95-5%) mixture, featuring the escape peak at roughly half amplitude.*

The gain measurement is performed by reading the micro-mesh signal through a chain consisting of a pre-amplifier, an amplifier and a Multi-Channel Analyzer (MCA). Though their intrinsic response functions are available, a separate calibration of the chain provides much more precise measurements. The calibration is performed by replacing the detector by a capacitance C, and the physics signal by a pulser of amplitude V [6]. The output signal of the MCA is then expressed by:

$$S_{MCA} = K \times Q = K \times C \times V, \tag{2.3}$$

---

[5] The cross section is indeed favored by several orders of magnitude compared to more outer shells.

[6] The practical difficulty to know precisely C and V which are both small should not be underestimated.

from which the calibration constant K is extracted. Measurements then provide Q from which the gain is obtained knowing the number of primary N_p: $Q = G \times N_p$.
Measured gains of a Micromegas are shown for different gases in Fig. 2.12. An exponential dependence with the micro-mesh high voltage is observed, the slope depending on the gas mixture. For Argon-Isobutane (95-5%), the gain essentially doubles every 20 V. At low concentrations of Isobutane, an overexponential trend develops because of secondary avalanches due to UV photons. The maximal gain usually lies from 1 to 5×10^4 in Argon and can reach 10^5 in Neon, which compensates for the 10^4 higher ionization yield of Silicon detectors. Because of the varying Penning effect strength, maximal gains are obtained with specific mixtures in each noble gas, *e.g.* around 5% of Isobutane with Argon.

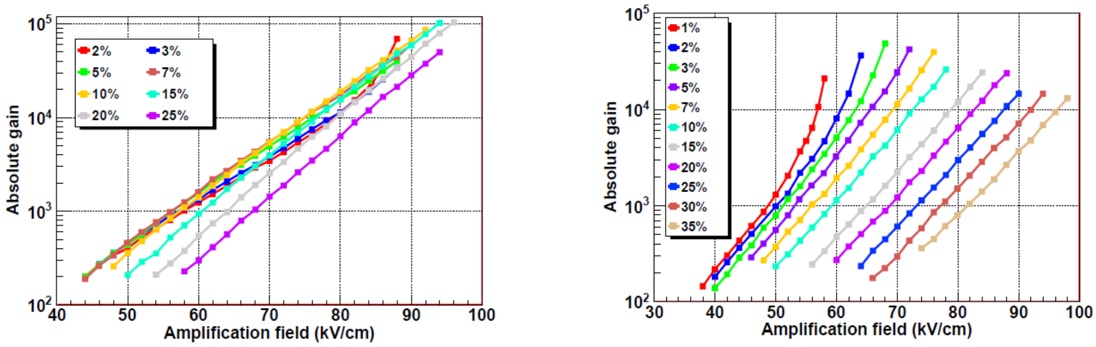

Figure 2.12: *Measured gains in a Micromegas detector with Neon (left) and Argon (right) Isobutane mixtures [61].*

The effect of the pressure on the gain has been extensively studied (see for example recent measurements from [62] with Micromegas) and is illustrated in Fig. 2.13. At a given field, a lower pressure increases the free path of electrons in the gas, enhancing their energy and thus the first Townsend coefficient. This effect can be exploited in low pressure detectors to initiate a preamplification stage in the conversion gap itself.

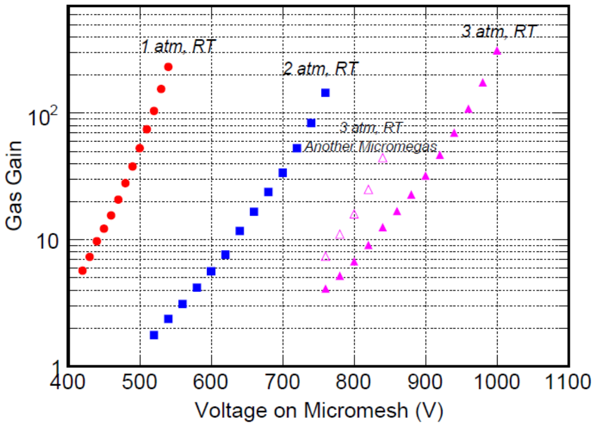

Figure 2.13: *Measured gains in a Micromegas detector for different Xenon gas pressures at room temperature (RT) [63].*

The question of the gain fluctuations on a given detector, or between identical detectors, is a delicate issue. Large variations of the order of 20-30% are often reported, and originate from fluctuations of the amplification gap, which themselves may result from inhomogeneities during the lamination process. According to a Garfield simulation, 20% variations of the gain corresponds to only 5% inhomogeneities of the amplification gap, *i.e.* generally a few microns [7].

2.4.2 Electron transparency

The electron transparency η is defined as the probability for an electron created in the conversion volume to pass in the amplification gap through the holes of the micro-mesh. An effective gain is sometimes introduced as the product ηG, as the transparency directly affects the total charge induced on the readout anode. It has been observed very early that η primarily depends on the amplification to conversion field ratio E_a/E_d [8], reaching a value close to 100% if this ratio exceeds roughly 50, for which the funnel effect is maximal (see Fig. 1.1). For smaller values of the field ratio, the transparency drops significantly, as shown in Fig. 2.14 (left). The highest transparency being close to 100%, it is experimentally evaluated by measuring the gain at different drift electric fields, and by normalizing it to the maximal value. Fig. 2.14 (left) further reveals that in the case where large drift electric fields are required, the electron transparency can be enhanced by choosing a loose mesh. The length of the transparency plateau is also modified by the gas mixture, and more precisely by the quencher concentration. This effect, presented in Fig. 2.14 (right), seems to originate from the diffusion coefficients. A reduced diffusion indeed tends to tight electrons close to the field lines, and then to maximize the funnel effect.

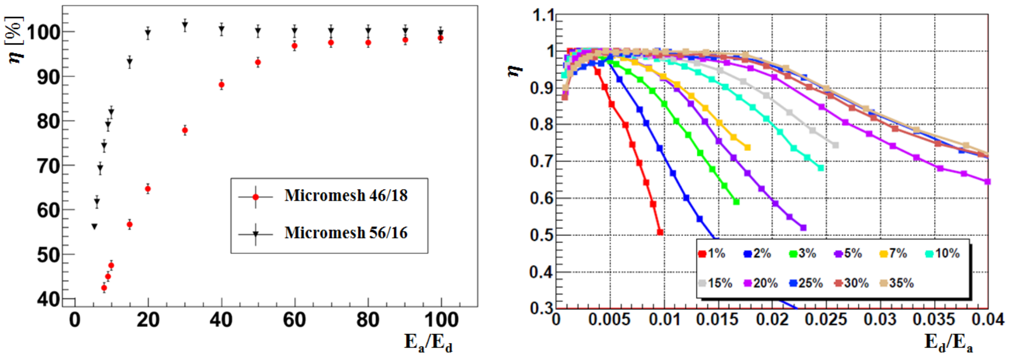

Figure 2.14: *Electron transparency as a function of the electric field ratio for a bulk with different micro-meshes [65] (left) and for a microbulk with different Argon-Isobutane gas mixtures [61] (right). A 46/18 micro-mesh corresponds to 46-micron pitch and 18-micron wire diameter.*

---

[7] even when the amplification size is close to the theoretical value which minimizes gain fluctuations

[8] This is actually not exactly true, as pointed out in [64].

2.4.3 Energy resolution

At high energies, the Micromegas as other gaseous detectors has limited energy resolution and particle identification capabilities, because of the low ionization yield and its large fluctuations. For the detection of low energy particles and photons, however, all the energy of the particle can be released in the gas volume, and energy measurements become competitive.

In general, the energy resolution σ_E/E can be expressed as a sum of independent terms, namely the primary electrons fluctuations, the gain variations and the noise term. Following [60]:

$$\left(\frac{\sigma_E}{E}\right)^2 = \left(\frac{\sigma_{N_0}}{N_0}\right)^2 + \frac{1}{N_0}\left(\frac{\sigma_G}{G}\right)^2 + \left(\frac{\sigma_{noise}}{GN_0}\right)^2, \tag{2.4}$$

where σ_{noise} is the noise level at the electronic input, N_0 the mean number of primary electrons and G the average gain. The variance of N_0 can be expressed as:

$$\left(\frac{\sigma_{N_0}}{N_0}\right)^2 = \frac{F}{N_0}, \tag{2.5}$$

where F is the **Fano factor** [66] accounting for the reduction of the ionization number fluctuations ($F < 1$). By neglecting the noise term and writing f the relative gain variance, we obtain:

$$\frac{\sigma_E}{E} = \sqrt{\frac{f + F}{N_0}} \tag{2.6}$$

For a standard Argon-Isobutane mixture (95-5%), numerical values (F≈0.2, f≈0.3) lead to a minimal energy resolution of the order of 5% (RMS) with a Fe^{55} source. Measurements with bulk Micromegas are generally slightly above this value (20% FWHM or 8.5% RMS) which point to additional fluctuations because of the woven micro-mesh structure. A recent Garfield simulation of a bulk predicted an energy resolution of around 7% [67], not too far from the best measurements. In the case of the micro-bulk however, resolutions of 11.6% FWHM (4.9% RMS) have been reported, showing that this detector practically reaches the theoretical limit.

To be complete, the energy resolution has also been investigated for curved bulk Micromegas with a Fe^{55} source. As shown in Fig. 2.15, the resolution is found to degrade at low radius for which the sagitta of the micro-mesh between pillars probably enhances gain variations.

2.4.4 Efficiency

The efficiency is simply defined as the probability to detect a given particle and depends on many parameters, in particular through its strong correlation with the S/N ratio:

- the particle type, charge and energy;

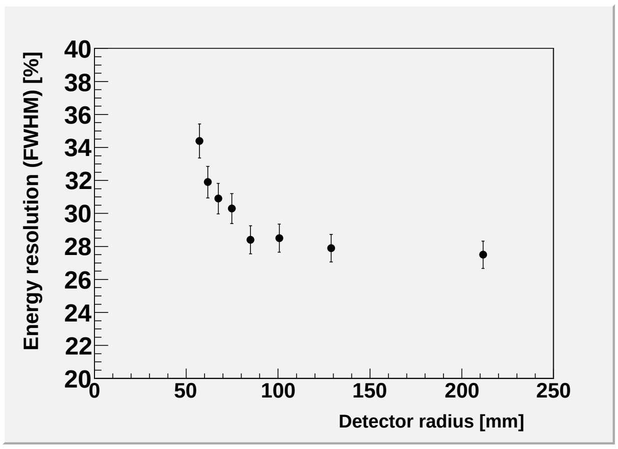

Figure 2.15: *Energy resolution of an early curved bulk Micromegas as a function of its curvature.*

- the detector gain or amplification field;
- the readout electronics;
- the environment, *e.g.* the noise level or the particle flux.

In practice, the efficiency ϵ is often evaluated either from a beam or from cosmic rays. With a sample of n particles crossing the detector active area:

$$\epsilon = \frac{p}{n}, \tag{2.7}$$

with p the number of particles really detected. For a given set of tracks, the efficiency error is given by the **Bernoulli distribution**:

$$\sigma_\epsilon = \sqrt{\frac{\epsilon(1-\epsilon)}{n}} \tag{2.8}$$

The track sample is usually selected by reference detectors placed in the vicinity of the detector to be tested. Each particle trajectory is reconstructed in these references and its extrapolated position on the test detector is compared with a potential hit nearby. The maximal distance allowed between the track and the hit depends on the tracker and detector resolutions. In order to avoid any bias in the efficiency measurement, no significant correlation should exist between the signals in the different detectors. Such a situation can occur when the sample is built from particles with different energies, leading to different mean ionization yield in the detectors. In this case, the measured efficiency may be slightly overestimated.

In a given configuration, the efficiency is expected to be close to a step function of the gain, expressing a threshold effect. In practice however, statistical fluctuations from ionization, amplification and noise smoothen this function into a typical s-shape curve ending with a plateau. For charged particles, plateaux higher than 95% are routinely achieved with Micromegas. The length of the plateau determines the operation margin, and in particular the nominal discharge probability. It should be stressed that the plateau is often modified in the real experiment compared to the test lab. Higher noises indeed translate the efficiency curve to higher fields, and the presence of highly ionizing particles reduces the maximal high voltage accessible. Last but not least, the plateau value can be lowered for very high particle fluxes.

Beyond the average value, the efficiency may also vary with the position in the detector because of inhomogeneities. Most of them result from defects occuring at the manufacturing process stage, *e.g.* cut strips during etching or a larger amplification gap due to detached pillars. In some cases, gas leaks or gas circulation issues can also locally alter the efficiency.

2.4.5 Spatial resolution

The spatial resolution σ_{det} of a detector characterizes its accuracy to reconstruct the particle position, and largely determines the tracking performance of a spectrometer. Individual signals above strip thresholds are first identified (hits), and neighbours are grouped into clusters whose positions x_{det} are defined as the average strip position x_i weighted by the signal amplitude s_i:

$$x_{det} = \frac{\sum_i s_i x_i}{\sum_i s_i} \tag{2.9}$$

Using the same method described in the previous section for the efficiency, the extrapolated track position x_{tr} is compared to the cluster position to form the residual $r = x_{tr} - x_{det}$. The width σ of the residual distribution is thus simply the quadratic sum of the track and detector resolution. In the common case where reference detectors are identical to the test detector, the spatial resolutions are assumed to be the same and can then be extracted. For example, if the test detector is placed at the middle of the references, the residual writes:

$$r = \frac{1}{2}\left(x_{ref1} + x_{ref2}\right) - x_{det} \tag{2.10}$$

leading to the following relation between residual width and spatial resolution:

$$\sigma^2 = \frac{1}{4}\left(\sigma_{det}^2 + \sigma_{det}^2\right) + \sigma_{det}^2 = \frac{3}{2}\sigma_{det}^2 \tag{2.11}$$

In reality, the measured raw residual width is often higher than this value because of various misalignments between references and the test detector. These misalignments translate into correlations between the residual and specific parameters like the track angle or position. For example, a misalignment Δz of the test detector along its perpendicular axis z develops the following correlation:

$$r = \Delta z \times \tan(\theta_{xz}), \tag{2.12}$$

where θ_{xz} is the track angle in the $x - z$ plane, x being the axis perpendicular to readout elements. This type of global misalignment is not intrinsic to the detector, and an offline alignment procedure can be implemented to correct for these effects (see Chapter 3). Local misalignment can also exist, coming *e.g.* from the non planarity of the PCB. In this case, realignment is more complex, and the remaining effect may be accounted in the global resolution of the detector which becomes a quadratic sum of the intrinsic resolution and residual misalignments. To fully benefit from the detector capabilities, it is therefore desirable that the uncorrected misalignments represents only a fraction of the intrinsic resolution.

The intrinsic resolution is closely related to the granularity of the anode plane. When the signal of a particle is recorded on a single readout element, the spatial resolution is simply $p/\sqrt{12}$, p being the pitch of the elements. Because of the transverse diffusion in the gas, a normally incident particle often leaves a signal on several neighbouring elements. The weighted average of the element positions thus yields a better resolution than the single hit case. For example, the Compass Micromegas reach 70 micron resolution at low flux with $p/\sqrt{12}$ of the order of 100 microns and a mean cluster size around 2.5 [68]. This last value is close to the optimum, as higher transverse diffusion would also be accompanied by larger statistical fluctuations in the position estimate as well as smaller S/N ratio for individual elements. In the case where the particle trajectory is not perpendicular to the detector, the spatial resolution extracted from Eq. (2.9) exhibits a strong dependence with the track angle, and can double with angles as low as 20-30°. Instead, a so-called micro-TPC algorithm using the time of the different signals allows to obtain a quasi angle-independent resolution [69, 70].

Finally, the presence of an external magnetic field B can also slightly modify the detector resolution. When B is parallel to the electric field, the transverse diffusion and the cluster size are reduced, and the resolution approaches the single strip limit [9]. When the drift distance is long (TPC mode), large transverse diffusion degrades the resolution and a focusing B field is generally used to reduce the cluster size close to its optimum. On the other hand, a transverse magnetic field systematically degrades the spatial resolution because of the charge spread and the associated statistical fluctuations of the primary electron positions. More complex effects also develop, like an asymmetric resolution for positively and negatively charged particles [71].

2.4.6 Time resolution

The time resolution σ_t plays a very important role in modern experiments as it often determines the particle flux a spectrometer can stand, and therefore the available statistics for processes of interest. High flux experiments are indeed characterized by large background rates, and the time selection of hits greatly influences the tracking performance and its CPU consumption. The number of bakground hits to be considered for the track finding procedure is directly proportional to the time resolution of a given detector, and impact both its efficiency and purity [10]. Large background rates also degrade the track reconstruction by enhancing the probabilities of ambiguities or so-called *sister tracks*.

---

[9] unless the pitch is lowered accordingly to maintain the same cluster size, in which case the final resolution can be significantly improved

[10] *i.e.* the proportion of fake reconstructed tracks

The time measurement in a Micromegas varies with the readout electronics and the recorded information. It can be simply extracted from the starting and ending times of the signal, or fitted from the signal shape in the case of a sampling electronics. In the latter case, different fitting methods exist, *e.g.* the raising slope, the maximum, or even a correlation function. The times determined for each signal of a given cluster may then be mixed to further improve the estimation. The distribution of the difference between the measured time and a reference (trigger) is then formed, and its width σ verifies:

$$\sigma = \sqrt{\sigma_t^2 + \sigma_{trig}^2}, \tag{2.13}$$

with σ_{trig} the trigger resolution. In many cases this last term is either known or can be safely neglected. It is also common to use 2 test detectors simultaneously and consider only the time difference distribution, to get rid of the trigger contribution.

The resolution σ_t extracted from the previous equation is *a priori* a convolution of the electronics and the intrinsic detector resolutions. The first contribution can be measured with a pulser, and is often of the order of 1 ns with modern electronics. The detector part, typically 10 to 20 ns, is mainly determined by the drift velocity and the longitudinal diffusion, which in turn depend in a non trivial way on the gas mixture and the drift electric field. Simulations or dedicated studies are thus often required to optimize the resolution. In general better time resolutions are obtained with light noble gases, with the admixture of polyatomic quenchers to enhance the drift diffusion (see Chapter 1). Among these quenchers, CO_2 and CF_4 are particularly performant, and it was observed that a 10% concentration of CF_4 can lower the time resolution from 15 to 10 ns in a Neon based gas. Electric fields maximizing the drift velocities can also bring significant improvements, as illustrated in Fig. 2.16.

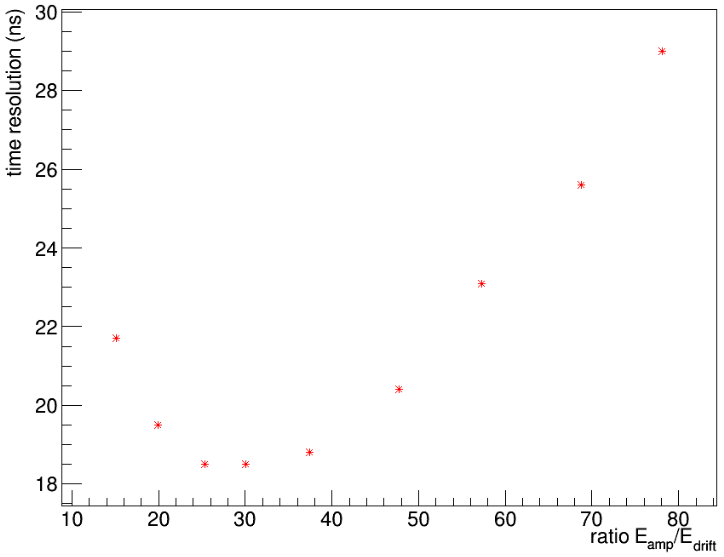

Figure 2.16: *Time resolution of a Clas12 Micromegas detector as a function of the electric fields ratio at constant amplification field, in a Argon-Isobutane (90-10%) mixture [72].*

2.5 Specific performance of resistive Micromegas

Resistive films were initially introduced to spread the charges on several readout elements and were later employed as a discharge quencher in Micromegas. Since the resistive strip development at Cern in 2010 [51] many prototypes have been built to validate the performance before this technology can equip future experiments. The significantly higher gains it offers without any ageing effect as well as its peculiar behaviour in the presence of dust will be described in the next sections.

2.5.1 Gain and efficiency

In a non resistive detector the maximal amplification field never reaches the dielectric strength of the gas, even in the absence of highly ionizing particles. This originates from unavoidable local defects in the amplification gap, and it is frequently seen that at the highest possible field discharges don't occur randomly but at specific positions in the detector. On the contrary the discharge quenching offered by resistive films absorbs these local small defects into a small harmless current circulating between the micro-mesh and the resistive ink. Higher voltages and gains are thus possible, as illustrated in Fig. 2.17 for a Micromegas flushed with a Argon-Isobutane (95-5) mixture. The detector showed stable operation at gains up to 70000, *i.e.* more than 2 times larger than the same detector without the resistive film [11]. Above this value, an unstable current appeared at the 10-100 nA level. The measurement of the micro-mesh current through a decoupling capacitance showed random, small bursts suggesting the accumulation of abundant micro-discharges. The change of slope visible on Fig. 2.17 further suggests that the detector approaches the limit between the proportional and the streamer regimes.

A direct consequence of the higher available gains is a significant increase of the length of the efficiency plateau, up to 40 V for large Clas12 detectors. It also permits the operation of detectors with much larger input capacitance, *i.e.* longer cables, multiplexing pattern (see Chaper 5) and bigger detectors. Alternatively, it can compensate for the signal loss due to the charge sharing in a 2D readout design in order to maintain the full efficiency in both directions. Such a technology may even be used directly in air with potential applications in dosimetry, and a 40% efficiency to MIP was reported with a small detector [73].
Last but not least, the discharge quenching by the resistive film provides a natural protection of the readout electronics to current bursts, and therefore plays the same role as the protection circuit often used for this purpose. Modified FE cards without this circuit were tested and did not suffer from any damage on the chips even at the highest gains. The comparison with protected cards showed a simultaneous increase of the signal and noise, with an overall improvement of 15% and up to 35% on S/N for the Clas12 detectors. This effect corresponds to a shift of the efficiency plateau by almost 10 V, as seen in Fig. 2.18.

---

[11] for which discharges started to occur at gains around 30000

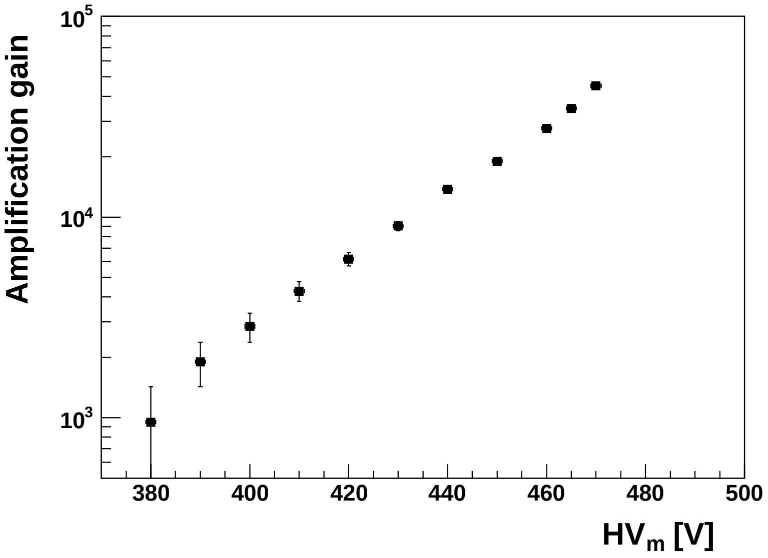

Figure 2.17: *Gain measurements of a resistive Micromegas as a function of the micro-mesh high voltage, in a Argon-Isobutane (95-5%) mixture. Gains of 50000 were obtained with the* Fe^{55} *source, and up to 70000 without it.*

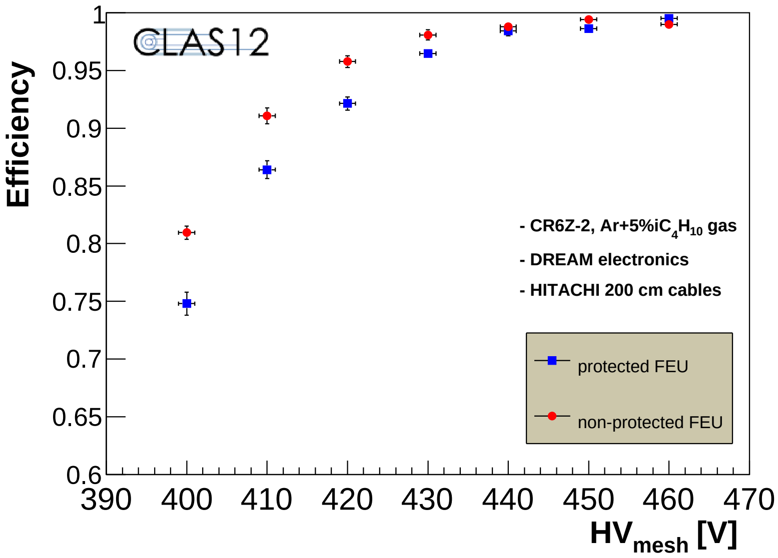

Figure 2.18: *Efficiency plateau of a resistive Micromegas equipped with protected and unprotected FEU (Dream electronics).*

2.5.2 Ageing and high fluxes

In parallel of these promising measurements, the long term behaviour of the resistive film was investigated and in particular the resulting gain stability and the discharge protection ability. Ageing effects were looked for with alpha particles [74], X-rays, neutrons, gammas and pion beams, with no hint of damage. In particular, the gain was found to remain stable during intense X-ray radiations, as shown in Fig. 2.19, corresponding to several years of operation of the Atlas New Small Wheel at the sLHC luminosity [75]. Similarly, resistive films were not degraded after 1.5×10^6 discharges provoked by an Am source, equivalent to more than 5 years in the Clas12 conditions.

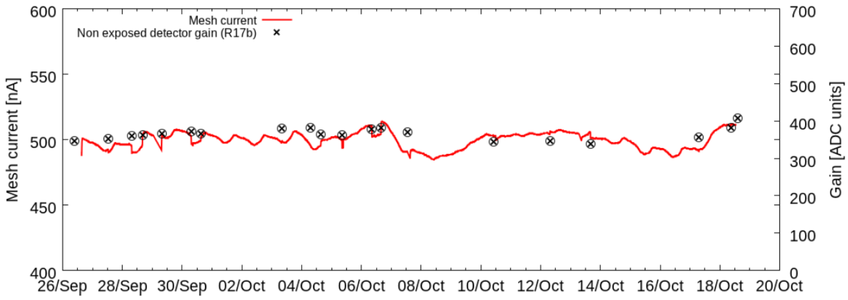

Figure 2.19: *Gain evolution of a resistive Micromegas under intense X-ray radiations, with a total exposure of 918 mC. Black dots correspond to measurements of a non exposed reference detector.*

At high fluxes of particles significant currents may develop between the micro-mesh and the resistive film. With a typical resistance of the order of $10\,\mathrm{M}\Omega$, a $1\,\mu$A current corresponds to a local voltage drop of 10 V, an effect which has a strong impact on the gain. Such a saturation effect has been revealed with intense X-ray source via the micro-mesh current measurement, as shown in Fig. 2.20 [76]. The integration of ladders between the readout elements attenuates this saturation by lowering the effective resistance and spreading the charge evacuation.

The remarkable performance described in the previous sections decided several collaborations to choose the resistive technology for their future upgrades, and in particular for the Atlas NSW and the Clas12 vertex tracker. We will see below that a few questions should still be issued, though they don't jeopardize the promising future of this technology.

2.5.3 Effects of dust

We have seen in Section 2.2.1 that dust or other defects may be burnt or dried in standard Micromegas by a specific *cooking* of the detector. This technique relies on heating with discharges circulating through the defect, and therefore can not work with a resistive film. In spite of careful cleaning and thermal cooking before the final integration of the detectors, resistive prototypes may suddenly exhibit relatively large currents after a few days of running, from 3 to $50\,\mu$A depending on the detectors. This is often accompanied by an abnormal increase of the noise of one or two neighbouring strips, see Fig. 2.21 (left). In the case of detectors with resistive ladders an extended unefficiency area also develops, delimited by the closest HV connections of the film, as illustrated in Fig 2.21

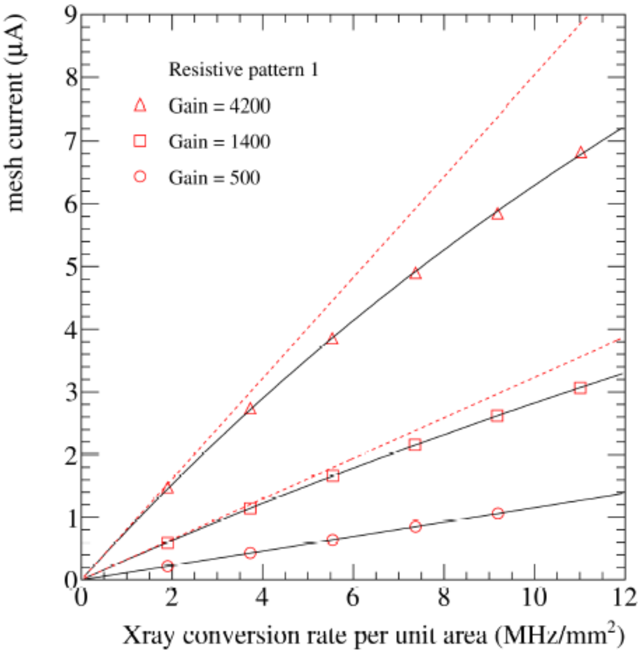

Figure 2.20: *Micromesh current as a function of the X-ray flux, showing non linearity at high gains.*

(right). A careful inspection with a UV camera usually reveals the presence of a hot spot where the current leaks, proving that the defect originates from a dust or any point-like fragment falling in the holes of the micro-mesh. If needed, the spot can be neutralized by the insertion of a liquid insulator (polyurethane) with minimal impact on the efficiency. Such a repair requires an access to the detector inside, but stays compatible with the bulk technology.

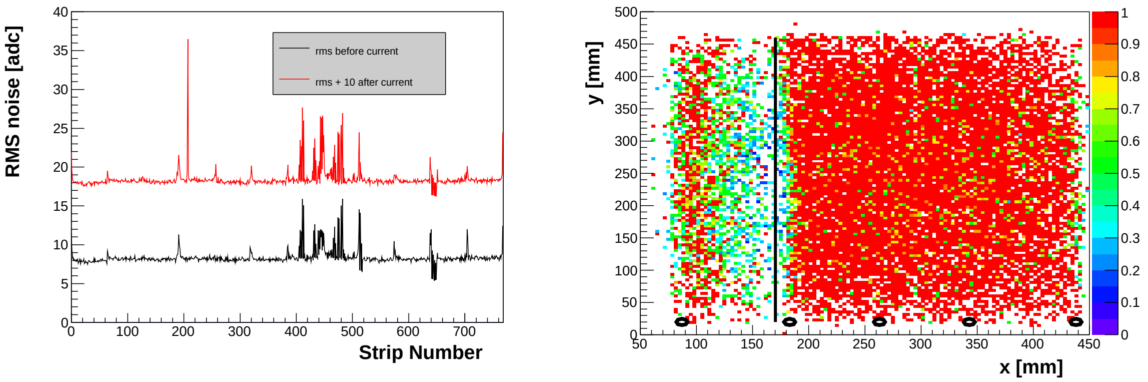

Figure 2.21: *(Left): noise level in the same detector before and after the current appears. (Right): 2D efficiency of a (ladder) resistive Micromegas with a large current between the micro-mesh and the resistive strips. Black circles indicate HV contact of the resistive film, and the black line the location of the noisy strip.*

2.5.4 Time resolution

Another problem reported with the resistive technology is the degraded time resolution of such detectors which can be an issue for high flux experiments. This effect was first observed with Compass prototypes where resolutions as bad as 30 ns were measured, and led to the choice of hybrid GEM-Micromegas for the Compass-II upgrade [77]. Recent investigations revealed that the degradation probably originates from 2D inhomogeneities of time measurements in the detector, as seen in Fig. 2.22. The source of these fluctuations are still unknown but may arise from resistivity variations along the film, suggesting that the serigraphy process is not yet optimized. Meanwhile, such inhomogeneities can be tabulated in 1D or 2D and corrected offline.

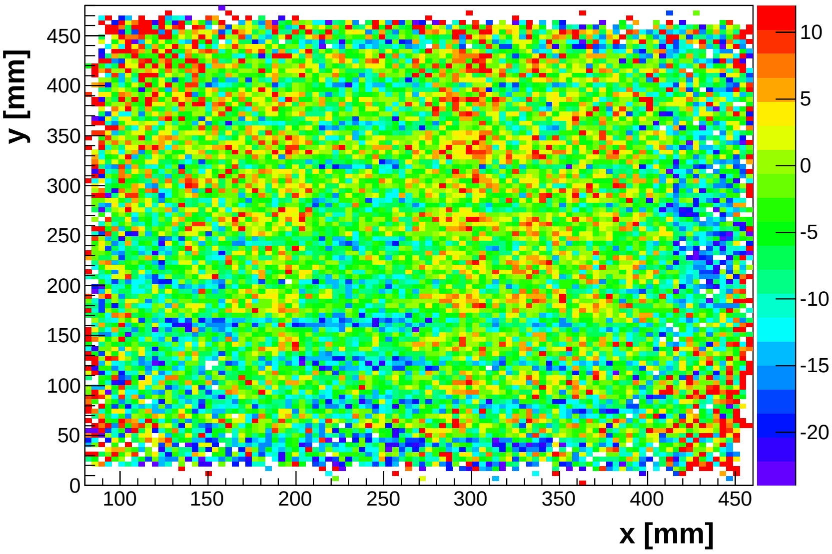

Figure 2.22: *2D distribution of the signal time (in ns) in a resistive Micromegas, obtained with cosmic data.*

Chapter 3

Elements of tracking and reconstruction

Though tracking issues are much more general than Micromegas detectors and are the subject of numerous specialized books, this chapter will present basic principles of track reconstruction. It is indeed essential to better understand the importance of detectors characteristics, like spatial and time resolutions, radiation length and even alignment. The tracking also makes the link with physics analysis, and its knowledge thus provides a more comprehensive view of experimental particle physics.

3.1 Introduction to tracking

The main goal of the tracking in an apparatus is to provide a list of tracks from each trigger for physics analysis. These tracks are defined by parameters estimated at the vertex position. Numerous methods have been developed with years to optimize the tracking which is traditionally splitted in at least two steps:

- the **track finding** whose role is to identify patterns which are compatible with trajectories
- the **track fitting** which calculates the track parameters from the selected patterns

The need of a separate, fast, fit free track finding is easy to understand, as it would be unrealistic to send to the fitter all the combinations of hits.
At the very high fluxes of modern experiments, several events can be recorded within a single trigger and the tracking therefore includes a third process during which tracks are associated into vertices. This is also relevant when the reactions of interest involves unstable particles which further decays after a measurable distance (secondary vertices).
These different steps will be reviewed in the next sections, as well as the tracking performance. The effect of the detectors characteristics, the background level as well as misalignments will also be discussed.

3.2 Track finding

In the early days of particle physics, track finding was ensured by human eye scrutinizing photographs from bubble or cloud chambers. The flux was generally so low that no special skills were required to recognize trajectories. Besides, the human eye — and the brain behind — has outstanding capabilities to identify patterns in a given picture, though with a very limited cadence. With the advent of electronic readouts and the increase of particle fluxes, humans had to be replaced by algorithms to perform this task at a much higher frequency. It turns out that the field of pattern recognition exceeds by far the needs of particle physics, and several algorithms were adapted from other situations. Because of the multitude of cases, it exists nowadays a large variey of such algorithms which however can be classified in two main categories: local and global methods.

3.2.1 Local methods

Standard local algorithms start in a small area of the whole pattern, typically with one or a few neighbouring hits acting as a seed which is grown using the estimated track pattern - straight line, helix, etc. The rough track is extrapolated at the next detection layer and compared with available measurements. If one or several hits are compatible with this extrapolation, they are included in the seed and the search goes on. If no hits are found, the track may be extrapolated to the next layer or abandoned according to the number of passed layers without suitable measurements. The exact growing of the seed depends on the geometry of the apparatus. It can be linear if detectors are placed at regular distances. It can also form bigger structures, like clusters of hits, or mini track segments in different groups of detectors. This is illustrated in Fig. 3.1 featuring a single track in the Clas12 Drift Chambers with some background. The progressive identification of structures at different scales eventually leads to a unique track segment.

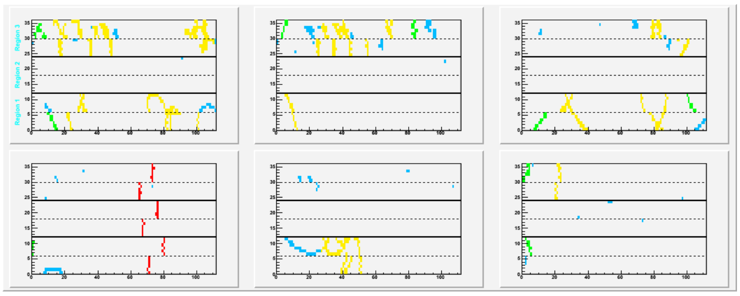

Figure 3.1: *Hit display of a simulated Clas12 event with an electron and full luminosity in the six sectors of the Drift Chamber tracker, composed of 3 regions of 12 layers each. Isolated hits are in blue, half region clusters in green, full region segments in yellow and complete track candidate in red. Both human eye and the algorithm identify the electron track.*

This method is iterative by nature, the algorithm being run again over all the possible seeds. Hits from a previously identified track candidate may or may not be removed from

the pattern. Hit removal speeds up the finding process, but with a risk of unefficiency if several tracks share a given hit and the redundancy is not high enough. The final choice to remove these hits is made on the comparison of both methods or on a simulation, and depends primarily on the occupancy of the readout elements.
Local algorithms can be easily customized to any apparatus and are therefore widely used in tracking. However they suffer from a lack of robustness, in particular when dead zones appear during the data taking. Their use also becomes delicate when the spectrometer is built from distant groups of detectors, with a loose extrapolation between them. Finally, they are generally highly time consuming, with a number of operations growing faster than the number of hits n.

3.2.2 Global methods - example of the Hough transform

Global methods, on the other hand, consider the list of hits as a whole, with a number of operations that is linear with n. They also better resist to the appearance of dead areas, provided that the redundancy is large enough. A particularly efficient algorithm makes use the **Hough Transform** (HT), initially developed in 1959 for the analysis of bubble chambers photographs. The HT converts a point (hit) in a given object space into a curve in an image space. The curve defines the relation between the parameters of all possible, fixed pattern (*e.g.* a circle) crossing the initial point. Therefore, a set of points lying on the same pattern will have their image curves crossing at the same point in the image space. The coordinates of this point simply correspond to the parameters of the pattern.
The HT was applied to the Clas12 Central Tracker for the search of quasi-circles in the plane transverse to the field and beam axis [78]. For a given point P of this plane, it exists an infinity of circles crossing both P and the origin (the beam spot). These circles can be parametrized by their center coordinates x_C and y_C. If a and b are the coordinates of P, it is easy to show that:

$$a x_C + b y_C = \frac{a^2 + b^2}{2}, \tag{3.1}$$

i.e. the point P converts into a straight line in the space spanned by x_C and y_C. The Fig. 3.2 (top left) shows the object and image spaces for a proton track initiating from the target. For simplicity all detectors were chosen to be purely cylindrical. As can be seen in Fig. 3.2 (top right), the four curves indeed intersect at the same point in the image space, determining the circle position. The HT thus allows to convert the pattern finding into the search of an intersection point. With an appropriate binning of the image space [1] this problem is equivalent to find a maximum, which is visible in Fig. 3.2 (top right). For illustration, the same transform is performed in a case where the proton track is polluted with a 150 MHz (uncorrelated) background, see Fig. 3.2 (bottom). The HT identifies only three track candidates with a very small number of operations, when a local method would have to test numerous seeds.

---

[1] to take into account that the track is not a perfect circle

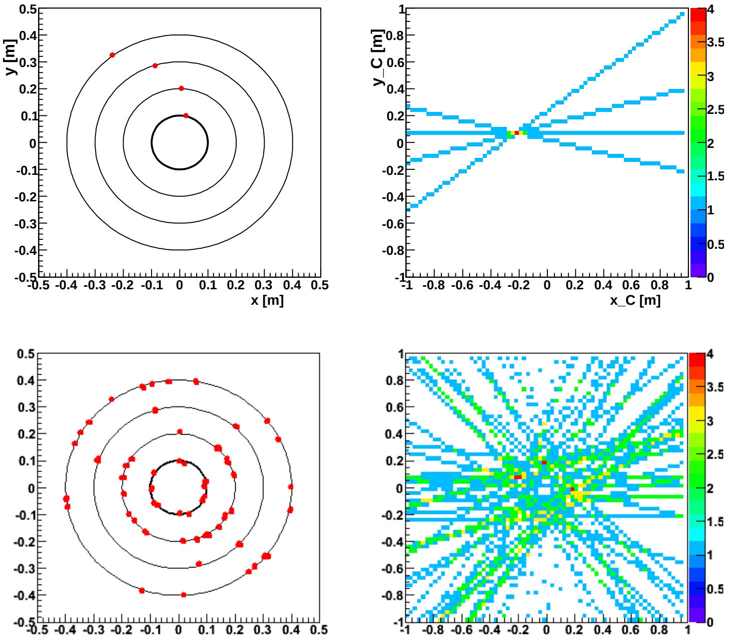

Figure 3.2: *(Top): Illustration of the Hough transform for a proton track in a cylindrical tracker (left) made of four layers, with its associated image plane (right). The four lines intersect at the coordinate of the track center. (Bottom): same event, with an uncorrelated 150 MHz background. Only three track candidates are identified in spite of the high hit density.*

3.3 Track fitting

Once a set of hits or measurements $\{m_i\}_{i=1,2,\ldots,N}$ has been identified to come from a single particle, a fitting procedure is applied to determine the parameters of the track, in particular at the vertex position. These parameters are expressed in terms of a state vector $\mathbf{x}$, whose components are usually chosen according to the geometry of the spectrometer. Four components are enough to describe a straight track, but in the presence of magnetic fields a fifth one should be added to take into account the track curvature. The relation between $\{m_i\}_{i=1,2,\ldots,N}$ and $\mathbf{x}$ can be established by different types of algorithms which in general have to satisfy two main criteria:

- non bias estimation $\langle \mathbf{x_{fit}} \rangle = \mathbf{x_{true}}$
- minimal variance (best estimator): $\sigma^2(\mathbf{x_{fit}}) = \langle (\mathbf{x_{fit}} - \mathbf{x_{true}})^\mathbf{2} \rangle$ minimal

3.3.1 The Least Squares Method

A simple algorithm generally fullfilling these two criteria is based on the Least Squares Method (LSM) which provides a global, thus fast, track fitting through a χ^2 minimization.

the LSM is particularly adapted in cases where multiple scattering and energy loss can be neglected. It is derived from the assumption that the measurements can be expressed as a linear function of the state vector given by the particle equation of motion:

$$\mathbf{f}(\mathbf{x}) = \mathbf{f}(\mathbf{x_0}) + \mathbf{A}.(\mathbf{x} - \mathbf{x_0}) + \mathcal{O}((\mathbf{x} - \mathbf{x_0})^{\mathbf{2}}) \tag{3.2}$$

In addition to the set of measurements $\mathbf{m}$, an error (or covariant) matrix $\mathbf{V}$ should be formed to take into account the measurements uncertainties. A weight matrix $\mathbf{W}$ is commonly introduced and defined as the invert of $\mathbf{V}$. When the different measurements are uncorrelated, $\mathbf{W}$ is diagonal with components related to the spatial resolutions σ_i of the individual detectors:

$$W_{ij} = \delta_{ij}/\sigma_j^2 \tag{3.3}$$

For a given set of measurements $\mathbf{m}$, the χ^2 writes:

$$\chi^2 = (\mathbf{f}(\mathbf{x_0}) + \mathbf{A}.(\mathbf{x} - \mathbf{x_0}) - \mathbf{m})^T \, \mathbf{W}. \, (\mathbf{f}(\mathbf{x_0} + \mathbf{A}.(\mathbf{x} - \mathbf{x_0}) - \mathbf{m}) \tag{3.4}$$

The LSM consists is minimizing it in $\mathbf{x}$, leading to:

$$\mathbf{x_{fit}} = \mathbf{x_0} + (\mathbf{A^T W A})^{\mathbf{-1}} \mathbf{A^T W}.(\mathbf{m} - \mathbf{f}(\mathbf{x_0})) \tag{3.5}$$

This expression simply requires the inversion of a 5×5 matrix (in the case of magnetic field).
In some cases, the χ^2 can be derived analytically without any linearization. For example, a particle in a homogeneous magnetic field along the z axis follows at first order a helix track:

$$\begin{aligned} x &= x_0 + \frac{p_{x0}}{qB} \sin \omega t - \frac{p_{y0}}{qB} (\cos \omega t - 1) \\ y &= y_0 + \frac{p_{y0}}{qB} \sin \omega t + \frac{p_{x0}}{qB} (\cos \omega t - 1) \\ z &= z_0 + \frac{p_{z0}}{m} t, \end{aligned} \tag{3.6}$$

with usual notations and $\omega = qB/m$. If cylindrical detectors are placed concentrically around the particle emission area (target), one obtains [71]:

$$\chi^2 = \sum_{i=1}^{n} \frac{\left(\sqrt{(x_i - p_1)^2 + (y_i - p_2 - p_3)^2} - p_3 \right)^2}{\sigma_{x,i}^2} + \frac{\left(z_i - p_4 - \frac{p_5}{qB} \arccos \left(1 - \frac{x_i^2 + y_i^2}{2 p_3^2} \right) \right)^2}{\sigma_{z,i}^2}, \tag{3.7}$$

where x_i, z_i are the detectors measurements with their corresponding resolutions $\sigma_{x,i}$ and $\sigma_{z,i}$, y_i being determined from x_i and the detector's surface. The p_i are the parameters of the track: the circle in the plane perpendicular to B has center (p_1,p_2+p_3) and radius p_3, p_4 is the z position of the vertex, and p_5 the momentum along z axis. Any minimization program, *e.g.* Minuit [79], can be called to minimize this expression and provide an estimate of the p_i.

Though this example is not fully realistic, such an algorithm can be rapidly implemented to check the overall performance of a tracker layout, provided that the kinematics of interest is not completely dominated by multiple scattering effects. This is illustrated in Fig. 3.3 showing the obtained resolutions in momentum and vertex positions for different combinations of detectors (Micromegas and Silicons) of the Central Tracker of Clas12 [71].

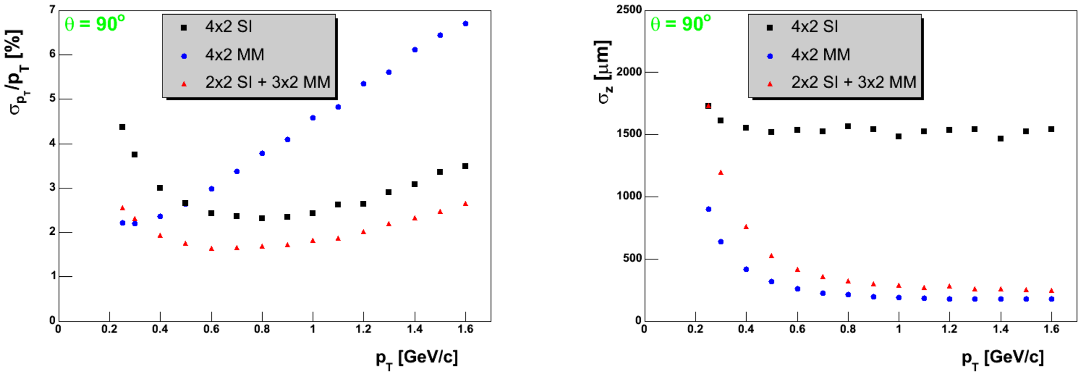

Figure 3.3: *Resolution in momentum (left) and vertex position (right) for various combinations of Silicon and Micromegas in the Clas12 Central Tracker. Tracks are perpendicular to the beam axis, and fitted with helix from Eq. (3.6).*

In general, the LSM starts to be more complex when measurement errors become correlated. Though the measurements themselves are independent, a correlation arises when the particle experiences multiple scattering along its trajectory. In this case, a correct computation of the non diagonal terms of the $n \times n$ matrix $\mathbf{V}$ is delicate, not to mention its inversion time which grows like n^3. The treatment of the energy loss is also not adapted, and progressive algorithms following the particle trajectory are prefered.

3.3.2 The Kalman Filter

Basic principles

The **Kalman filter** was developed in 1960 [80] and used for the first time in the Apollo program. It provides a recursive way to estimate the state of a system evolving in space and time by using discrete, noisy measurements and minimizing the corresponding χ^2. It has nowadays numerous applications from GPS to weather forecast, and was introduced in particle tracking in the mid 1980s [81, 82, 83]. In this framework, multiple scattering identifies to a noise term and can thus naturally be taken into account. If we note $\mathbf{x_k}$ the state vector at some discrete step k where a measurement $\mathbf{m_k}$ is available. The m-vector $\mathbf{m_k}$ is related to $\mathbf{x_k}$ via some unitary transformation that can be written:

$$\mathbf{m_k} = \mathbf{H_k} \cdot \mathbf{x_k} \tag{3.8}$$

The state of the system, extrapolated to a next step (in practice, to the next measurement), is then defined as:

$$\mathbf{x_k^{k+1}} = \mathbf{F_k} \cdot \mathbf{x_k}, \tag{3.9}$$

where $\mathbf{F_k}$ is some known propagation operator, based on the local equation of motion. At the step $k+1$, the algorithm has to perform an update of the system state, using both extrapolated vector (*i.e.* all previous measurements) and the current measurement. Writing $\mathbf{C_k}$ (resp. $\mathbf{M_k}$) the covariant matrix of $\mathbf{x_k}$ (resp. $\mathbf{m_k}$), and defining the covariance matrix of the extrapolated state $\mathbf{x_k^{k+1}}$:

$$\mathbf{C_k^{k+1}} = \mathbf{F_k} \cdot \mathbf{C_k} \cdot \mathbf{F_k}^T + \mathbf{Q_k}, \tag{3.10}$$

with some noise matrix $\mathbf{Q_k}$, the χ^2 has the following expression:

$$\begin{aligned}\chi^2 = {} & (\mathbf{x_{k+1}} - \mathbf{x_k^{k+1}})^\mathbf{T} \cdot \left(\mathbf{C_k^{k+1}}\right)^{\mathbf{-1}} \cdot (\mathbf{x_{k+1}} - \mathbf{x_k^{k+1}}) \\ & + (\mathbf{H_{k+1}} \cdot \mathbf{x_{k+1}} - \mathbf{m_{k+1}})^\mathbf{T} \cdot (\mathbf{M_{k+1}})^{\mathbf{-1}} \cdot (\mathbf{H_{k+1}} \cdot \mathbf{x_{k+1}} - \mathbf{m_{k+1}})\end{aligned} \tag{3.11}$$

The minimization gives:

$$\mathbf{x_{k+1}} = \mathbf{C_{k+1}} \cdot \left(\left(\mathbf{C_k^{k+1}}\right)^{\mathbf{-1}} \cdot \mathbf{x_k^{k+1}} + \mathbf{H_{k+1}}^\mathbf{T} \cdot (\mathbf{M_{k+1}})^{-1} \cdot \mathbf{H_{k+1}} \cdot \mathbf{H_{k+1}}^\mathbf{T} \cdot \mathbf{m_{k+1}}\right), \tag{3.12}$$

with the updated covariance matrix:

$$\mathbf{C_{k+1}} = \left(\left(\mathbf{C_k^{k+1}}\right)^{-1} + \mathbf{H_{k+1}}^T \cdot (\mathbf{M_{k+1}})^{-1} \cdot \mathbf{H_{k+1}}\right)^{-1} \tag{3.13}$$

Though it implies a potentially long series of extrapolation and minimization steps, this framework requires only the inversion of matrices with sizes equal to the state vector dimension, *i.e.* usually 5.

Initialization

One can see from the previous section that a Kalman filter needs to be initialized, *i.e.* a starting state vector and its error matrix should be computed. Most of the time the filter is run backwards from the last measurement to the vertex location. Indeed the most precise information is obtained when all the measurements are included, and the track parameters are relevant only at the vertex location for physics analysis. As the last measurement provides only partial information on the position, the rest of the state vector has to be estimated with the list of hits selected during the track finding. This estimate is highly geometry-dependent. For example, in a central tracker with a solenoid field, a global fit with a helix can be performed *a priori* to feed the filter. In dipole configurations, straight track segments in low field regions provide the direction while the field integral between segments can be roughly estimated to access the momentum. In practice a precision of the order of 20-30% on the latter is enough to ensure a good convergence of the filter. If the state vector is poorly evaluated, the extrapolation to the previous detector may differ considerably from its actual measurement, and the filter tends to over-compensate with a risk of diverging zigzags around successive measurements. The initialization of the errors are less critical, and a diagonal covariant matrix with relatively large components often suffices.

Stopping condition

At the other extremity of the track, a stopping condition should be defined to end the extrapolation of the filter around the (yet) unknown vertex location. This is particularly important since an extra propagation of the track modifies its parameters. In the case of single track events, an external criterion has to be imposed based on the given setup, *e.g.* a minimal distance to a well collimated beam or the intersection point with a thin target. In the case of multi-track events, the stopping condition is less relevant, as a vertexing algorithm may be applied to form clusters of tracks (see Section 3.5.1).

Multiple scattering

As stated above, multiple scattering can be identified to a noise term in the Kalman filter framework. It modifies in particular the direction of the track. Assuming a thin layer of material and neglecting the energy loss, the momentum change writes

$$\begin{pmatrix} p_x \\ p_y \\ p_z \end{pmatrix} \rightarrow \begin{pmatrix} p_x \cos\theta_{MS} + \frac{p_y}{p+p_z}\left(p_y \sin\theta_{MS}\sin\phi_{MS} - p_x \sin\theta_{MS}\cos\phi_{MS}\right) + p_z \sin\theta_{MS}\sin\phi_{MS} \\ p_y \cos\theta_{MS} - \frac{p_x}{p+p_z}\left(p_y \sin\theta_{MS}\sin\phi_{MS} - p_x \sin\theta_{MS}\cos\phi_{MS}\right) + p_z \sin\theta_{MS}\cos\phi_{MS} \\ p_z \cos\theta_{MS} - \sin\theta_{MS}\left(p_x \sin\phi_{MS} + p_y \cos\phi_{MS}\right) \end{pmatrix}, \tag{3.14}$$

where θ_{MS} is the diffusion angle with respect to the incident direction and ϕ_{MS} a random azimutal angle. Alternatively, multiple scattering can be described in terms of two uncorrelated angles θ_1 and θ_2 in orthogonal planes. The noise matrix $\mathbf{Q_k}$ can then be expressed at each step k from the components x_i of the state vector [84]:

$$Q_{ij} = \sigma(\theta)\left(\frac{\partial x_i}{\partial\theta_1}\frac{\partial x_j}{\partial\theta_1} + \frac{\partial x_i}{\partial\theta_2}\frac{\partial x_j}{\partial\theta_2}\right) \tag{3.15}$$

The term $\sigma(\theta)$ is the standard deviation of the diffusion angle, which is commonly approximated by [6]:

$$\sigma(\theta) = \frac{13.6}{\beta c p} z \sqrt{\frac{l}{X_0}}\left(1 + 0.038\ln(l/X_0)\right), \tag{3.16}$$

where βc is the velocity of the particle, p its momentum in MeV/c, z its charge in electron unit, l the length of the crossed material and X_0 its radiation length.

Practical implementation: example of a central tracker

We give in this section some useful formulas to implement a Kalman filter in the case of a central tracker with cylindrical geometry. The case of a linear spectrometer along the beam axis being more common, similar formulas can be found easily in the literature.

The propagation matrix $\mathbf{F}$ between two measurements is obtained by expressing the evolution of the state vector between t and $t + dt$, and multiply all the corresponding matrices. The equation of motion simply gives:

$$\begin{pmatrix} z \\ \phi \\ p_x \\ p_y \\ p_z \end{pmatrix}_{t+dt} = \begin{pmatrix} 1 & 0 & 0 & 0 & \frac{dt}{m} \\ 0 & 1 & \frac{-ydt}{mr^2} & \frac{xdt}{mr^2} & 0 \\ 0 & 0 & 1 & \frac{qBdt}{m} & 0 \\ 0 & 0 & \frac{-qBdt}{m} & 1 & 0 \\ 0 & 0 & 0 & 0 & 1 \end{pmatrix} \begin{pmatrix} z \\ \phi \\ p_x \\ p_y \\ p_z \end{pmatrix}_{t}, \tag{3.17}$$

where $r = \sqrt{x^2 + y^2}$. This step by step propagation also allows for the correction of the mean energy loss, using the Bethe-Bloch formula (see Ex. 1.4) and the characteristics of the medium.

Cylindrical detectors measure exactly z and ϕ at a given radius, so the measurement matrix writes:

$$\mathbf{H_k} = \begin{pmatrix} 1 & 0 & 0 & 0 & 0 \\ 0 & 1 & 0 & 0 & 0 \end{pmatrix} \tag{3.18}$$

This expression can also be used when detectors provide only 1D information (strip), by attributing a very large error to the unmeasured component.

Finally the multiple scattering obtained from Eq. (3.15) can be written in the form:

$$\begin{pmatrix} 0 & 0 & 0 & 0 & 0 \\ 0 & 0 & 0 & 0 & 0 \\ 0 & 0 & p_y^2 + p_z^2 & -p_x p_y & -p_x p_z \\ 0 & 0 & -p_x p_y & p_x^2 + p_z^2 & -p_y p_z \\ 0 & 0 & -p_x p_z & -p_y p_z & p_x^2 + p_y^2 \end{pmatrix} \tag{3.19}$$

The vanishing components in the first two lines and columns express the fact that multiple scattering affects only the direction of the particle, and not its position.

3.3.3 Recent developments

As stated in the previous section, the Kalman filter possesses interesting features like small matrices inversion or a straightforward treatment of multiple scattering. On the other hand, it is based on two important assumptions which in certain cases may be inappropriate, with the consequence of deteriorating the estimation of the track parameters.

The first assumption is that all the processes at stake have Gaussian distributions. In reality non Gaussian tails arise through various processes, in particular the energy loss or multiple scattering. In some cases the detector measurements themselves may distribute on a sum of Gaussians. For these situations a relatively natural extension of the Kalman filter has been introduced [85, 86], where the distribution of the state vector $f(\mathbf{x})$ at any step is a sum of Gaussian components of mean value μ and covariant matrix $\mathbf{V_i}$:

$$f(\mathbf{x}) = \sum_{\mathbf{i=1}}^{\mathbf{n}} \mathbf{p_i} \phi(\mathbf{x}; \mu_\mathbf{i}, \mathbf{V_i}), \tag{3.20}$$

The potential gain of such an extension should be considered with the corresponding increase of the CPU consumption which is proportional to the number of components.
The Kalman filter as described above also assumes that the track finding process has selected only the hits coming from the current track. In very noisy environment the purity of the track finding may be degraded, as several neighbouring hits can compete. It is of course possible to let the Kalman filter decide which hit to consider in case of ambiguities - naturally the closest to its extrapolation - but this may bias the result in case of a loose initialization. Another approach consists in running several filters in parallel when an ambiguity occurs, and select the track with the best χ^2. However this becomes prohibitively time consuming when the hit density is large. Elegant solutions have been developped independently to overcome the problem of hit to track association:

- the Elastic Arms Algorithm (EAA [87]) makes use of statistical mechanics and defines an energy function expressing the cost of individual hits to belong to a given arm (track). To avoid local minimum in the minimization of this function, a temperature parameter T is introduced. The EAA starts at high temperature where hits can easily jump from one arm to another. When the temperature decreases, hits are slowly frozen to a given arm whose parameters are given by the energy minimization.
- the Deterministic Annealing Filter (DAF [88]) generalizes the Kalman Filter by assigning probabilities for each hit to belong to a given track. For a given set of probabilities, the algorithm runs a standard Kalman filter to determine the track parameters, which are in turn used to recalculate the hit probabilities based on their distance to the track. Similarly to the EAA, an annealing process is introduced through an additional term in the hit probabilities to avoid local minimum. Interestingly, the best performance is obtained at non zero temperature, *i.e.* with a fuzzy hit to track assignment.

It is worth mentioning that these algorithms tend to merge the finding and fitting processes which were largely independent in the early days of track reconstruction.

3.4 Tracking performance

3.4.1 Tracking resolutions

The track parameter resolutions depend on the detectors precision and on multiple scattering. Both contributions being independent, the final resolution is a quadratic sum of both terms. For example, the momentum resolution writes:

$$\sigma_p^2 = \left(\sigma_p^{det}\right)^2 + \left(\sigma_p^{ms}\right)^2 \tag{3.21}$$

The first term is obtained by considering the small deviation θ of a particle in a magnetic field B:

$$\frac{q}{p} = \frac{1}{BR} = \frac{\theta}{BL}, \tag{3.22}$$

where R is the local curvature radius of the track and BL the field integral. The differentiation gives:

$$\delta\frac{1}{p} = \frac{\delta p}{p^2} \propto \delta\theta \tag{3.23}$$

In the absence of multiple scattering, the $\delta\theta$ is constant, and then:

$$\sigma_p^{det} \propto p^2 \tag{3.24}$$

The multiple scattering introduces a p dependence of $\delta\theta$ through Eq. (3.16). For infinite detectors resolution:

$$\delta\theta \propto \frac{1}{p\beta}, \tag{3.25}$$

leading to:

$$\sigma_p^{ms} \propto \frac{p}{\beta} \tag{3.26}$$

Gathering the two terms one finally gets:

$$\frac{\sigma_p}{p} = \sqrt{(\sigma_{1,p}p)^2 + \left(\frac{\sigma_{2,p}}{\beta}\right)^2}, \tag{3.27}$$

with two parameters $\sigma_{1,p}$ and $\sigma_{2,p}$, depending respectively on the detectors resolutions and the radiation length. Similar calculations give the resolutions in polar and azimutal angles θ and ϕ as well as the vertex position z along the beam (or spectrometer) axis:

$$\sigma_\theta = \sqrt{\sigma_{1,\theta}^2 + \left(\frac{\sigma_{2,\theta}}{p\beta}\right)^2} \tag{3.28}$$

$$\sigma_\phi = \sqrt{\sigma_{1,\phi}^2 + \left(\frac{\sigma_{2,\phi}}{p\beta}\right)^2} \tag{3.29}$$

$$\sigma_z = \sqrt{\sigma_{1,z}^2 + \left(\frac{\sigma_{2,z}}{p\beta}\right)^2} \tag{3.30}$$

The relative contribution of the two terms in these expressions largely determines the optimization strategy in the design of a spectrometer. At high momentum (particle physics), the detector term dominates, and high resolution trackers are priviledged. The situation is reversed at low momentum (nuclear physics), where the radiation length of the tracker elements becomes a critical issue. The two terms yield similar contributions at momenta around 0.5-1 GeV/c, *i.e.* roughly in the domain of hadronic physics. The momentum dependent resolutions are shown in Fig. 3.4 with the Clas12 tracking code (Socrat [89]), and closely follow the above expressions.

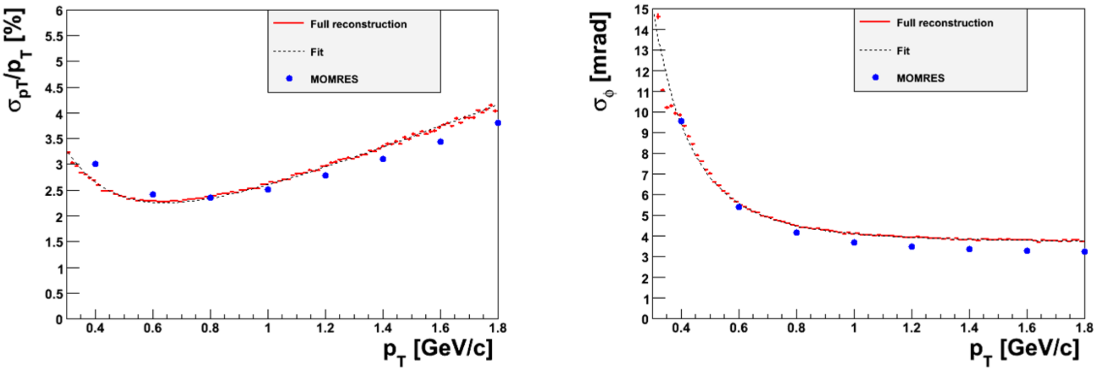

Figure 3.4: *Resolution in momentum (left) and azimutal angle (right) in the Clas12 Central Tracker with a Kalman filter algorithm. Blue points come from a simplified, analytic estimation of the resolution [90].*

3.4.2 Effect of the background

As already stated in the track finding section, the presence of additional hits in a given pattern complicates the reconstruction task. These hits may either be uncorrelated (electronics noise, photons) or correlated if they come from other tracks or low energy track segments. It is frequent that background primarily determines the maximum luminosity that an apparatus can stand through multiple undesired effects:

- high background rates reduce the reconstruction efficiency in different ways: drop of the detector efficiency because of pile-up, increase of the dead time at the trigger level, or wrong hit association eventually leading to the rejection of tracks. Fig. 3.5 illustrates this latter effect for simulated DVCS events in Clas12 as a function of the luminosity.
- it may also degrade the resolutions of the apparatus, in particular if neighbour hits compete for the same track.
- Too many neighbours may also result in *sister tracks*, *i.e.* fake tracks which develop around a good one. If the background density is even higher, a percolation like transition may occur and purely random tracks can be reconstructed.
- Last but not least it slows down the reconstruction algorithm and requires higher CPU.

As far as tracking is concerned, the maximum background rate in a detector depends on its granularity, as pile-up and hit separation are both improved with smaller readout elements. Instead of the integrated background, it is therefore more relevant to consider the *occupancy* of the elements, defined as the time fraction during which this element is busy and cannot detect unambiguously an incoming particle. A significant degradation of tracking performance usually occurs when occupancy yields a few percent level. Apart

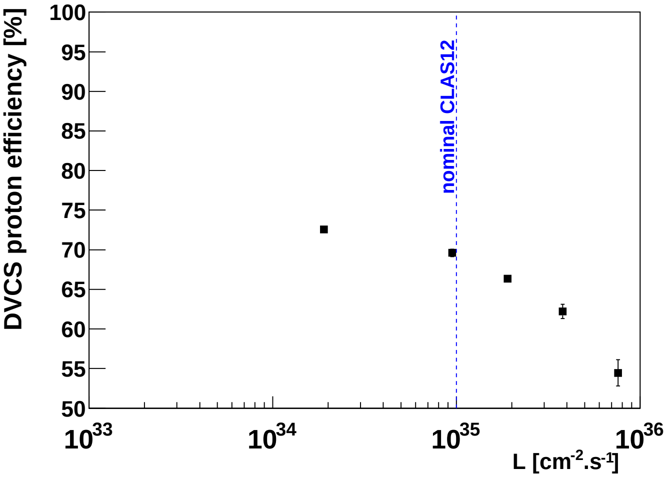

Figure 3.5: *Simulation of the global efficiency of the proton reconstruction from DVCS events as a function of the luminosity, obtained with the Socrat code.*

from the readout granularity, the occupancy can be lower by shortening the time extension of the signal in the detector.
The maximum background in tracking also depends on the time resolution σ_t of a detector. Indeed the signal time, when available, helps the track finding process by removing hits outside a given time window around the trigger. This time window is commonly chosen as a fixed number of σ_t in a given detector. For uncorrelated background, the number of hits to be considered in the tracking is thus directly proportional with the time resolution.

3.4.3 Misalignments

In the whole discussion above it has been assumed that the positions of all detectors, as well as magnetic fields, are perfectly known. In reality alignment defects between the elements of a spectrometer degrade the spatial resolution and track parameter estimations, as illustrated in Fig. 3.6. To fully benefit from the performance of a detector, the effect of the misalignment — and not necessarily the misalignment itself — should be kept within a fraction of its resolution. Such a precision is virtually unreachable mechanically or even with surveyors measurements, and a software alignment procedure should be implemented to achieve this goal. Software alignment makes use of specific data without magnetic field to get reference straight tracks between detectors [2]. A misalignment introduces a distortion of the residual du in a detector (see Section 2.4.5), and generally a correlation arises with other parameters. For example, a rotation $\Delta\theta$ of the detector around its perpendicular axis leads to:

$$du = -v \times \tan \Delta\theta, \tag{3.31}$$

---

[2] Field map positions may be extracted in a second step with respect to the detectors using field-on data.

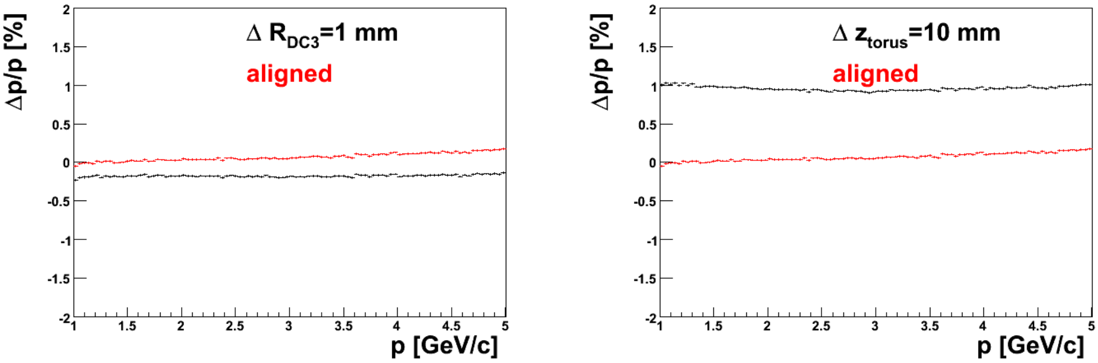

Figure 3.6: *Simulation of the average momentum shift as a function of the electron momentum in the Clas12 Drift Chambers, with a 1 mm shift of the last DC (left) and a 1 cm shift of the torus field map (right).*

where v is the coordinate perpendicular to u in the detector plane. A simple method consists in computing these residuals [3] to access the correlations and update the software detector positions. The method is iterative, as the realignment of one detector may influence the alignment of the others. Though this is applicable for simple setups, it becomes quite a lengthy procedure for complex spectrometers with tens of detectors. Besides, the tracking bias introduced by all the misalignments does not guarantee to converge on the correct geometry. Another formalism has therefore been proposed [91], where the sum of the χ^2 of all the sample tracks is formed and expressed as the track and alignment parameters α_t and α_a:

$$\chi^2 = \sum_{i=1}^{n_{det}} \frac{[du_i(\alpha_t, \alpha_a)]^2}{\sigma_i^2}, \tag{3.32}$$

where σ_i is the resolution of the i^{th} detector and n_{det} the number of detectors to be aligned. The linearization and minimization of this expression as a function of all the αs give the following matrix equation:

$$\left(\begin{array}{c||c|c|c} \sum C_i & \cdots & G_i & \cdots \\ \hline\hline \vdots & \ddots & 0 & 0 \\ \hline G_i^T & 0 & \Gamma_i & 0 \\ \hline \vdots & 0 & 0 & \ddots \end{array}\right) \left(\begin{array}{c} \alpha_a \\ \hline\hline \vdots \\ \hline \alpha_{t,i} \\ \hline \vdots \end{array}\right) = \left(\begin{array}{c} \sum b_i \\ \hline\hline \vdots \\ \hline \beta_i \\ \hline \vdots \end{array}\right), \tag{3.33}$$

where matrices C_i and b_i (resp. Γ_i and β_i) only contain residual derivatives with respect to alignment (resp. track) parameters, and matrices G_i contain both terms. The solution of this equation involves *a priori* the prohibitive inversion of a $(6n_{det}+4n)\times(6n_{det}+4n)$ matrix. However, the extraction of the $\alpha_{t,i}$ in the $4n$ lower lines of Eq. (3.33) can be

---

[3] obviously the current detector should be removed from the tracking

reinjected directly in the first $6n_{det}$ lines, leaving:

$$\left(\sum_i C_i - \sum_i G_i \times \Gamma_i^{-1} \times G_i^T\right) \alpha_a = \sum_i b_i - \sum_i G_i \times \Gamma_i^{-1} \times \beta_i \tag{3.34}$$

The alignment parameters are thus obtained by inverting the n, 4×4 Γ_i matrices and one matrix of size $(6n_{det})\times(6n_{det})$.
The linearization step in this formalism assumes that the initial geometry is not too far from the real one, this is why precise surveyors measurements remain mandatory. More importantly, it should be kept in mind that the χ^2 minimization may result in geometry distortions. Indeed, the χ^2 of straight tracks is unchanged if special global transformations of the spectrometer are applied. This includes global translation or rotation, homothety, helicoidal rotations or more complicated changes depending on the setup. These degrees of freedom should be listed and eliminated by fixing a few geometry parameters, and in particular an absolute distance and some rotation angles.

3.5 Event reconstruction

As stated in Section 3.1 the reconstruction of single tracks does not necessarily suffice for physics analysis. Indeed, several vertices may co-exist in an event, and the task to reconstruct them and distribute the tracks accordingly may be highly non trivial.

3.5.1 Vertexing

As for the tracking itself, the vertexing process may be splitted in a vertex finding and a vertex fitting procedures. If the number of reconstructed tracks is small, it is however possible to try the different combinations and reject tracks giving a high contribution to the total χ^2 of a vertex candidate. The main difficulty therefore appears in the vertex fit, and how to combine the information from the different tracks.
A very performant algorithm consists in adapting the Kalman filter formalism, and to define the state vector $\mathbf{x}$ as the vertex coordinate $\mathbf{v}$ and the momentum $\mathbf{q_i}$ of the n track parameters:

$$\mathbf{x} = (\mathbf{v_1}, \mathbf{v_2}, \mathbf{v_3}, \mathbf{q_1}, \mathbf{q_2}, ..., \mathbf{q_n})^{\mathbf{T}} \tag{3.35}$$

The covariant matrix is a block diagonal built from the covariant matrices $\mathbf{C}$ of $\mathbf{v}$ and $\mathbf{D_i}$ from the $\mathbf{q_i}$. Each track is then seen as a new measurement $\mathbf{m}$ of $\mathbf{x}$. Writing $\mathbf{p_k}$ the state vector of the k^{th} track:

$$\mathbf{m_k} \equiv \mathbf{p_k} = \mathbf{h_k}(\mathbf{v_{k-1}}, \mathbf{q_k}) \approx \mathbf{A_k} \cdot \mathbf{v_{k-1}} + \mathbf{B_k} \cdot \mathbf{q_k} + \mathbf{c_k} \tag{3.36}$$

after linearization. $\mathbf{A_k}$ is derived from the equation of motion and $\mathbf{B_k}$ depends on the coordinate system. With cylindrical geometry:.

$$\begin{pmatrix} 0 & 0 & 0 \\ 0 & 0 & 0 \\ 1 & 0 & 0 \\ 0 & 1 & 0 \\ 0 & 0 & 1 \end{pmatrix} \tag{3.37}$$

The advantage of this formalism is twofold: first its simplified structure compared to the standard Kalman filter provides the vertex position $\mathbf{p}$ without any iterations:

$$\mathbf{x_n} = \mathbf{C_n}\left(\mathbf{C_0}^{\mathbf{-1}} \cdot \mathbf{x_0} + \sum_{\mathbf{k=1}}^{\mathbf{n}} \mathbf{A_k}^{\mathbf{T}}\mathbf{G_k^B}(\mathbf{p_k} - \mathbf{c_k})\right), \tag{3.38}$$

with $\mathbf{G_k^B}$ obtained from matrices $\mathbf{D_k}$ and $\mathbf{B_k}$ [92]. Secondly, it updates the state vectors of the corresponding tracks as well as their covariant matrices. Indeed, the criterion that all tracks should intersect on a single point provides a strong constraint and adds significant information which improves the determination of track parameters.

A potential difficulty may arise in the practical implementation of this algorithm. Indeed the track parameters $\mathbf{q_i}$ may not be all expressed in the same coordinate system. In particular this happens when a spectrometer combines a Central Tracker (with cylindrical geometry) and a Forward one (with measurement at fixed z along the beam axis). In such a situation, the covariant matrix of the state vector should be carefully transformed in the same coordinates. As an example, let's consider the spatial transformation of the state vector $(x, y, u_x, u_y, q/p)$ in cylindrical coordinates, *i.e.* from a constant z to a constant R. Variations of x and y are easily related to variations of the azimutal angle Φ:

$$\begin{aligned} \delta x &= -R\sin\Phi \cdot \delta\Phi \\ \delta y &= R\cos\Phi \cdot \delta\Phi \end{aligned} \tag{3.39}$$

The relations between variations in x, y and z can be obtained from the helix parametrization, see Eq. (3.6):

$$\delta t = \frac{m}{p_z^0}\delta z \tag{3.40}$$

from which we get:

$$\begin{aligned} \delta x &= \cos\phi \cdot \tan\theta\delta z \\ \delta y &= \sin\phi \cdot \tan\theta\delta z, \end{aligned} \tag{3.41}$$

where θ is the track polar angle and ϕ the local azimutal angle in the $x - y$ plane. Multiplying these quantities give the desired relations of the covariant matrix components in both cordinate systems, *e.g.*:

$$cov(x, y) = -R^2\sin\Phi\cdot\cos\Phi\sigma_\Phi^2 + \tan^2\theta\cdot\sin\phi\cdot\cos\phi\sigma_z^2 + R\tan\theta\cdot\cos\Phi + \phi cov(\Phi, z) \tag{3.42}$$

3.5.2 Physics analysis

Once the full event has been reconstructed, the related physical quantities are accessible and reactions of interest can be selected. The reconstruction can either be run on simulated or real data. In the first case, an *ad hoc* generator first provides events at the right kinematics and the tracks are propagated in a model (usually based on the Geant4 [93] package) of the apparatus giving hits to be reconstructed. Fig. 3.7 gives a few examples of such reconstructed data with various generators using the Socrat code of Clas12. Simulated quantities like missing mass resolution or acceptance can then be compared with the initial physics requirements. If these requirements are not met, the apparatus is revised, *e.g.* with more precise detectors, improved electronics for better time resolutions and thus less background hits, better shielding, smaller dead zones for higher efficiency, etc.
In case of real data, quality checks can be performed based on the stability of a set of observables - missing mass, cross section of a well known process. The comparison between simulation and data also provide hints for misalignments or inaccurate field maps.

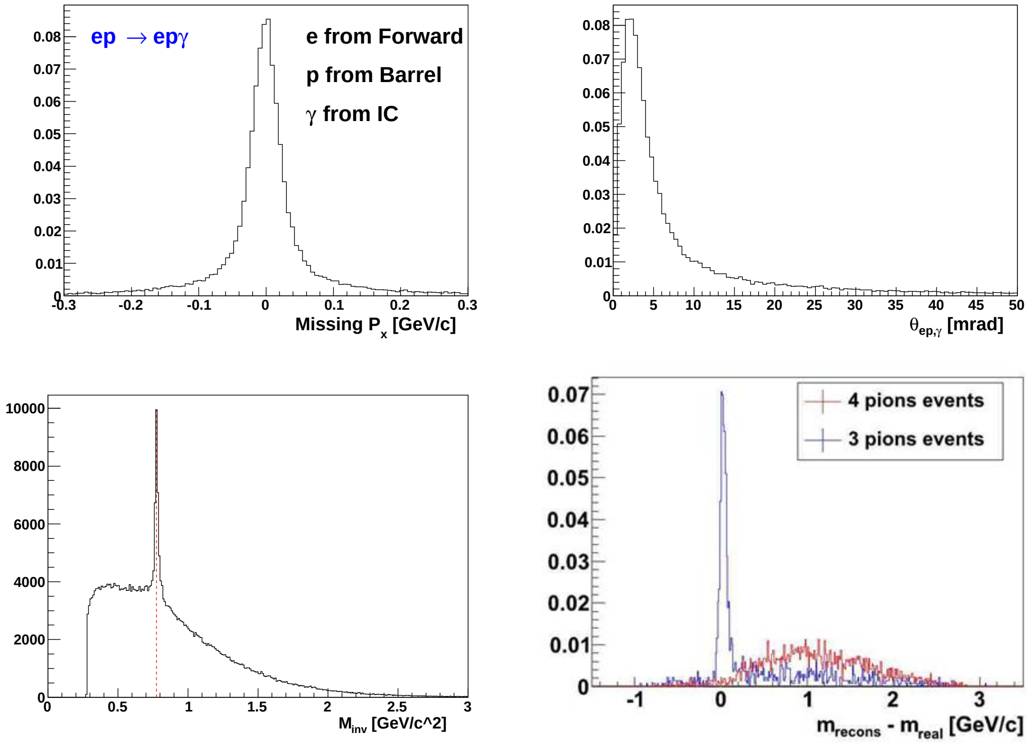

Figure 3.7: *Examples of event reconstruction with a full simulation code. (Top): distributions of the missing x momentum (left) and difference between reconstructed and measured photon angle (right) for DVCS events (dvcsgen generator). (Bottom left): invariant mass distribution of $\pi\pi$ events showing the ρ resonance (Pythia generator [94]). The red line indicates the PDG ρ mass value used in Pythia. (Bottom right): missing mass distribution of 3-pion events coming from the electroproduction of an exotic meson [65]. The 4-pion event contamination is also shown.*

Chapter 4

Micromegas and discharges

We have already mentioned that the maximal gain accessible with Micromegas is limited by the development of discharges in the amplification gap. Theoretically a discharge occurs when the applied electric field exceeds the breakdown voltage of the associated capacitor. In practice however, such a value cannot be attained: defects or dust indeed locally lower the breakdown voltage, not to mention natural ionizations which can initiate an avalanche in the vicinity of which the electric field is enhanced. After a general and historic introduction to the discharge, we will review some consequences and early measurements of the discharge rate in Micromegas. We will see that discharges can be simply understood with a Geant4-based model which was confronted with more systematic measurements. This model quantitatively explains why GEM detectors are less subject to discharges. We will finish the chapter by a review on technologies developed to reduce the discharge rate or at least to quench their amplitude.

4.1 Introduction to discharges and breakdown

4.1.1 The Paschen law

The first systematic measurements of the breakdown voltage of a capacitor were carried out in the second half of the XIXth century. They culminated with the work of F. Paschen who established experimentally that the breakdown voltage is a non linear function of pd [95], the product of the pressure by the distance between the plates (**Paschen law**):

$$V_{br} = \frac{a \times pd}{b + \ln pd}, \tag{4.1}$$

where a and b are gas dependent parameters. It is interesting to note that this function exhibits a minimum in pd below which the breakdown voltage increases strongly. This increase later received the following microscopic interpretation: if the mean free path of electrons starts to be non negligible compared to the plate distance, they will have fewer

possibilities to ionize the gas, even if they acquire enough energy between two collisions. A breakdown will therefore require higher voltages. In particular, this effect explains why a Micromegas detector can stand electric fields up to 80 kV/cm in atmospheric air, whereas the air dielectric strength is only 36 kV/cm.
The Paschen law empirically provided the first quantitative criterion for voltage breakdown, but it did not give an insight nor a theoretical frame on the mechanisms as work. A decisive contribution to the understanding of breakdown came in the early 1900s with the microscopic description of the avalanche by Townsend.

4.1.2 The second Townsend coefficient and generation mechanism

The Townsend measurements of the current in an irradiated chamber as a function of the reduced field E/p indicated an exponential growth of the charge avalanche, formalized by the first Towsend coefficient α (see Chapter 1). Additional measurements at higher E/p showed a further increase of the current that Townsend interpreted as a second ionization mechanism. At that time, it was believed that the ionization process of the avalanche was ensured by negative ions, which were known to have higher mobilities than positive ones. Therefore Townsend naturally suggested that larger E/p allowed a second ionization from positive ions in their way to the cathode [30]. Associating this process with a second coefficient β, the current in the chamber could be expressed as:

$$i = i_0 \frac{(\alpha - \beta)e^{(\alpha-\beta)x}}{\alpha - \beta e^{(\alpha-\beta)x}} \tag{4.2}$$

This formula provided a correct agreement with the existing data, and the positive ion process was adopted, even after it was realized that negative ions were in fact free electrons. The divergence of the current leads to a quantitative criterion:

$$\alpha = \beta e^{(\alpha-\beta)x} \tag{4.3}$$

However, Townsend identified a third mechanism, in which a positive ion striking the cathode has a probability γ to release a secondary charge that will initiate new avalanches. This process was thought to be negligible compared to the second mechanism until experiments in the 1930s unambiguously showed that gas ionization cannot occur from positive ions at these values of E/p. The γ parameter is nowadays known as the **second Townsend coefficient**, and expresses the probability to emit a secondary electron from the cathode per positive ion in the avalanche. It should be emphasized that this emission does not necessarily result from the interaction of the ion itself with the cathode. Indeed, photons created during the avalanche contribute significantly to the development of secondary avalanches, as illustrated in Fig. 4.1. Starting from n_0 primary electrons, the first avalanches create $n_0(e^{\alpha d} - 1)$ ions, and thus $\gamma n_0(e^{\alpha d} - 1)$ secondary avalanches. Repeating the process the current writes:

$$i = i_0 e^{\alpha d} + i_0(e^{\alpha d} - 1)\gamma e^{\alpha d} \times \sum_{n=0}^{\infty} (\gamma(e^{\alpha d} - 1))^n \tag{4.4}$$

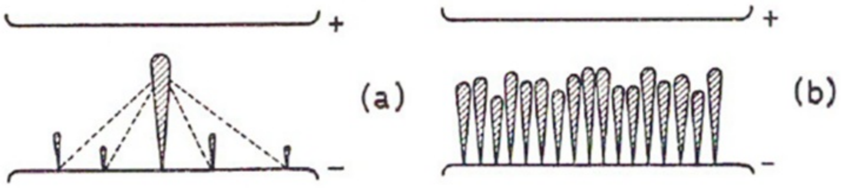

Figure 4.1: *Illustration of secondary electron production from [97]: a first avalanche emits photons that interact with the cathode and initiate secondary amplification (a). This process can be repeated several times, leading to a potentially large number of avalanches (b).*

If a mother avalanche yields less electrons at the next generation, the sum is convergent:

$$i = i_0 \frac{e^{\alpha d}}{1 - \gamma(e^{\alpha d} - 1)} \tag{4.5}$$

This equation is similar to Eq. (4.2), and provides the same agreement with the observations. If, however, the total number of electrons is increased at each generation, the current is divergent, and leads to a voltage breakdown. The classic **Townsend criterion** for breakdown is then:

$$\gamma(e^{\alpha d} - 1) = 1 \tag{4.6}$$

This criterion can be easily extended to the case where the electron attachment coefficient is not negligible. Using the Townsend parameterization of α/p (see Eq. (1.27) of Chapter 1), one can also obtain the breakdown voltage:

$$V_{br} = E \times d = \frac{Bpd}{\ln \frac{A}{\ln 1 + \frac{1}{\gamma}} + \ln pd}, \tag{4.7}$$

which proves that the Paschen law is a consequence of the Townsend criterion.
The Townsend mechanism provides a simple explanation of breakdown by the creation of a cascade of secondary electrons leading to the divergence of the current. Early time measurements confirmed that this type of breakdown is slow, typically 10 μs for a 1 cm gap, and generally occurred after a few hundreds of avalanches. However, the Townsend mechanism does not provide any details on *how* the current divergence leads to the breakdown

4.1.3 The streamer mechanism and the Raether limit

In the 1920s, Rogowski studied the time development of the breakdown by applying short pulses of 30 kV in a 1 cm gap [99]. He found that the voltage drops within a few tens of nanoseconds, which cannot be explained by the Townsend theory. Besides, observations with cloud chambers suggested that the sparks were localized, proving that the breakdown could not come from the accumulation of secondary avalanches. It was soon understood that in this new mechanism, the breakdown is achieved with a single avalanche by the formation of **streamers** developing very rapidly [1] in the directions of both electrodes. Detailed studies were performed by Raether, and the streamer development was explained by the strong electric field near the charge clouds resulting in further ionization of the gas in the edges of the avalanche. This effect is illustrated in Fig. 4.2.

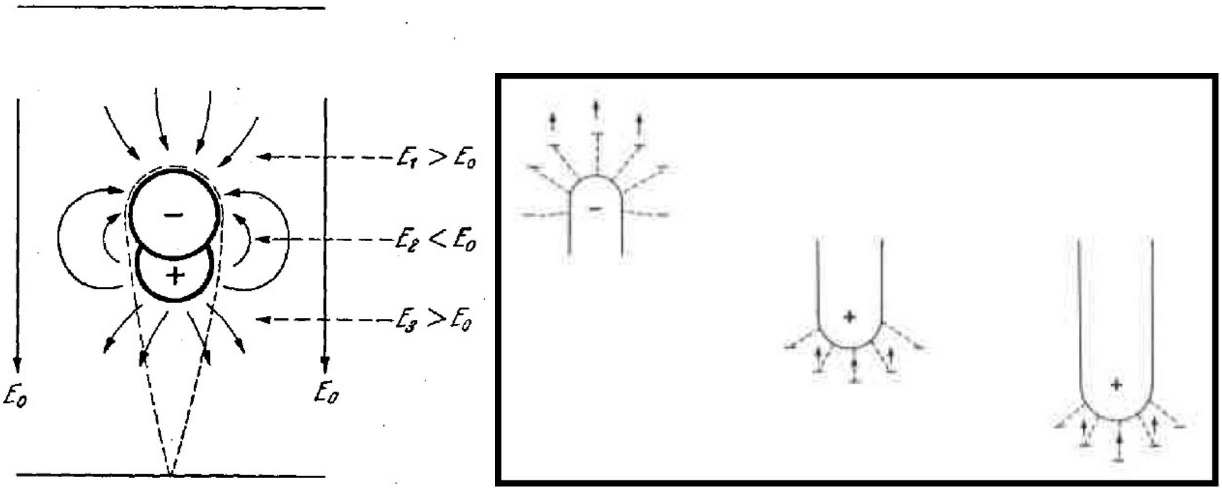

Figure 4.2: *(Left): field configuration in the vicinity of the avalanche; (right): development of the streamer at the two edges of the avalanche through gas ionization (plots from [97]).*

Empirically, streamers were found to occur when the amplification reaches $e^{\alpha d} \sim 10^7 - 10^8$, an estimate nowadays known as the **Raether limit**. Another quantitative criterion was established by Meek in 1940, who suggested that *"a streamer will develop when the radial field about the positive space charge in an electron avalanche attains a value of the order of the external applied field"* [98]. On the contrary to the Raether limit, this criterion is relatively intuitive, and approximate calculations show that both estimates are in good agreement.

It should be emphasized that these two estimates assume that the breakdown occurs from a single avalanche, and the criteria should then be understood as a charge density limit. This is explicit in the Meek criterion, but not in the Raether limit which is expressed in a total number of electrons.

4.2 Discharges in Micromegas

4.2.1 Manifestation and consequences

As any other capacitor or MPGD, the Micromegas is subject to discharges. Indeed, the need to amplify the primary signal of an incident particle usually requires to operate at gains of several thousands, corresponding to electric fields above 10 kV/cm. The first effects of a

---

[1] *i.e.* with velocities larger than electron or ion ones

discharge are the appearance of an abnormal current from the micro-mesh to the strips and a voltage breakdown, accompanied by a visible spark. During the breakdown, the potential difference drops very rapidly (in a few tens of ns) and quenches the discharge. The HV power supply then charges up the micro-mesh back to its nominal value, in a characteristic time τ ranging from 1 to 100 ms, as illustrated in Fig. 4.3. During most of this time, the Micromegas is unable to ensure a full detection efficiency of the incoming particles. Indeed, the gain becomes too small to stay on the efficiency plateau, and the voltage variations of the micro-mesh further induces noise on all the readout elements. Writing F the discharge rate of a detector, a reasonable requirement on the dead-time $F \times \tau$ is then $F \times \tau \leq 5\%$. Solutions to decrease this fraction, and in particular τ, will be presented in Section 4.5.

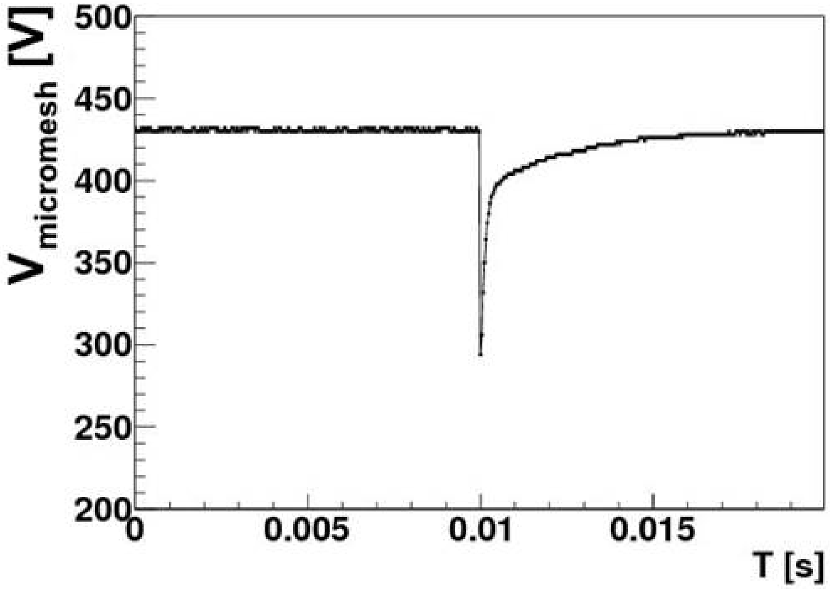

Figure 4.3: *Typical high voltage variations of the micro-mesh during a discharge (induced by a α source).*

Though discharges are also known to be harmful for several types of MPGDs, they rarely induce damage or ageing effects to the Micromegas. The best proof is provided by the twelve Micromegas of the Compass experiment which have been running smoothly for more than a decade. The various elements of the detector, and in particular stainless steel woven micro-meshes, are robust enough to resist to short μA currents. If the discharges involve much higher currents, however, irrepairable damage can be observed, as illustrated in Fig. 4.4. But this is easily avoided in practice by limiting the maximal current of the power supply to reasonable values.

4.2.2 Past measurements

The issue of discharges in Micromegas was investigated as soon as 1998 for its application to the Compass experiment. The goal of this R&D was to minimize the discharge rate

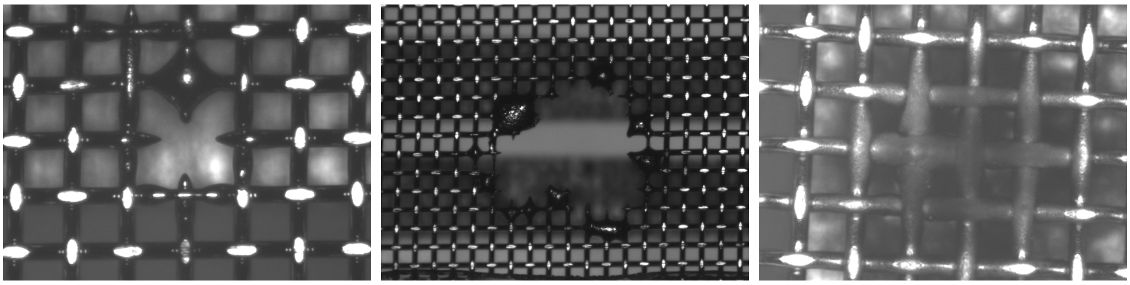

Figure 4.4: *(Left and middle): damages observed on the micro-mesh with discharges involving mA currents. (Right): ageing of the micro-mesh after intense and localized discharges using a α source.*

in order to operate at a gain that can ensure full detection efficiency for MIPs. After preliminary measurements with a α source, a beam test was organized in the T9 line of the Cern/PS. This line provides hadron beams from 3 to 15 GeV/c with fluxes up to $2{\times}10^6$ Hz, *i.e.* well adapted to precise discharge rate measurements. Five important observations were made [46]:

- the discharge rate is proportional to the beam intensity, which means one can define a probability of discharge P per incident particle;
- the discharge probability exhibits a power law dependence with the gain of the detector, *i.e.* $P = k \times G^n$, with n ranging from 1.6 to 2.3 (see Fig. 4.5).
- for a given gain, the discharge probability strongly depends on the mean atomic number of the gas $< Z >$. In particular, Neon-based mixtures reduce the discharge rate by almost an order of magnitude compared to Argon;
- the discharge probability is independent on the hadron energy, from 3 to 15 GeV;
- the discharge rate is much higher with hadrons than with muons. This last observation was derived from a comparison with a beam test in the M2 line at the Cern/SPS.

The observed gas dependence cannot be explained by the difference of primary ionizations between Argon and Neon. Even if the efficiency plateau is indeed reached at a lower gain with Argon gas, the discharge probability at the beginning of the plateau is still significantly lower with Neon. This gas feature allows the Compass Micromegas to run at full efficiency with discharge rates of the order of 1 /min in muon beams.
Most of these observations were not quantitatively understood at that time. However, the discharges were not attributed directly to the incoming hadrons, as these particles could not provide enough primary electrons: *"Even if one includes the tail of the distribution of energy loss (Landau distribution), it is unlikely that the energy deposit exceeds 10 keV for such particles. This is not the case for secondary particles or nuclear fragments which can deposit much larger amounts of energy"* [46]. This actually remains true even after the convolution of the Landau distribution for energy deposit with the Polya distribution for the gain fluctuation. Such a convolution cannot give rise to the power law dependence of

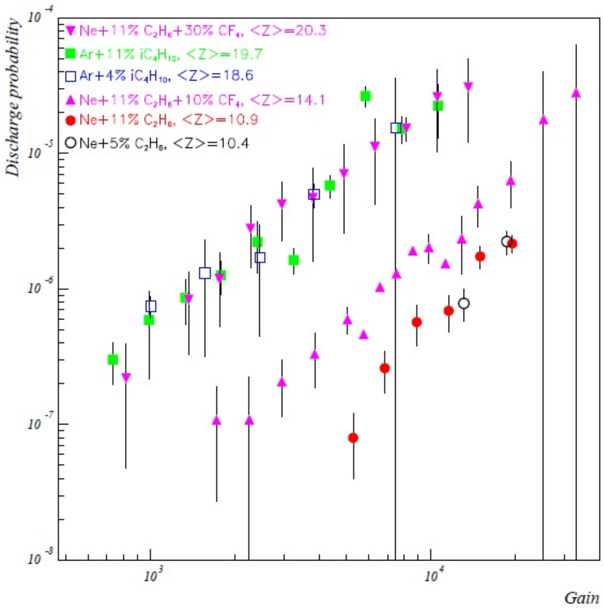

Figure 4.5: *Discharge probability measured on the T9 hadron beam line of the Cern/PS with different gas mixtures as a function of the gain (plot from [46]).*

the discharge probability with the gain. For several years, a quantitative understanding of these observations was thus lacking.

4.3 Simulation of discharges in hadron beams

4.3.1 A Geant4-based model

The development of reliable simulation tools on the interactions between particles and matter offered the opportunity to better understand the origin of discharges in Micromegas. Among these tools, the Geant4 [93] package appeared as one of the most suitable to precisely describe the nuclear interactions between a high energy hadron and the detector materials. The experimental setup mentioned in the previous section was first modeled and studied using the 4-09-02 version and the `QGSC_BERT` physics list [2]. Systematic checks were performed to investigate the effect of the production threshold or the integration volume for the deposited energy. For the latter, boxes of 300 μm×300 μm× the drift gap were first applied to integrate transverse diffusion effects that were primarily not modeled.

---

[2] well adapted to the 3-15 GeV energy range [100]

4.3.2 Large energy deposits and discharges

The simulation of 15 GeV pions impinging on the detector reveals that 98.73% of them don't produce any secondaries and release of the order of 1 keV in the Argon-Isobutane gas. For 1.26% of events, the pion creates a secondary electron in the gas volume, but this does not significantly change the deposited energy. In the remaining 0.01%, however, interactions between the pion and the material of the detector produce several secondary, highly ionizing particles (HIPs) as shown in Fig. 4.6. The production probabilities of all these particles roughly vary from 10^{-8} to 10^{-4}, which corresponds to the typical orders of magnitude for discharge probabilities.

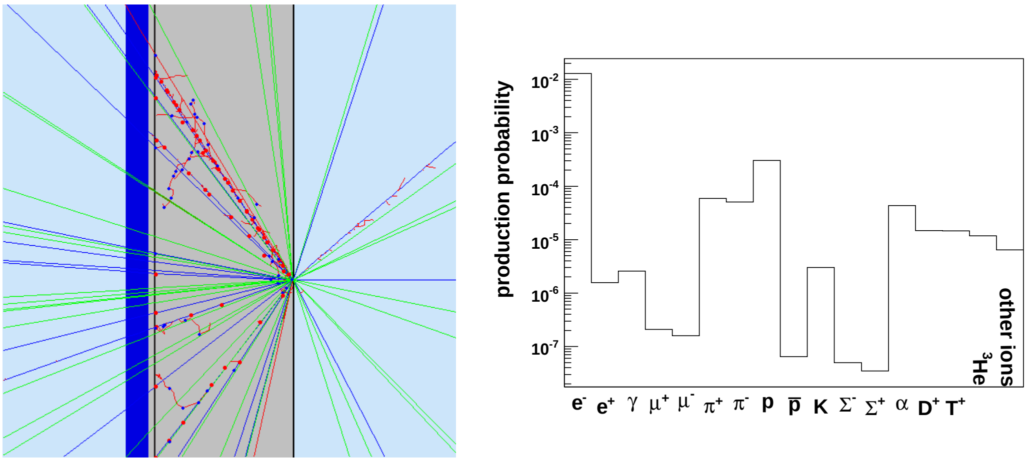

Figure 4.6: *(Left): example of an interaction between an incident pion and the drift electrode. Besides secondary electrons and photons, a low energy proton is emitted. Large energy deposits (represented by dots) are visible all along its trajectory in the conversion gap. (Right): production probability for all secondary particles [101].*

The distribution of the highest energy deposit per event in the detector is shown in Fig. 4.7 and exhibits as expected a very long tail coming from HIPs. Energies of the order of 1 MeV can be locally deposited in the detector, with a probability close to 10^{-8}. Around 42% of the particles depositing at least 0.2 MeV are produced in the drift electrode, 22% in the gas itself, 10% in the micro-mesh, and 23% in the strips. A 1 MeV energy deposit corresponds to around 40000 primary electrons in the Argon-Isobutane mixture, *i.e.* 4×10^7 electrons after the amplification by a modest gain of 1000. This value exceeds the Raether limit which means that such deposits are likely to induce a discharge. Assuming the number of electrons created in the conversion gap is directly proportional to the deposited energy, we can then derive the discharge probability dependence with the gain by using the Raether limit. In this case, the discharge criterion can be simply written as:

$$\frac{E_{dep}}{w_i} \times G > N_R \approx 2 \times 10^7, \tag{4.8}$$

where w_i is the mean energy to create an electron-ion pair in the gas (see Chapter 1). Thus, the integration of the tail of the deposited energy directly provides the discharge

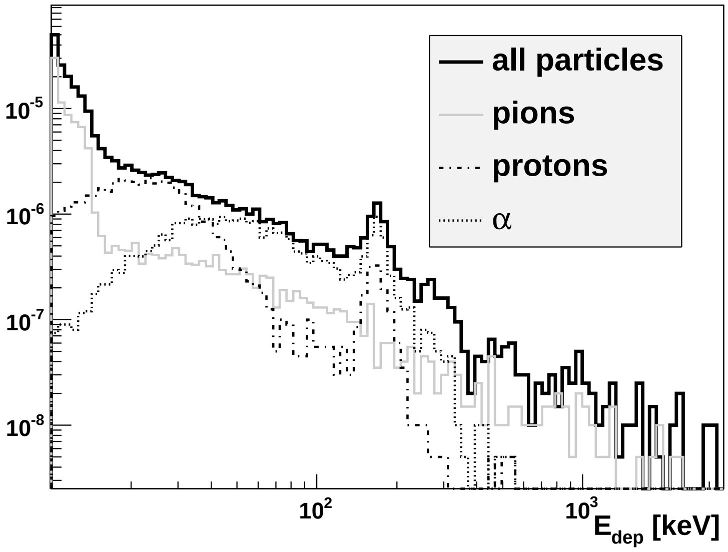

Figure 4.7: *Tail of the local deposited energy in a Micromegas detector using a 15 GeV* π^+ *beam, normalized to the total flux of pions.*

probability P at a given gain G:

$$P(G) = \int_{E_{dep}=N_R \times w_i/G}^{\infty} f(X)dX, \tag{4.9}$$

where f is the deposited energy distribution. The result of this integration is displayed in Fig. 4.8, where a power law dependence is clearly observed. Furthermore, the use of the standard value for the Raether limit provides a quantitative agreement with the experimental measurements. Other simulations showed that the discharge probability is largely independent from 3 to 15 GeV, as observed in the data.

4.3.3 Effect of the gas and detector materials

The simulation was also used to investigate the gas dependence of the discharge probability. It turns out that Argon and Neon have similar dielectric strengths, meaning that the same Raether limit can be safely assumed for both gases. Under this assumption, the simulation yielded a significantly lower discharge rate for Neon, as a consequence of a higher w_i and spatially wider energy deposits. However, the simulated reduction doesn't entirely explain the measurements, suggesting either a different Raether limit or an effect from the transverse diffusion.

The influence of the detector materials is illustrated in Fig. 4.9, showing the fraction of events with large energy deposits and originating from the different elements of the detector. This plot suggests that some optimization can be done in the choice of the materials, but with limited improvement. Another interesting result concerns the contribution of the micro-mesh to these energy deposits. First measurements were performed with 4-micron

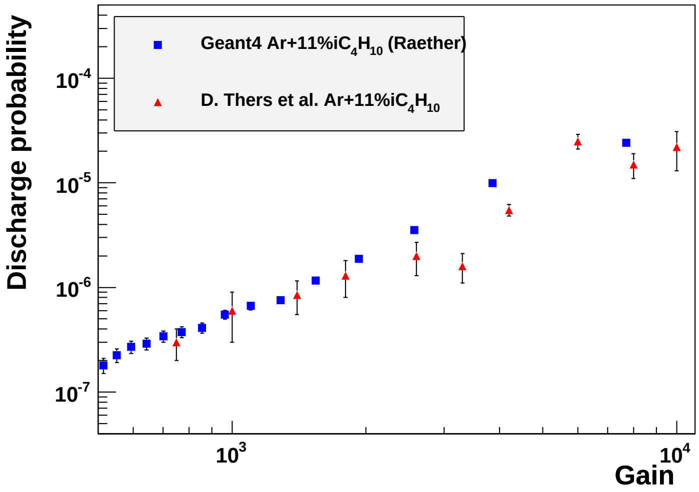

Figure 4.8: *Comparison between the simulated discharge probability and the measurements from [46] with 15 GeV pion beam.*

thick electroformed grid, whereas most of the Micromegas nowadays are issued from the bulk technology with 30-micron, stainless steel woven micro-mesh. Being thicker, the latter micro-mesh indeed induces more HIPs in the detector, but this is partially compensated by a screening of HIPs originating from the strips. As a result, the discharge probability expected with a woven micro-mesh is not significantly higher than with an electroformed grid. This prediction of the simulation was later confirmed by new measurements.

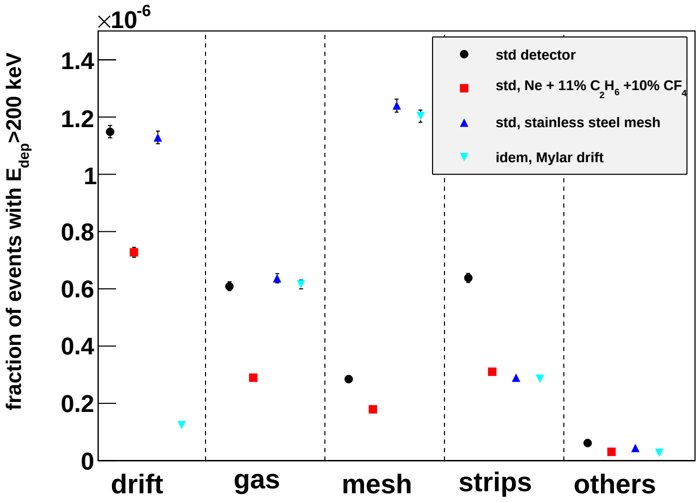

Figure 4.9: *Contribution of the different parts of the detector to the production of energy deposits larger than 200 keV for various geometries.*

4.4 Recent discharge rate measurements and simulation

Though the simulation presented in the previous section gives a correct estimate of the discharge probability for Micromegas in a 15 GeV beam, further studies and comparisons were required to extend the validity of this model. The main goal of this extension was to provide a tool that could reliably predict the discharge rate for a given setup. In particular, the effect of the following parameters were of particular importance:

- The beam energy and type: the cross sections for the production of nuclear fragments are indeed energy dependent. Besides, the Geant4 physics lists are not supposed to be equally valid at different energies.
- The presence of an external magnetic field: such a field modifies the drift of electrons and can therefore affect the local charge density in the gas. The case of a parallel and perpendicular magnetic field (with respect to the electric field) should be distinguished.
- The presence of a GEM [102] foil: GEM detectors are indeed known to induce less discharges at a given gain than a Micromegas. Besides, the use of a GEM foil in combination with a Micromegas significantly reduces the discharge rate [103]. A quantitative understanding of the underlying mechanism was still missing.

The study of all these parameters required new measurements to be compared with the simulation. From 2009 to 2010, three different beam tests were thus organized both at Cern and at the Jefferson Laboratory to cover all the configurations.

4.4.1 Effect of the beam energy and type

The remarkable variety of beam lines available at Cern makes it a unique place to test the dependence of the spark probability on the beam energy. High intensity hadron beams can be used from 150 GeV/c (SPS) down to several hundreds of MeV/c (PS). A first campaign was organized in October 2009 on the SPS/H4 beam line, with the aim of measuring the spark probability for different types of Micromegas [104]. Six detectors were placed simultaneously on a support structure to compare their behaviour in the same conditions. The whole structure was located inside the Goliath dipole to investigate the role of a transverse magnetic field.
The second beam test took place on the PS/T11 line in August 2010 [105], with twelve detectors tested simultaneously. The T11 beam line offers the possibility to tune the beam energy from 3 GeV/c down to approximately 200 MeV/c, by changing currents in the upstream magnets. The charge of the particles can also be chosen, by reversing the sign of these currents. Negatively charged beams essentially consist of π^-, with negligible contribution of anti-protons. In the case of positively charged particles however, the fraction of protons in the π^+ beams reaches almost 1%.
The main characteristics of these two beam tests are summarized in Table 4.1.

	Cern/SPS	Cern/PS
Beam line	H4	T11
Beam momentum	150 GeV/c	0.2-3 GeV/c
Beam particles	π	π^- or π^+ with protons
Spill	10 s every 50 s	1 or 2×0.4 s every 50 s
Max beam intensity	10^6 / spill	5×10^5 / spill
Number of detectors tested	10	20
Active area of detectors	$10\times10\,\mathrm{cm}^2$	$10\times5\,\mathrm{cm}^2$
Gas mixture	Ar+5%iC_4H_{10}	Ar+5%iC_4H_{10}
Number of spills recorded	7000	27000

Table 4.1: *Cern beam test specificities.*

High energy beams - SPS

The measured spark probability for five detectors is shown on Fig. 4.10, with a usual power law dependence as a function of the gain. In particular, no significant difference has been observed between thick and thin micro-mesh, *i.e.* between bulk and non bulk detectors. These results have been compared with a full Geant4 simulation of the experimental setup, using the same physics list and the same method as described above [101]. The only free parameter, *i.e.* the value of the Raether limit N_R, has been adjusted to the data. A reasonable agreement is obtained with $N_R = 2.5 \times 10^7$, which is close to the value fitted from 15 GeV data, 2×10^7.

Low energy beams - PS

At low energy, scans in both gain and beam energy have been performed. The latter is illustrated in Fig. 4.11 for three detectors located at the upstream, middle and downstream part of the setup. Above 1 GeV/c, results for negatively and positively charged beams are well compatible, and almost energy independent. Below 1 GeV/c however, a significant decrease is observed in the π^- case, while three pronounced peaks appear at specific momenta of the π^+ and protons, namely 300, 500, and 650 MeV/c. The latter one is wider and almost not visible for downstream detectors.

These data have been compared with a full Geant4 simulation of the setup, whose results are shown in Fig. 4.12 (left). Apart from the three peaks, the overall dependence of the spark probability with beam energy is reproduced, and a fair agreement is quantitatively obtained with a Raether limit of 4×10^7. However, the simulation indicates that the spark probability does not depend on the charge of the pions. A similar simulation has been run with protons, and a narrow peak showed up around 300 MeV/c, as illustrated on Fig. 4.12 (left). This peak originates from the stopping of protons in the detector volume, as in Fig. 4.12 (right), which leads to the release of a very large number of primary electrons. This effect not only explains the absolute position of the first peak in the data, but also its shift as a function of the detector position. A higher energy is indeed needed for protons to reach and stop in the most downstream detectors. Last but not least, the correct am-

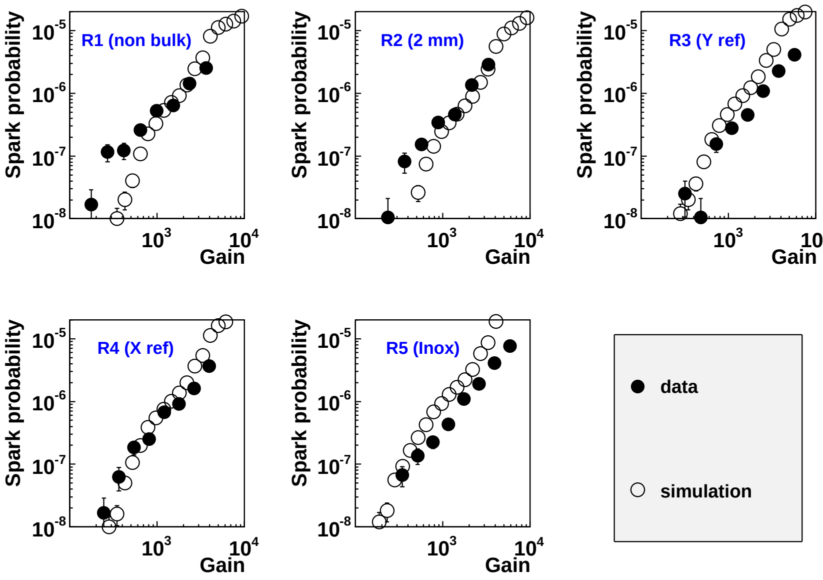

Figure 4.10: *Discharge probability in a 150 GeV pion beam as a function of the gain for five Micromegas detectors. Measurements (full circles) are compared with the Geant4 simulation (open circles) [104]. R3 and R4 are reference bulk detectors with 5 mm drift gap, R1 is a non bulk detector, R2 has a reduced 2 mm drift gap and R5 is equipped with a micro-mesh as the drift electrode.*

plitude of the peak could be obtained by assuming a 0.5% proton contamination in the π^+ beam, which is compatible with observations from the scintillators (<1%). The simulation has also been run with deuterons and tritons, and similar peaks indeed arised at 500 and 650 MeV/c.

These two tests at high and low energies combined with early measurements at 15 GeV/c confirmed that the same Geant4 based simulation can give a correct estimate of the spark probability over three orders of magnitude in beam momentum. The only free parameter is the Raether limit, which is found to be a few 10^7 for all the measurements, and seems therefore intrinsic to the detectors. Besides, this value is close to the one generally assumed for the development of a spark, giving strong credit to the model.

4.4.2 Effect of an external magnetic field

All the considerations above assume that a spark is initiated by a constant number of electrons in the vicinity of the amplification gap. One should keep in mind, however, that the Raether limit was initially estimated from *single* avalanche processes. But in our case, a spark essentially originates from the stopping of a highly ionizing particle which leads to many, localized avalanches. It is thus relatively intuitive that the charge density is a more relevant parameter than the total number of electrons. A simple way to emphasize the role of the charge density is to apply an external magnetic field which will modify the electron drift inside the detector. The possible effect on the spark probability is likely to

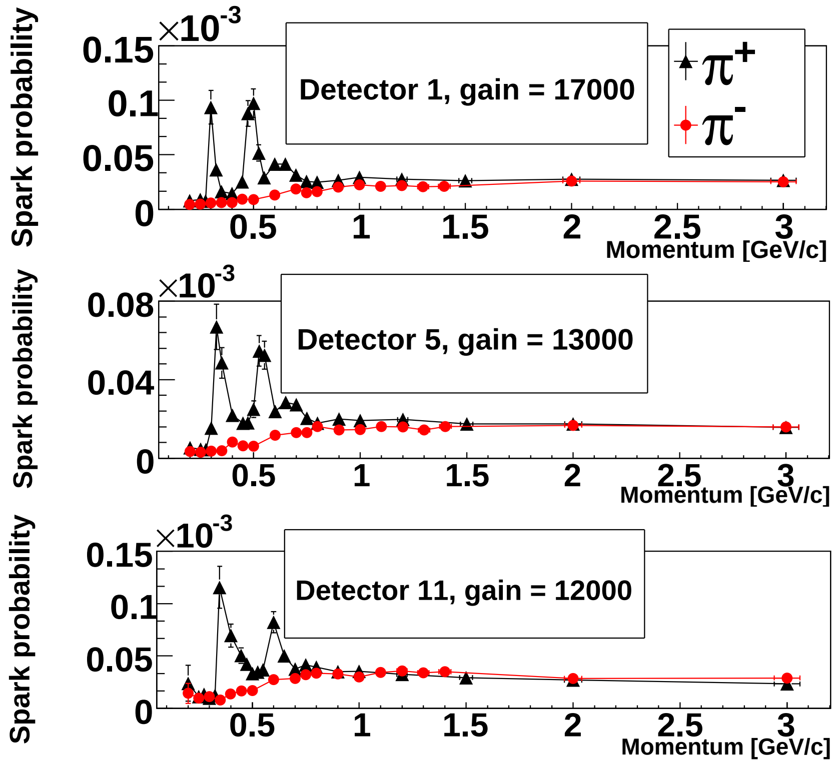

Figure 4.11: *Discharge probability for three Micromegas detectors as a function of the beam energy in* π^- *and* π^+ + *proton beams. The micro-mesh high voltage of all detectors was fixed at 430 V [105].*

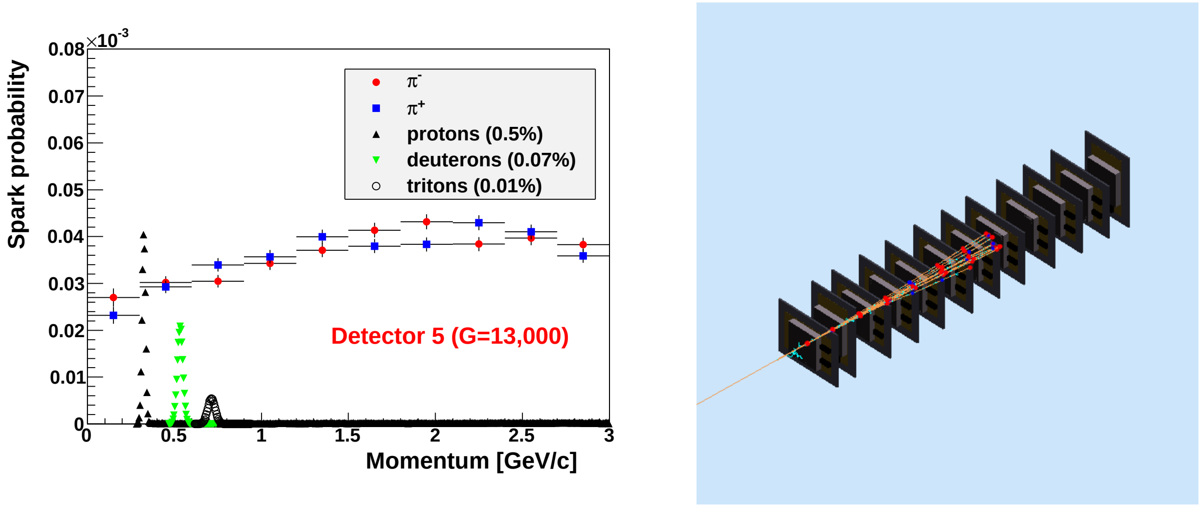

Figure 4.12: *(Left): Simulated spark probability as a function of incident hadron momentum for pions, protons, deuterons and tritons, for the middle detector [105]. (Right): 300 MeV/c proton beam on the experimental PS setup, illustrating the stopping of protons.*

be different according to the direction of the magnetic field, *i.e.* perpendicular or parallel to the internal electric field.

Case of a transverse magnetic field

In the perpendicular configuration primary electrons drift along an axis with a Lorentz angle θ with respect to the electric field $\vec{E}$ given by Eq. (1.21). Even in the case of a localized energy deposit, this angle will geometrically decrease the charge density. For a 20° Lorentz angle, this reduction is of the order of 15%.
The perpendicular configuration was investigated during the Cern/SPS beam test, where the detectors were located inside the Goliath magnet. This dipole delivers a tunable field up to 1.5 T. The spark probability measured as a function of B is shown in Fig. 4.13. No dependence has been observed with a Lorentz angle of 20°, though hints of a significant decrease have been seen in later measurements with a larger Lorentz angle.

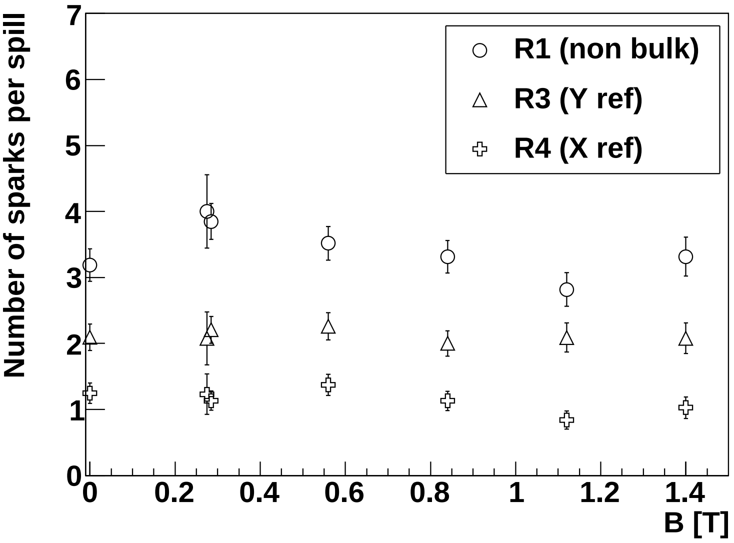

Figure 4.13: *Number of sparks per spill for three detectors as a function of the transverse magnetic field. The Lorentz angle in the drift gap was estimated to be 20° at 1.5 T [104].*

Case of a longitudinal magnetic field

In the parallel case the electrons are focused around the magnetic field lines, resulting in a reduced transverse diffusion and a higher charge density. The study of this configuration took place in the Hall B of the Jefferson Laboratory in July 2010 [106]. A small Micromegas was inserted in the 5 T Frost solenoid, downstream of a CH_2 target. The incident photon beam was obtained from the interaction of a primary 5.57 GeV electron beam with a thin Pt radiator. The main characteristics of the setup are summarized in Table 4.2.

In a first set of measurements, the spark probability was recorded as a function of the gain, and agreed well with the Geant4 simulation using a Raether limit of 2.5×10^7. In a second step, the gain of the detector was fixed and the magnetic field varied between 0 and 5 T. An increase by a factor of 10 was obtained, as illustrated in Fig. 4.14. It was checked

Location	JLab/Hall B
Beam momentum	0 to 5.57 GeV (Bremsstrahlung)
Beam particles	photons
Target	19.3 mm thick CH_2
Beam structure	continuous beam
Max beam intensity	2.5×10^9 photons/s
Number of detectors tested	2
Detectors dimension	11 cm diameter
Gas mixture	Ar+10%iC_4H_{10}
Number of sparks recorded	24000

Table 4.2: *JLab beam test specificities.*

with the simulation that the particle flux (especially hadrons) did not change significantly from 0 to 5 T, proving that this increase can only be attributed to an enhancement of the charge density in the amplification gap. This effect was confirmed in a 1.5 T field using a ^{241}Am source, where the detector gain was shown to be independent on the magnetic field. These measurements prove unambiguously that the relevant parameter in spark development is indeed the charge density. The initial Geant4 simulation was therefore upgraded to take into account the transverse diffusion in the gas volume of the detector. This upgrade is described in the next section and illustrated in the case of a hybrid Micromegas-GEM detector.

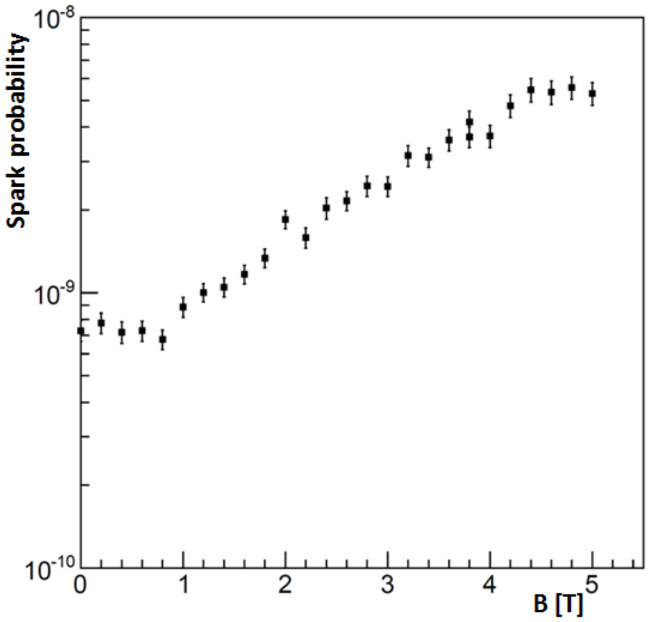

Figure 4.14: *Spark probability per incident photon on the target as a function of a longitudinal magnetic field. The detector gain was approximately 1000 [106].*

4.4.3 Effect of an additional GEM foil

It has been known for a long time that the addition of a GEM foil to a Micromegas detector significantly reduces the spark probability [103]. Precise measurements performed at Cern/SPS, PS, and JLab confirmed the reduction by a factor of 10 to 100, independently of the beam energy and experimental setup. To better understand the role played by the GEM in this reduction, a systematic study was performed during the Cern/PS beam test, where two Micromegas-GEM (MM-GEM) with 1 and 2 mm transfer gap [3] were compared with a standard Micromegas. The resulting spark probabilities are shown in Fig. 4.15 as a function of the total gain and for different GEM high voltages. Several important observations can be made:

1. A significant reduction of the spark probability can be obtained with modest GEM gains (less than 10)
2. For moderate GEM gains the spark probability does not depend on the transfer gap size
3. For larger GEM gains a larger transfer gap further reduces the spark probability
4. The reduction of the spark probability seems to saturate at high GEM gains
5. The slope of the spark probability as a function of the total gain increases at small gains for MM-GEM, in the large GEM gain domain. This tendency can actually be seen for the standard Micromegas at very small gain.

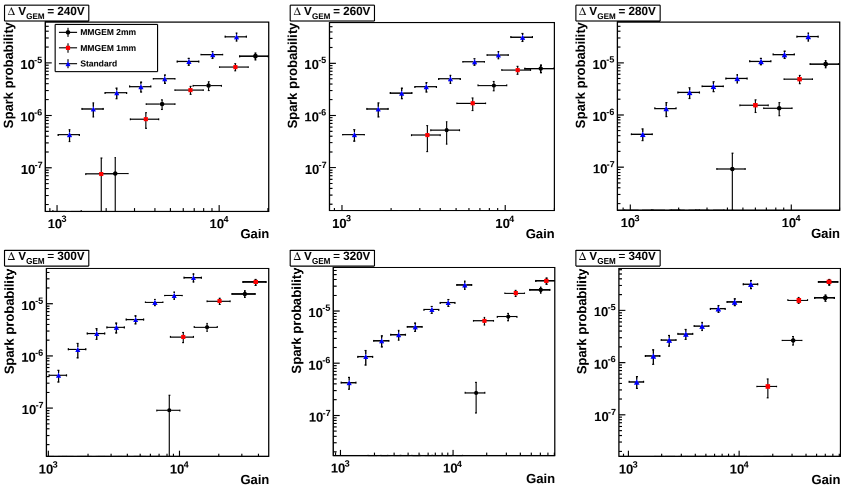

Figure 4.15: *Spark probability as a function of the gain for MM-GEM detectors in a 3 GeV/c pion beam, and for different GEM gains. Data from a standard Micromegas are shown for comparison [105].*

---

[3] The transfer gap is the distance between the micro-mesh and the GEM foil.

4.4.4 From the Raether limit to a charge density limit

All the effects described above cannot be explained in a model where the spark is only initiated by the creation of a critical number of electrons. It should be mentioned, however, that the importance of the density was already partly taken into account in the original simulation, as the model considered large energy deposits occurring in a relatively small volume. But this simulation did not distinguish from energy deposits appearing at different heights in the detector volume. Because of the transverse diffusion of the primary electrons, a given energy deposit is more likely to generate a discharge if occurring close to the micromesh.

In the new simulation, a pointlike energy deposit E_{dep} is converted into a surface charge density d_S by estimating the mean area of the electron cloud at the readout strip level. The transverse extension of the cloud being proportional to the square root of the distance z to the readout strips (usual diffusion model), one can write:

$$d_S = \frac{4 \times G \times E_{dep}}{\pi w_i (a(E,B) \times \sqrt{z})^2}, \tag{4.10}$$

where w_i is the ionization potential of the gas. The parameter $a(E,B)$ is closely related to the transverse diffusion of the gas, and can be estimated through Garfield simulation for any electric and magnetic fields. In practice, a systematic transverse diffusion of 100 μm was added to the term in $a \times \sqrt{z}$ to account for the additional spread coming from the avalanche in the amplification gap.

In the case of a MM-GEM detector, the gain appearing in the above equation is the total gain if the energy deposit occurs in the conversion region, and only the Micromegas one if it occurs in the transfer gap. The sparking condition now reads:

$$d_S \geq d_S^{lim}, \tag{4.11}$$

where d_S^{lim} is a critical surface charge density.

4.4.5 Comparison with data

The resulting discharge probabilities obtained with either the Raether or the density limit are shown in Fig. 4.16. The density limit exhibits a very similar behaviour with the gain, though with a slightly smaller slope. The adjustment gives:

$$d_S^{lim} = 2 \times 10^9 \,/mm^2 \tag{4.12}$$

It means that the data reproduced by the Raether condition can alternatively be described in terms of a critical charge density.

The same simulation was applied to two MM-GEM detectors with 1 and 2 mm transfer gaps respectively. Figure. 4.17 (left) illustrates the effects of both the GEM gain and the transfer gap on the spark probability. These effects are in qualitative agreement with observations made above, namely:

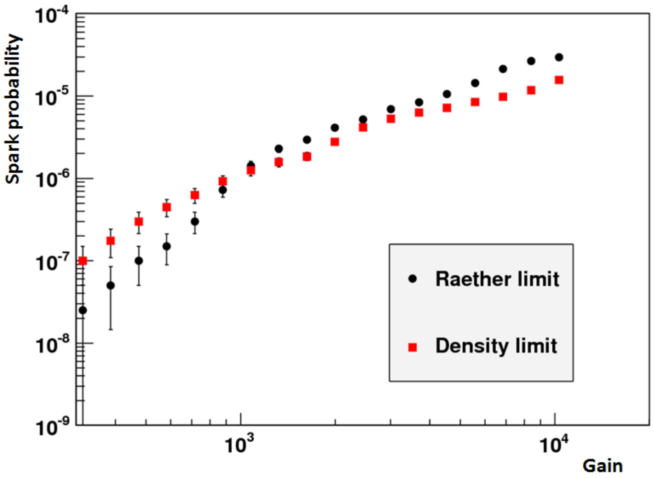

Figure 4.16: *Discharge probability obtained with a Geant4 simulation of 3 GeV/c* π^-*, using either a Raether or a density limit.*

- for small GEM gains at a fixed total gain, most of the sparks originate from energy deposits occurring in the transfer gap where only the micro-mesh gain plays a role. These sparks are suppressed when transferring a small part of the gain from the micro-mesh to the GEM (1). In this regime, the size of the transfer gap is of no importance (2).
- for large GEM gains, all the sparks initiated by energy deposits in the transfer gap have been suppressed. The observed sparks now come from energy deposits in the drift gap. These energy deposits being amplified by the total gain, a further transfer of the gain from the micro-mesh to the GEM does not further suppress the sparks (4). In this case, a higher transfer gap enhances the transverse diffusion and thus lowers the charge density (3).
- for large GEM gains and very small micro-mesh gains, the energy deposit required to initiate a spark becomes higher than a deposit corresponding to the stopping of a highly ionizing particle. In this regime the slope of the spark probability as a function of the total gain is strongly enhanced (5).

A quantitative comparison between the simulation and the data is shown in Fig. 4.17 (right) for an intermediate GEM gain. Using the same critical charge density as above, a fair agreement is obtained simultaneously for the standard Micromegas and the two MM-GEM.

4.5 Reduction of discharge effects

We have seen that a significant reduction of the discharge probability can be obtained by the use of light gases or of a GEM foil acting as a preamplifier. Another approach consists

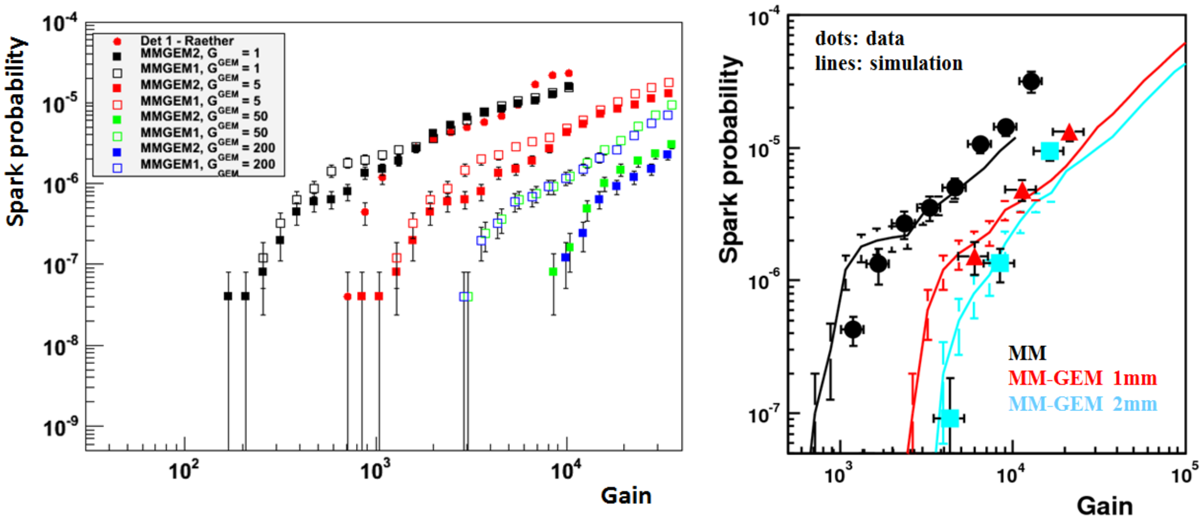

Figure 4.17: *(Left): Simulated spark probability in the 1 and 2 mm MM-GEM as a function of the total gain, for different GEM gains. (Right): Comparison of the spark probability from the data (points) and from the simulation (lines) for the Micromegas and the two MM-GEM (with a GEM gain of 30).*

in reducing the *effects* of the discharges in the detector, and in particular the dead time. From Fig. 4.3, it is clear that only three parameters can be optimized:

- the micro-mesh voltage drop.
- The reloading time, *i.e.* the time needed to reach the voltage corresponding to the beginning of the efficiency plateau.
- The area affected by the discharge.

4.5.1 Reduction of voltage drop through individual strip polarization

The first strip polarization scheme introduced in the late 1990s is illustrated in Fig. 4.18 (left). In this case, the strips are connected to the ground through the small impedance of the charge amplifier. When a discharge occurs, the strip potential cannot vary a lot, and the discharge is quenched only after a significant drop of the micro-mesh voltage. This drop can be reduced by adding an individual capacitance between each strip and its charge amplifier, see Fig. 4.18 (right). Such a capacitance decouples the strips and forces the (smaller) discharge current to be evacuated through the large polarization resistance [4]. The potential of the strip(s) involved in the discharge quickly increases and therefore limits the drop of the micro-mesh voltage. In practice, however, we observed that this drop can still exceeds 100 V as in Fig. 4.3.

---

[4] usually of the order of 10 to 100 MΩ

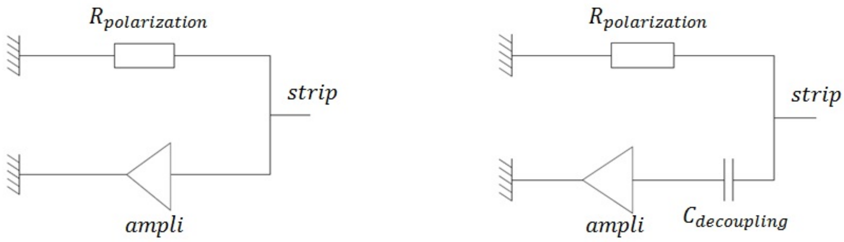

Figure 4.18: *(Left): early strip polarization scheme, with direct connection to the charge amplifier. (Right): strip polarization with individual capacitance for strip decoupling. This scheme appears with the SFE16 electronics developed for the Compass experiment [47].*

4.5.2 Reduction of reloading time through optimization of the filter components

The first goal of the HV filter, as introduced in Chapter 2, is to cut the noise originating from parasitic high frequencies. It can also provide some protection in the case of a discharge by limiting the current in the detector. Its components also determine the two reloading mechanisms to bring the micro-mesh voltage back to its initial value:

- a rapid charge equilibrium with the ballast capacitance through the resistance R_f (see Fig. 2.4).
- A complete reloading by the high power supply.

More quantitatively, and assuming the first process is much faster, the micro-mesh high voltage after the discharge at $t = 0$ can be written as:

$$V(t) = V_n - \frac{\Delta V}{C_{det} + C_f} \left(C_f \times e^{-t/\tau_f} + C_{det} \times e^{-t/\tau_{alim}} \right), \tag{4.13}$$

where V_n is the nominal voltage, ΔV is the voltage drop during the discharge, and τ_f, τ_{alim} are the rise times associated to the two mechanisms[5]. One can derive for the former:

$$\tau_f = \frac{R_f \times C_f \times C_{det}}{C_f + C_{det}}, \tag{4.14}$$

showing that the charge equilibrium can take place in a few microseconds only. In practice, R_f should not be chosen below ~100 Hz, otherwise voltage oscillations appear. This mechanism is generally not sufficient to reload the detector well enough, except in the case of small detectors with C_{det} of the order of 1 nF or less. For the latter, an intuitive expression can be obtained in the case where $R_f \ll R_{hv}$:

$$\tau_{alim} = (R_f + R_{hv}) \times C_{det} + R_{hv} \times C_f \tag{4.15}$$

---

[5] There is *a priori* a third term related to a second rise time due to the power supply reloading, but in practice its contribution is negligible.

This value can be as high as a few tens of milliseconds, depending on the frequency range the filter should cut.
In the general case, a minimization under constraints should be performed on the time needed to reach V_n-ϵ, ϵ depending on the position of the working point along the efficiency plateau. This optimization depends on the initial voltage drop, ΔV, which cannot be accessed analytically. However, simulations of the electronic scheme can provide realistic values, as illustrated in Fig. 4.19 obtained with LTSpice. A complete example of minimization for the Clas12 detectors is available in [65].

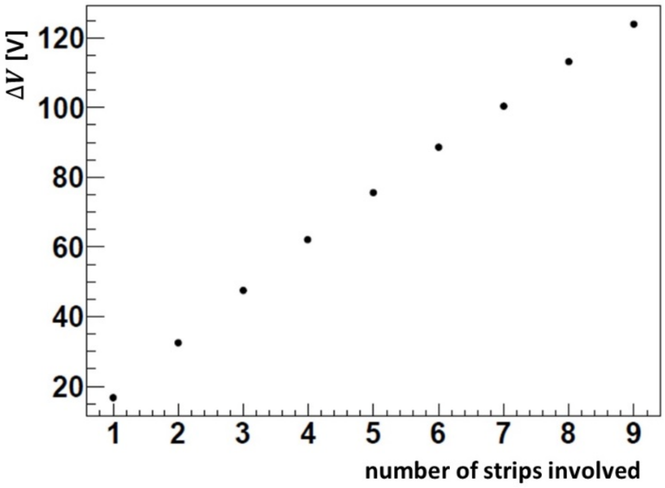

Figure 4.19: *LTSpice simulation of the micro-mesh voltage drop, as a function of the number of strips involved in the discharge, for individual strip capacitance of 74 pF.*

4.5.3 Micro-mesh segmentation

Another possibility to reduce the discharge effect is to limit its influence area. Within a same detector, the micro-mesh can be segmented in different pieces so that a discharge in one piece doesn't affect the others. In addition, such a segmentation lowers the capacitance of each micro-mesh, resulting in a shorter recovery time as shown by expressions derived in the previous section.
On the other hand, the segmentation introduces additional dead zones and decreases the acceptance. However, the width of the dead zone can be lowered to a few hundred microns with the use of a micro milling cutter, as shown in Fig. 4.20. This segmentation can be either parallel or perpendicular to the readout strips. In the first case, a segmented prototype has been tested in a regime where one micro-mesh was in a constant discharge mode. Acquisition with cosmics revealed no influence on the neighbouring micro-meshes, neither on the noise nor on the detection efficiency. In the perpendicular case, discharges on one micro-mesh induced a small current on the adjacent one, as shown in Fig. 4.21, certainly because of the common strips. Measurement with cosmics indicated that the micro-mesh in constant discharge regime lowered the efficiency of its neighbour by an amount equivalent to 5 V.

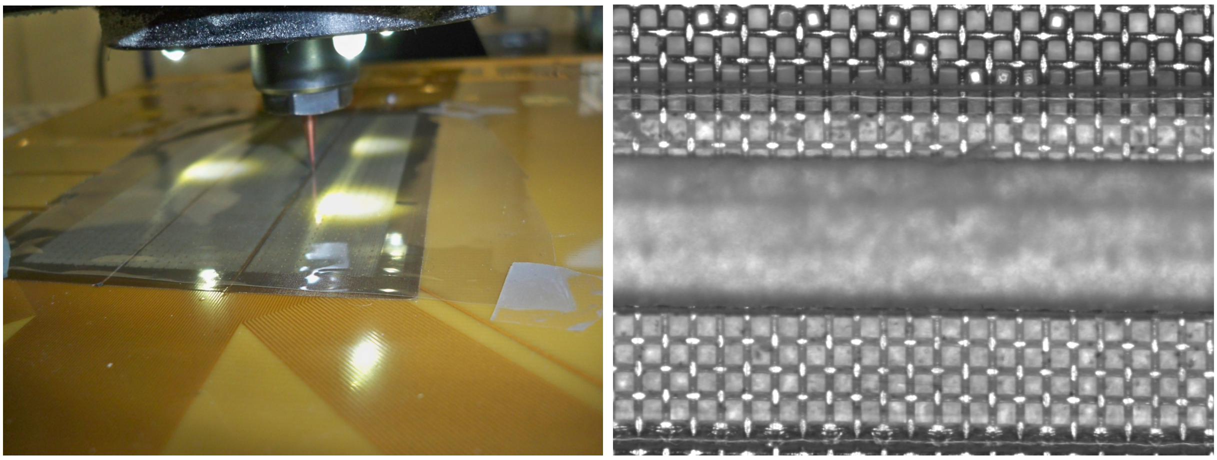

Figure 4.20: *(Left): 0.3 mm diameter milling cutter performing a micro-segmentation on a Micromegas. (Right): zoom on the resulting micro-segmentation.*

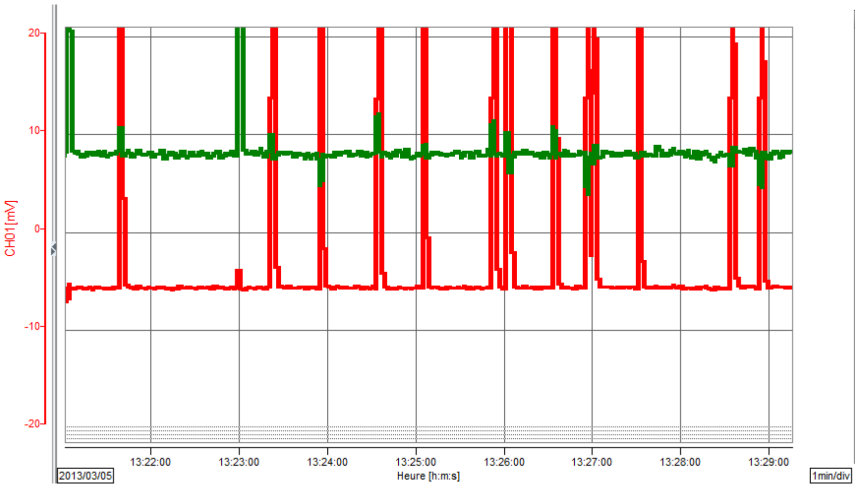

Figure 4.21: *Current monitoring of two adjacent micro-meshes with perpendicular segmentation. Discharge on a given micro-mesh correspond to large peaks, and are often associated with a smaller peak induced on the other.*

4.5.4 Resistive technologies

An innovative way to reduce the effect of discharges consists in adding a resistive layer between the micro-mesh and the readout strips. This layer is separated from the strips by an insulator, for example a Kapton foil. This idea first emerged from the need to spread the signal on several readout elements (pads), to limit the size of the electronics. Such a spreading is not necessarily appropriate in high flux environments, and two main variants were later introduced with discontinuous resistive layers, as illustrated in Fig. 4.22:

- resistive strip parallel to readout strips, with a connection to ground via a common resistance. This variant was introduced in the course of the Atlas NSW project.
- Burried resistors, adapted to pixel readout, with a connection to readout pixels

through a dedicated resistance.

In all cases, the signal is transferred to the readout elements by capacitive effect, and the charges are evacuated through the resistances. When a discharge occurs, the corresponding current leads to a very rapid increase of the resistive element potential which quenches the discharge before any significant drop of the micro-mesh potential. Measurements with an alpha source revealed that discharges still occur, but with a voltage drop lower than 2 V. For such a small value there is usually no deviation from the efficiency plateau, and the corresponding dead time is thus negligible. The price to pay for this spark protection is a higher sensitivity to dust, and potential problems of charge evacuation at very high rate. The overall performance of these detectors is presented in Chapter 2.

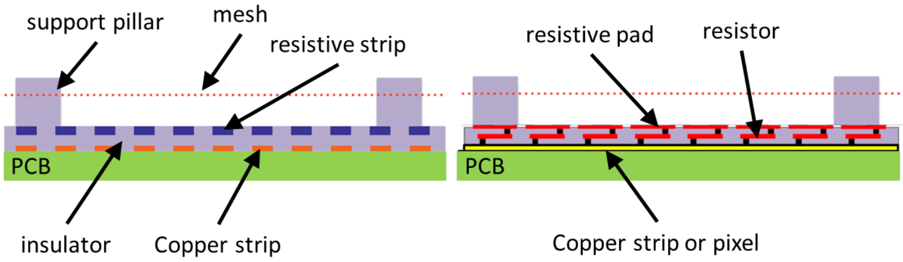

Figure 4.22: *Layout of the resistive strip (left) and buried resistor (right) technologies.*

Chapter 5

Micromegas with genetic multiplexing

5.1 Introduction

The Micromegas was originally designed to stand very high fluxes of particles with an excellent spatial resolution. The recent industrialisation attempts of the bulk technology driven by the LHC upgrade allows for massive productions of large area detectors in the near future. But the micro-pattern structure of the Micromegas requires a huge number of readout elements to equip a whole tracker, from 30000 for Clas12 to several millions for the Atlas New Small Wheel. With a typical cost of ≈ 1-4 euros per channel, the electronics represents a significant budget for a given experiment and can limit the performance of an apparatus. This cost, as well as other issues on integration, power consumption, or cooling are even prohibitive in some applications, like muon tomography. Very often, however, the incident flux per recording element is not critical. For one particular event, the signal is localized on a few electronic channels, the others being useless. Even in high luminosity experiments, the spatial resolution is a stronger constraint for fine granularity than the incident flux in some parts of the acceptance. A simple but illustrative example is provided by the Compass experiment at Cern, where twelve layers of Micromegas detectors are installed downstream of the target. In spite of an incident flux of the order of a few tens of MHz per layer (in the strip region), a rapid calculation shows that less than 5% of the electronic channels carry a useful signal for a given event. In low flux experiments, *e.g.* with cosmics, the part of the electronics carrying no useful information exceeds 99%. The possibility to reduce the number of electronic channels therefore appears as an important aspect to optimize the use of Micromegas detectors in existing or future applications, and is the main focus of the present chapter.

5.2 Principle of multiplexing

A simple but efficient way to reduce the size and the cost of the electronics consists in grouping several recording elements together, and in connecting them to a single electronic channel. This reduction is in practice limited by two requirements:

- maintaining a good detection efficiency, because the connection of several recording elements to a single channel increases the input capacitance and lowers the S/N ratio.
- Limiting the number of ambiguities by choosing an appropriate grouping pattern. Indeed such a grouping inherently leads to a certain loss of information. In particular, if several particles leave a signal simultaneously in the detector, some ambiguities can arise during the demultiplexing process.

The development of robust, high gain MPGDs as well as low noise electronics now offers quite comfortable S/N ratios and provides some margin for the former requirement. For the latter, two strip multiplexing techniques have been developed and succesfully tested at Saclay with large Micromegas prototypes. Special emphasis will be given on the genetic multiplexing (see Section 5.2.2) which appears as the most efficient one. Besides, it can be easily adapted to the incident flux of particles and to other MPGDs, Drift Chambers or scintillators.

5.2.1 Double sided multiplexing

This concept is based on the possibility to manufacture double sided bulk detectors, and has been designed by Aune. The top face active area of the Micromegas is equipped with n groups of m thin strips each, *i.e.* $m \times n$ strips in total, readout by m electronic channels in such a way that the i^{th} strip of each group is connected to the i^{th} channel. The bottom face is built from n large strips connected to n electronic channels. Each large strip is back-to-back with a group of m thin strips, and their dimensions exactly match, as illustrated in Fig. 5.1.

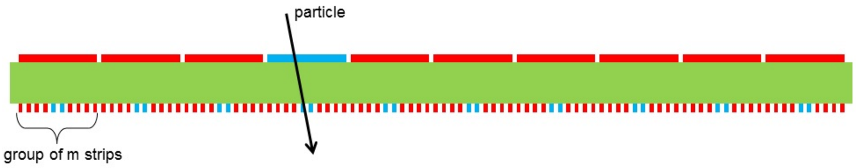

Figure 5.1: *Principle of the double sided multiplexing. Two back-to-back detectors are built on a single PCB, and equipped with large non multiplexed and thin multiplexed strips (in red and blue). The exact localization of a particle (array) on thin strips is provided by the additional information from the large strip side.*

When a particle crosses the detector, it leaves a signal on some thin strips, as in any standard detector. Because of the multiplexing, it is not possible to determine *a priori* in which group of strips the signal has appeared. But a signal is also recorded on the other side of the detector, usually on a single large strip. This additional information identifies which group of thin strips has seen the particle. The system is then equivalent, in terms of spatial resolution, to a detector with $m \times n$ strips, though read with only $m + n$ channels.

This type of multiplexing has been used to perform the muon reconstruction in the large Clas12 cosmic rays bench equipped with two 60×60 cm^2 scintillators which provide the trigger coincidence. Six such double sided PCBs were transformed into bulks at the Saclay MPGD workshop, and integrated with an aluminum frame on both side to ensure the gas tightness within a 1 cm drift gap. The active area is 50×50 cm^2, with a thin (resp. large) strip pitch of 488 μm (resp. 1.56 cm) including a 100 μm interstrip. This configuration corresponds to m=n=32, so that a whole detector is readout with a single connector of 64 channels. The large acceptance of this telescope allows the characterization of a Clas12 prototype within one or two days, with a trigger rate of the order of 5 Hz. An event display of a cosmic particle is shown in Fig. 5.2 with four CosMulti.

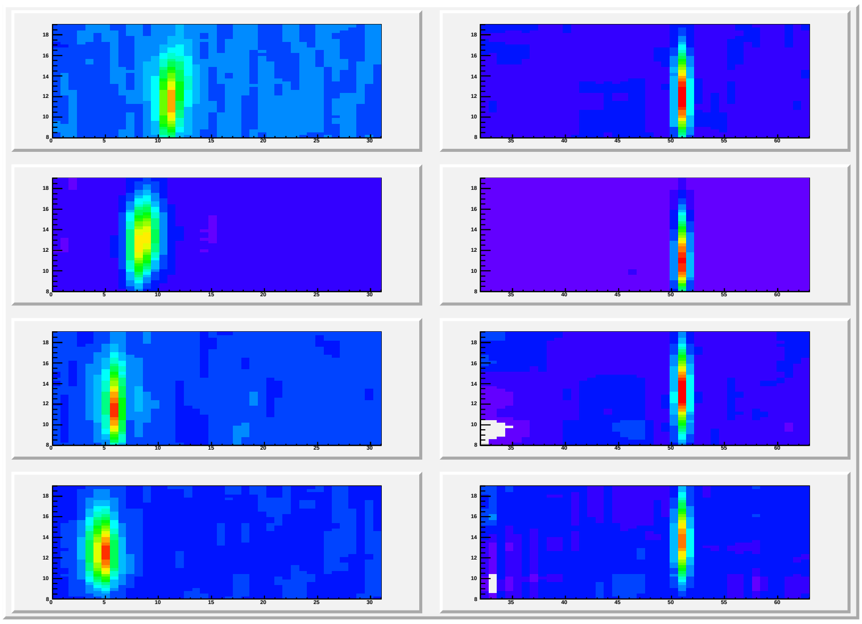

Figure 5.2: *Event display of a cosmic particle in four CosMulti detectors. The left (resp. right) panels shows the signal amplitude on thin (resp. large) strips, as a function of the strip number (X) and time (Y). As expected, the signal on thin strips is spread over several recording elements.*

In spite of its good performance for tracking, this multiplexing technique suffers from several limitations affecting both its detection efficiency and its ability to localize the particles without ambiguities. The 2 nF capacitance of each group of thin strips significantly reduces the S/N ratio [1], and the efficiency does not exceed 85-90%, even with a 1 cm drift gap. The double bulk process apparently degrades the quality of the detectors, and increases the risk of failure [2]. Furthermore, two particles crossing the detector simultaneously give rise to four different associations between large and thin strips, as illustrated in Fig. 5.3 (top). With a single detector, this ambiguity is unsolvable. Ambiguities can even arise with a single particle crossing the detector with a large angle, or on the edge of a large strip, as in this case thin strips do not correspond to the large one (Fig. 5.3 (bottom)). Finally, such

---

[1] The capacitance of a large strip is only 1 nF.

[2] Indeed, if one side does not work properly, the whole detector is not operational.

a detector is not adapted to X-ray detection, and the thick PCB considerably increases its radiation length. For all these reasons, another type of multiplexing was investigated, as described in the next section.

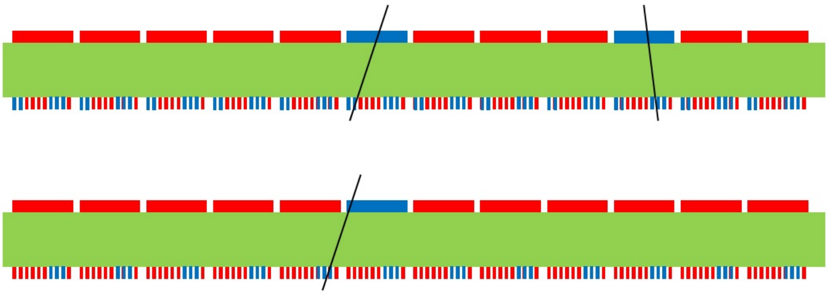

Figure 5.3: *Example of ambiguities with the double sided multiplexing. (Top): case where two particles cross the detector simultaneously, leaving four possible associations between thin and large strips. (Bottom): case where a single particle crosses the detector on the edge of a large strip, leading to a wrong combination.*

5.2.2 Genetic multiplexing

Principle

It is important to understand that any grouping implies a certain loss of information. This is the very reason why ambiguities can occur. The previous pattern multiplexes groups of thin strips, and therefore loses the (crucial) information on which group really recorded the signal. This loss has to be compensated by an additional knowledge which is provided by the large strip side. A different approach consists in looking for *redundant* information in the signal, and to design a grouping pattern in such a way that the lost information exactly coincides with this redundancy. Thus no crucial information for the localization of the particle is lost.

It turns out that in Micromegas detectors, and more generally in any MPGD, a particle usually leaves a signal on several, *neighbouring* strips. This feature clearly carries a redundancy, and can be utilized to localize the particles with an appropriate grouping pattern. Suppose indeed that two neighbouring strips i and $i+1$ are connected to two given channels a and b, and each of these channels are in turn connected to several other strips. The connection is made in such a way that there is only one set of two consecutive strips for a given set of two channels. Therefore if a signal is recorded only on channels a and b, it is almost certain that it results from the passage of a particle close to strips i and $i+1$. This principle is illustrated in Fig. 5.4. Such a pattern does not require additional large strips anymore by explicitely assuming that a particle leaves a signal on at least two neighbouring strips. This can be guaranteed in practice for most of the events, either by lowering the pitch size or by increasing the transverse diffusion with a larger drift gap or a lower drift field. It can be generalized to the case where a signal is recorded on k neighbouring strips,

$k > 2$. The term **genetic multiplexing** was chosen for the analogy with DNA and genes, as the sequence of fired channels uniquely codes the position of the particle in the detector.

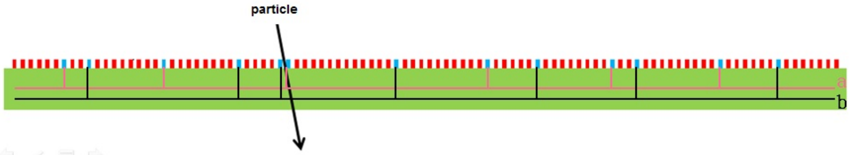

Figure 5.4: *Principle of the genetic multiplexing. A particle (array) leaves a signal on two neighbouring strips which are connected to two given channels. These channels are connected to other, non neighbouring strips in the detector. The recorded signals on these two channels therefore localize without ambiguities the particle in the only place where strips are consecutive.*

Construction scheme

Though the idea described above is relatively simple, the construction of the corresponding {strips} ↔ {channels} connection in a systematic and optimal way is not a trivial problem. For each strip of the detector, one has to specify the channel number to which it should be connected. If the detector contains n strips and is read with p channels, then the connection can be described by a n-list of numbers ranging from 1 to p. In a non multiplexed detector, $n = p$, and the list is simply {1,2,3,...,n}. In the following, $p < n$, and a convenient way to write this n-list is to form a table with p columns and n boxes in total. The i^{th} box contains the channel number which is connected to the i^{th} strip.
The genetic multiplexing imposes *a priori* only two constraints on this n-list:

- the same number cannot appear twice in succession. This would indeed mean that two consecutive strips are connected to the same channel;
- any unordered doublet (or k-uplet in the case where k strips record a signal) of channel numbers should appear at most once in the whole list.

Starting with p channels, the number N_2 of unordered doublets is given by the combinatorial formula:

$$N_2 = \frac{p \times (p-1)}{2} \tag{5.1}$$

The theoretical, maximum number of strips that can be readout with p channels is therefore:

$$n_{max} = N_2 + 1 = \frac{p \times (p-1)}{2} + 1 \tag{5.2}$$

as a n-list contains $n-1$ doublets.
A first attempt to form a maximal n_{max}-list is to choose the channel numbers randomly, one after the other, with the two constraints given above. Such a construction is illustrated in Table 5.1 for $p=9$. After the last 1, all doublets containing this number have been used, and the construction is blocked while not using all the available doublets. In general, this method is very unlikely to provide a n_{max}-list.

$\mathit{1}_{1}$	$\mathit{2}_{2}$	$\mathit{3}_{3}$	$\mathit{4}_{4}$	$\mathit{5}_{5}$	$\mathit{6}_{6}$	$\mathit{7}_{7}$	$\mathit{8}_{8}$	$\mathit{9}_{9}$
2_{10}	4_{11}	1_{12}	3_{13}	5_{14}	8_{15}	3_{16}	6_{17}	9_{18}
3_{19}	7_{20}	1_{21}	9_{22}	4_{23}	6_{24}	1_{25}	5_{26}	2_{27}
8_{28}	1_{29}							

Table 5.1: *Random construction of a list of doublets for* $p=9$ *channels. Each connexion is represented on the form* X_Y*, where* X *is the channel number and* Y *the strip number along the detector. The first line is just a numbering convention.*

An alternative solution was found, and turned out to be optimal when p is a prime number. The list is constructed with $(p-1)/2$ sublists of p channel numbers ordered according to the formula:

$$1 + [(i \times s)\ mod\ p] \tag{5.3}$$

for the s^{th} sublist, and with i ranging from 0 to $p-1$. To complete the list, the first channel can be repeated once more at the end. This construction is given in Table 5.2 for $p=11$. It can be checked that each possible doublet occurs exactly once in the list.

1_{1}	2_{2}	3_{3}	4_{4}	5_{5}	6_{6}	7_{7}	8_{8}	9_{9}	10_{10}	11_{11}
1_{12}	3_{13}	5_{14}	7_{15}	9_{16}	11_{17}	2_{18}	4_{19}	6_{20}	8_{21}	10_{22}
1_{23}	4_{24}	7_{25}	10_{26}	2_{27}	5_{28}	8_{29}	11_{30}	3_{31}	6_{32}	9_{33}
1_{34}	5_{35}	9_{36}	2_{37}	6_{38}	10_{39}	3_{40}	7_{41}	11_{42}	4_{43}	8_{44}
1_{45}	6_{46}	11_{47}	5_{48}	10_{49}	4_{50}	9_{51}	3_{52}	8_{53}	2_{54}	7_{55}
1_{56}										

Table 5.2: *Ordered construction of a serie of doublets for* $p=11$ *channels, allowing* $n = n_{max} = 56$*. Each connexion is represented on the form* X_Y*, where* X *is the channel number and* Y *the strip number along the detector.*

This construction can be extended with minor adaptations to the cases where p is not prime in order to obtain large lists. To do so, one can construct the n-list step by step, taking the first available channel number that forms a new doublet with the previous number. For $p=9$ and 10 for example, one obtains lists of $n=37$ and 42 strips respectively. Recently, it has been proven using graph theory that n_{max}-lists can be constructed with odd p, while even p yields only $\frac{p\times(p-2)}{2}+2$ [107].
A practical subtlety arises from the possibility for a detector to record a signal on more than two consecutive strips. This triggers the question of k-uplets ($k>2$) repetition in the present system which is designed to avoid only doublet repetition. As we can see in

the example shown in table 5.2 with the sequence {9-1-5-9}, triplets (and more generally k-uplets) can occur more than once. However, one of the most important features of the proposed construction for prime numbers of channels is that the sublists can be reordered at will, in order to minimize the repetition of k-uplets (it seems feasible up to k around $p/4$).

All the previous discussion can be generalized, to a large extent, to the case where a signal is recorded on at least k strips (k >2). One can then construct much larger lists with a maximal size given by:

$$n_{max} = N_k + (k-1) = \frac{p!}{k!(p-k)!} + (k-1) \tag{5.4}$$

The number of combinations being very large, it is rarely necessary to implement all possible k-uplets.

Degree of multiplexing and incident flux of particles

The statement that the information loss exactly matches the redundancy of the signal is only valid when a single particle crosses the detector. In the presence of several particles, the corresponding signals have no reason to be on consecutive strips, so that the overall redundancy does not compensate anymore the information loss. In other words, some ambiguities can arise. For example, in the construction given in Table 5.2, if two particles leave a signal on channels {5-7} and {8-11} respectively, three different combinations appear, namely {5-7;8-11}, {5-8;7-11} and {11-5;7-8}, the last two being fake. This happens because all the possible doublets are used in the list. A first option to limit the ambiguities therefore consists in using only a fraction of the available doublets (or k-uplets). Of course the electronics reduction will be smaller, but the probability to measure fake hits will be suppressed. If one defines the degree of multiplexing as the number of doublets actually used:

$$d = \frac{n-1}{p(p-1)/2} \tag{5.5}$$

the probability of each fake combination in the above example will be d^2. A preliminary simulation of a Micromegas detector of 1024 strips and readout with different channel numbers gives an estimate of the probability of ambiguities [3] as a function of n/p, see Fig. 5.5. It shows that even with a 10 kHz/cm^2 incident flux, a reduction by a factor of two of the electronics (corresponding to d of the order of 1%) only leads to a 1% ambiguity level.

Another solution to limit the ambiguities is to use the extra information available such as the signal spread. For exemple, the strip measuring the largest signal is most probably in the center of the cluster (when k >2), while smaller signals are recorded on the edges. One can also use the other detectors of a given setup to select between the possible options

---

[3] The ambiguity was defined here as the case where the difference between the reconstructed and true position is larger than three times the spatial resolution of the detector.

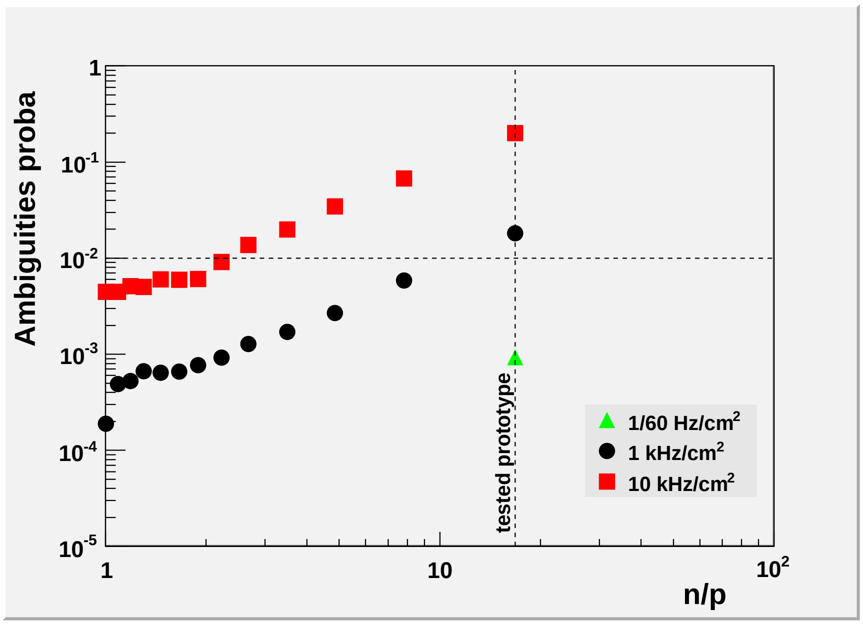

Figure 5.5: *Simulation of the probability of ambiguities as a function of* n/p*,* n *=1024, for different fluxes of (independent) particles. The vertical line corresponds to the configuration of the prototype described in Section 5.3, and the horizontal line shows the 1% ambiguity level.*

left by ambiguities. In a tracker for example, the continuity of the trajectory can help to distinguish between the different combinations. In general only a careful simulation of the detector in its setup can allow a precise estimate of the effective fraction of ambiguities. The degree of multiplexing should consequently be chosen on a case by case evaluation depending on the flux of particles, the detector design and the proportion of ambiguities considered acceptable.

5.2.3 2D multiplexing

The genetic multiplexing cannot be easily applied to pads or pixels, because of the higher number of neighbours. In the case of a TPC however, the signal redundancy is much higher as a whole track segment is observed. The difficulty is then to design a multiplexing pattern without introducing an anisotropy, and in particular special directions where the demultiplexing would fail. In theory the best solution against anisotropy would be to implement a random multiplexing, but in practice the design of the corresponding routing seems not possible. An alternative consists in extending the genetic multiplexing in 2 dimensions, *i.e.* to muliplex on the basis of 2 prime numbers p_1 and p_2. A standard multiplexing with p_1 is performed in one direction, and the second direction is obtained by multiplexing p_2 1D groups. The number of channels is then $p_1 \times p_2$, with a maximum number of pixels equals to:

$$(N_{p_1}+1) \times (N_{p_2}+1) = \left(\frac{p_1 \times (p_1-1)}{2}+1\right) \times \left(\frac{p_2 \times (p_2-1)}{2}+1\right) \tag{5.6}$$

This requires that p_1 return strips can be inserted below a single pixel line. For example, 247 channels (13×19) corresponding to half a FEU from Clas12/Dream can equip up to 13588 pixels, provided that pixels are as large as $\sim 13 \times 0.3 \approx 4\,\mathrm{mm}$ for the routing.

5.3 Characterization of prototypes

5.3.1 1D prototype

Description of the detector

A first prototype has been built in 2013 to validate the principle of the genetic multiplexing on a large area. In order to simplify the mechanical integration, the same PCB size and strip pitch as the CosMulti detectors were used, corresponding to 1024 strips and a $50 \times 50\,\mathrm{cm}^2$ active area. The number of channels was chosen to be the highest prime number below 64 (61), to keep a single readout connector. According to Eq. (5.2), up to 1831 strips can be readout in these conditions, which means that 56% of all the available doublets occur in the prototype. A careful reordering of the sublists was performed to limit the repetition of k-uplets, $k > 2$, and it was checked that no k-uplets can occur twice up to $k = 16$. Thirteen 16-uplets are then repeated, but the corresponding, potential ambiguity is quite limited. Indeed, two such 16-uplets strongly overlap, in a sequence of the form a;b;c;d;...m;n;o;p;a. The routing between the channels and the strips is shown in Fig. 5.6 (left). From this PCB, the bulk Micromegas was manufactured at the Saclay workshop by M. Anfreville. Apart from a small mesh defect which appeared during the process (see Fig. 5.6 (right)), high voltages higher than 800 V were successfully applied on the mesh in the atmospheric air.

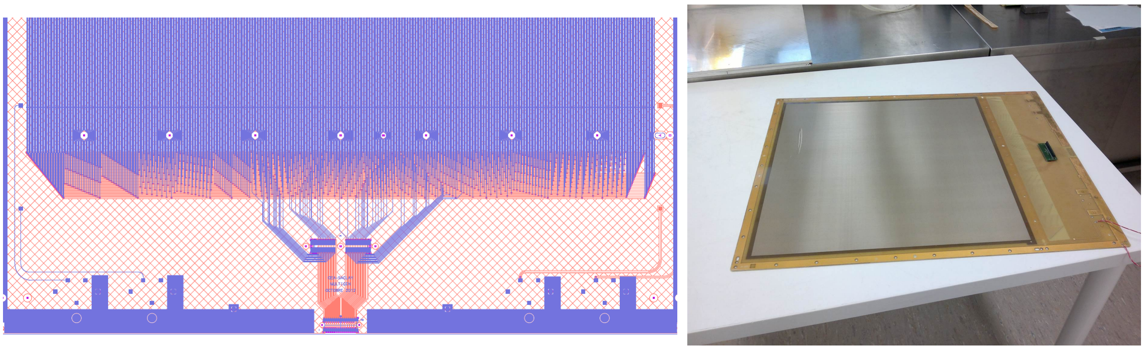

Figure 5.6: *(Left): routing between the 61 channels and the 1024 strips for the MultiGen 1D prototype; (right): picture of the PCB after the bulk process. A small mesh defect is visible on the left part.*

Results

The detector was tested in a standard Argon-Isobutane (95-5%) gas mixture with a 1 cm drift gap and readout by the T2K/After electronics. The effective gain was first measured as a function of the mesh high voltage. This gain is calculated directly from the charge effectively collected by the electronics, and therefore takes into account the signal loss due to the large capacitance of the strips (1300 pF) and of the cable (110 pF). Effective gains close to 3000 were routinely achieved, as shown in Fig. 5.7 (left). Comparing the resulting signal amplitude with the measured electronic noise (roughly 4000 electrons), the average S/N ratio was found to be around 35. Figure. 5.7 (right) shows the cluster size distribution with cosmics. Thanks to the large drift gap and a moderate electric field, only 2% of the events could not be localized on the detector, failing the criterion to have a cluster size of at least two.

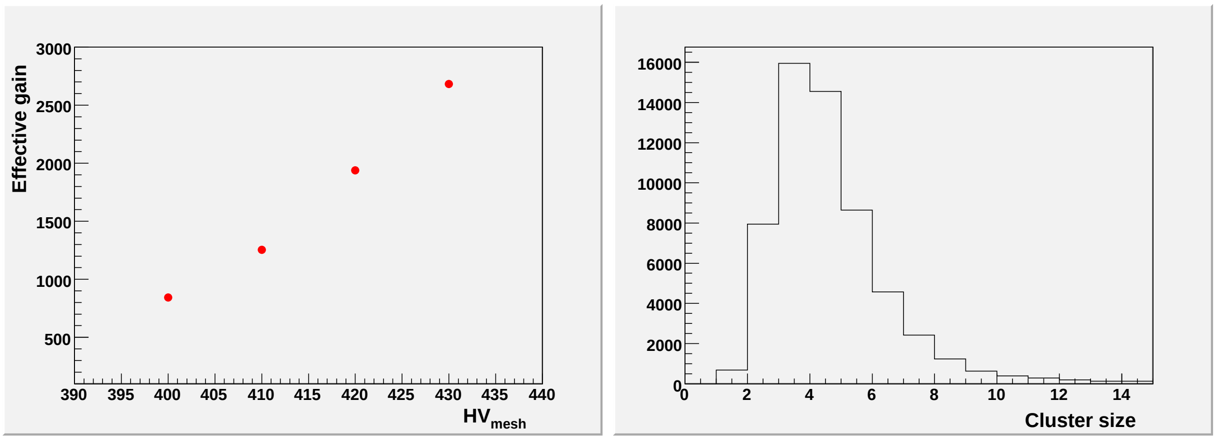

Figure 5.7: *(Left): effective gain of the detector as a function of the mesh high voltage; (right): cluster size distribution with cosmics.*

The 2D efficiency with cosmics is displayed on Fig. 5.8. The detector is quite homogeneous, with an average efficiency of 88% at 435 V. This value, though correct for a first prototype, shows that the efficiency plateau cannot be reached, as already suggested by the limited effective gain.

5.3.2 2D prototypes

Description of the detectors

In order to increase the compactness and enlarge the potential application fields of the multiplexed detectors, a 2D version has been designed and built. The charge sharing between the two coordinates leads to a significant efficiency loss, so the resistive strip technology has been used to increase the maximal available gain. The resulting layout consists of the following layers:

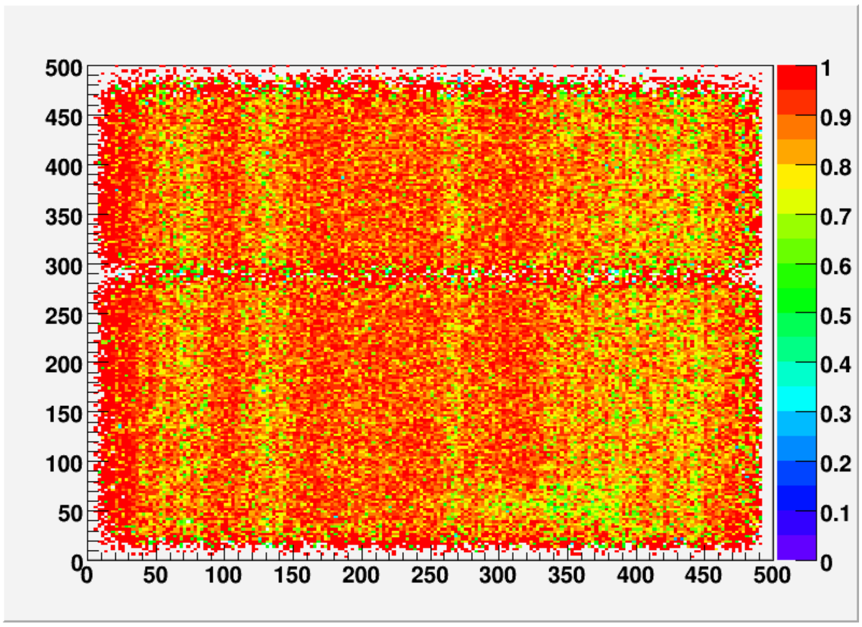

Figure 5.8: *2D efficiency of the 1D MultiGen prototype with cosmics. The horizontal line is an acceptance artefact of the cosmic bench used at that time. The mesh defect is visible on the bottom right corner.*

- the mesh;
- a layer of resistive, X strips, with a 488 micron pitch and 380 micron strips;
- a layer of readout Y strips with the same pitch, and thin, 100 micron strips;
- a layer of readout X strips with the same pitch, and 380 micron strips.

Thinner Y strips allow for a significant signal to be induced on the most inner X strip plane. The T2K/After setup was replaced by a FEU from the Clas12/Dream electronics which is more adapted to large capacitance. The multiplexing pattern is the same on both coordinates, and is identical to the 1D prototype. There is *a priori* not enough correlation between X and Y positions and signals, so no multiplexing has been introduced between the coordinates. Four such detectors have been initially manufactured at Cern. Another detector has been partially built by the Elvia group, and the bulk part has been finalized at Cern.

Results and performance

The first feature of these detectors is an asymmetry between X and Y strips due to the orientation of resistive strips. Y clusters are much larger because of the slow, perpendicular charge evacuation. This effect is particularly visible on Fig. 5.9, showing the time development of the signal. The maximum of edge strips are delayed in time, while an undershoot develops on central strips as the electrons move away.

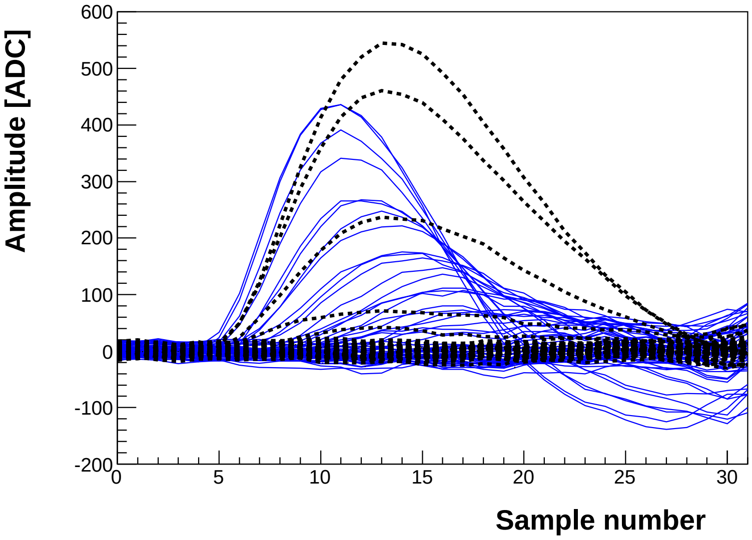

Figure 5.9: *Event display on Y (blue) and X (black) coordinates of a MultiGen 2D detector in the cosmic test bench. Pedestals and common mode have been subtracted.*

The 2D efficiency curves are displayed in Fig. 5.10 for three detectors. In spite of the charge sharing, a comfortable plateau is reached for all the detectors thanks to the resistive technology and the new electronics. The inter-strip distances and layer thickness, inspired from NSW prototypes allows both coordinates to receive approximately the same charge, and thus to have the same efficiency. This was not the case for the first Elvia prototype where thicker Copper and glue layers lead to a smaller signal on X readout strips.

The 2D efficiency combining X and Y detection is significantly higher than the product of 1D efficiencies thanks to a strong correlation between the two signal, illustrated in Fig. 5.11. Stable 2D efficiencies above 95% were routinely achieved during several months of operation. Last but not least, spatial resolution was found to be relatively large, of the order of 300 microns. Though misalignments remain in the cosmic bench, several detectors elements can be improved. In particular, a second version has been built very recently without ladders and with an improved mechanical frame to ensure better planarity.

The development of efficient Micromegas offering spatial resolution similar to standard micropattern detectors with a strong reduction of the electronics equipment is opening new fields of applications in fundamental physics and beyond. Benefitting from other progress in robustness (bulk, resistive technology) and production capabilities (transfer of know-how to the Elvia group), such detectors can now be considered for outside lab measurements. Among them, a particularly promising application is the detection of density variations by muon tomography.

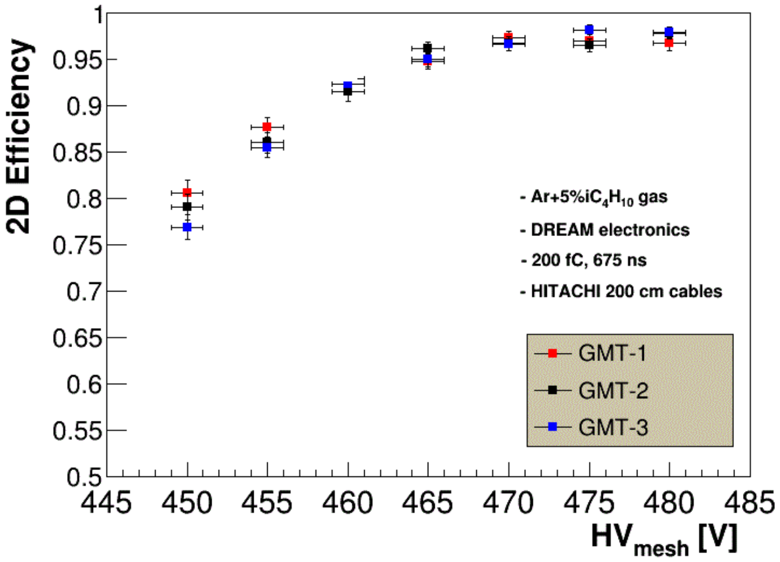

Figure 5.10: *2D efficiency curves for 3 MultiGen 2D detectors, measured in the cosmic test bench.*

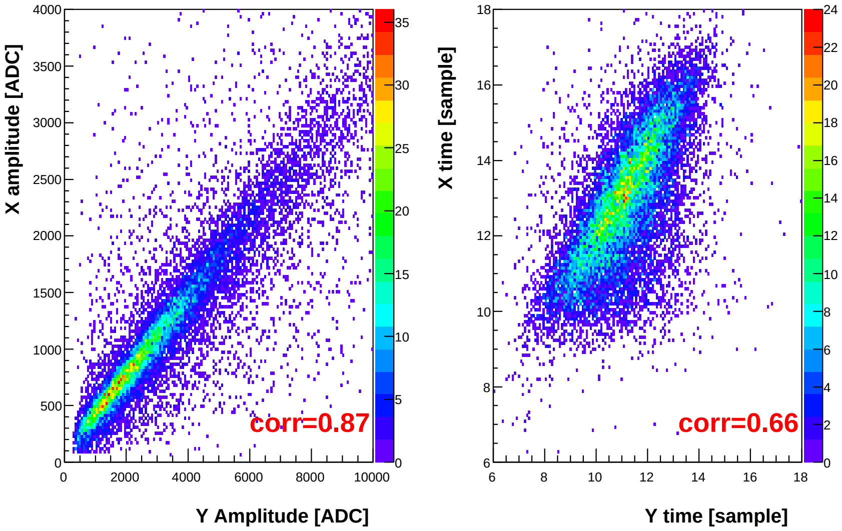

Figure 5.11: *Correlation in cluster amplitude (left) and time (right) for X and Y coordinates of a MultiGen 2D.*

5.4 Applications to muon tomography

5.4.1 Principles of muon tomography

The muon tomography consists in imaging an object or a structure with muons produced in the atmosphere by highly energetic particles. It therefore uses a natural and free radiation, with large scanning capabilities. Muon tomography was shown to be a promising technique for more than 40 years, but in practice the moderate muon flux [4] calls for two partially conflicting constraints:

- large detection areas;
- excellent spatial resolution to extract the most possible information from each particle.

Existing systems based on this technique usually have to sacrifice one of these two criteria, with the consequence to have long scanning time or poor image quality.
Depending on the size and configuration of the studied structure, muon tomography can be operated in deviation mode or in absorption mode, as depicted in Fig. 5.12. If the object is small enough, detectors can be placed on its both sides [5] and the measurement of the upstream and downstream trajectory provide insights of the 3D density structure through the deviation angle due to multiple scattering (see Eq. (3.16)). Examples of angular deviations are given in Table 5.3 for illustration. If the object is too large to be sandwitched by detectors, measurements are performed in only one side, and the flux deficit determines the integrated 2D density in the direction of observation. This mode requires much longer acquisition time, because of the fewer information available and because of the small absorption rate of cosmic muons. Table 5.3 gives some absorption probabilities for different materials and lengths.

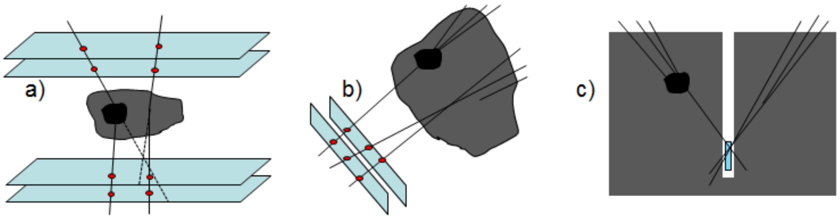

Figure 5.12: *Different modes of the muon tomography: particle deviation (a) and absorption (b and c).*

5.4.2 Selected applications and simulation

Homeland security

The main application of the deviation mode is the homeland security, and more particularly the search for special nuclear material (SNM). Current detection methods are based on artificial radiations (X-rays, gammas or neutrons), which all suffer from several drawbacks: high cost of the whole installation, risks associated to artificial radiations (outside

---

[4] roughly 150 $/\mathrm{m}^2/\mathrm{s}$

[5] vertically, *i.e.* where the muon flux is maximal

Material	Length	θ_0^{param} (mrad)	θ_0^{Geant4} (mrad)	absorption probability
Air	10 m	0.537	0.499 ± 0.001	0.39%
Air	100 m	1.87	1.64 ± 0.001	0.78%
Lead	1 cm	4.64	4.88 ± 0.02	0.49%
Lead	10 cm	15.9	17.7 ± 0.1	2.9%
Water	1 m	5.88	6.08 ± 0.02	4.2%
Rock	1 m	11.6	13.0 ± 0.1	9.5%
Rock	100 m			99%
Rock	1 km			99.999%

Table 5.3: *Typical angular deviations for 4 GeV muons in various materials, calculated from Eq. (3.16) and from Geant4. The table also shows the absorption probability for all cosmic muons obtained with Geant4 simulations.*

and inside containers), possibility to hide SNM with shielding and limited spatial extension of the source. Recently, several projects have therefore emerged to overcome these drawbacks by making use of the free cosmic radiation as a probe. In the US, a collaboration between Los Alamos and the Decision Science company allowed to install in 2012 the very first detection device in the world based on muon tomography. However, the difficulty to manufacture the detectors (drift tubes) prevented this company from building other such devices in the last three years. Similar technologies (multi-wire chambers) are under study in Russia (Protvino), China (Tsinghua), and Italy (INFN), but without any realistic plan of large scale deployment. On the contrary, Canada (AECL/Carleton) and GB (AWE/Manchester) have opted for industrialized technologies (scintillators and single wire chambers respectively), but with poor spatial resolutions.

Multiplexed MPGDs offer both excellent resolution and large production capabilities. Our simulation has shown that it is the only industrial technology of reasonable compactness able to pass the first level of performance required by the American Domestic Nuclear Detection Office (DNDO) [6]. The M-Cube project (Multiplexed Micromegas for Muon tomography), funded by a NRBC-E grant, has initiated the construction of a large cosmic bench demonstrator to scan small containers with a mosaic of MultiGen detectors. The mechanical structure has already been assembled, and the full setup will be built in 2016. Validation tests have already been performed with a smaller setup, as shown in Fig. 5.13, and confirmed the simulation predictions in terms of detection time. On the software side, a partnership has been started in 2015 with the DRT Division of CEA to implement algorithms beyond the simple POCA (Point Of Closest Approach) or Likelihood-based reconstruction [108].

Volcanology

Another application under investigation is the imaging and monitoring of geological structures, and in particular active volcanoes. In this case, the acquisition time is much longer,

---

[6] *i.e.* the detection of 4 kg of Uranium in less than 2 minutes

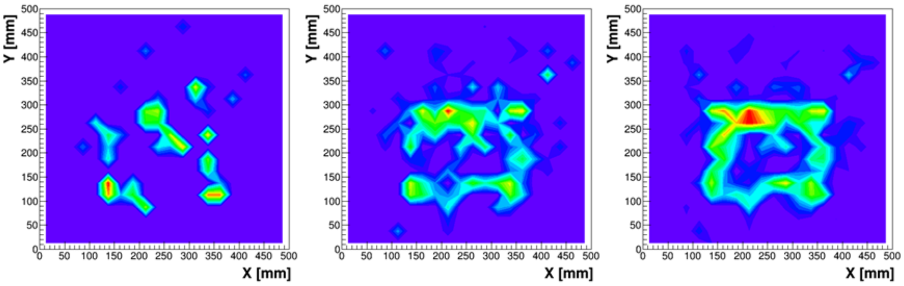

Figure 5.13: *Reconstruction of a Lead square with a small, 50 × 50 cm^2 muon tomography setup after 2 (left), 10 (middle) and 20 (right) minutes.*

up to several months. Several teams in the world have already performed such measurements in the recent years, and are able to reconstruct 2D density profiles of several volcanoes. One of the leading teams in the world, the Diaphane collaboration between IPG-Paris and IPN-Lyon, has designed large muon telescopes made with layers of 5 cm wide scintillators. Fig 5.14 shows the result of a three-month campaign made at La Soufrière, in Guadeloupe. In terms of performance, a telescope with multiplexed Micromegas can *a priori* enhance the angular resolution by at least a factor 10, while being more compact, improving background rejection and increasing the acceptance for open sky simultaneous measurements. On the other hand, several challenges should be addressed, like the autonomous operation, the control of electromagnetic noise, the time stability with large temperature, humidity and pressure variations. To face all these issues and prove the feasibility of such an instrument, a small telescope built with 4 MultiGen 2D detectors was designed and installed near the water tower of the CEA-Saclay center. The instrument was equipped with a mini PC (Hummingboard card) for the acquisition and the data storage, as well as the HV control and monitoring. These high voltages were provided by 12 V miniature modules from CAEN (A7501) integrated on a card designed at Irfu. The 4 detectors were readout with a single FEU from the Clas12/Dream electronics used in its

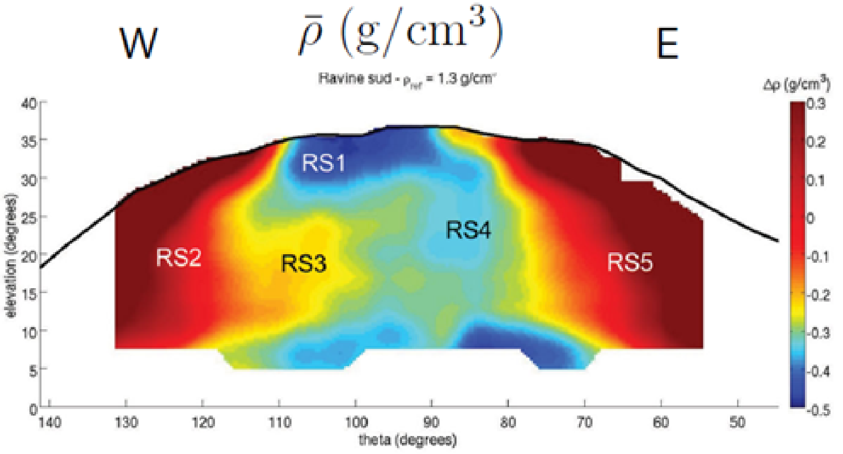

Figure 5.14: *Muon tomography of la Soufrière de Guadeloupe with a scintillator telescope built and operated by the Diaphane collaboration ([109] and references therein).*

self-triggering mode to avoid the presence of external scintillators. The whole consumption of the telescope yielded only 25-30 W, including about 16 W for the FEU. A small B20 bottle with a non flamable Argon-Isobutane-CF$_4$ (95-2-3) mixture ensured an autonomy of 3 months with a limited 1 L/h gas circulation. The telescope was AC powered during the first half of the experiment, and later plugged on a battery with recharging solar boards to check the full autonomy of the instrument.

The extrapolation of muon tracks to the water tower plane gives direct access to its *muography*, as shown in Fig. 5.15 (left). In spite of the small size of the telescope, several details of its architecture are visible, as well as the presence of water in the lower part of the tank. An absorption up to 50% is measured, corresponding to roughly 10 m of water. A dynamic monitoring of the water level was also performed, by counting the number of muons passing through the tank. As the natural muon flux varies with time, this number was normalized by the open sky flux measured in parallel thanks to the large telescope acceptance. As shown in Fig. 5.15 (right), a strong correlation was revealed with the water height, a feature which is particularly promising for volcanology.

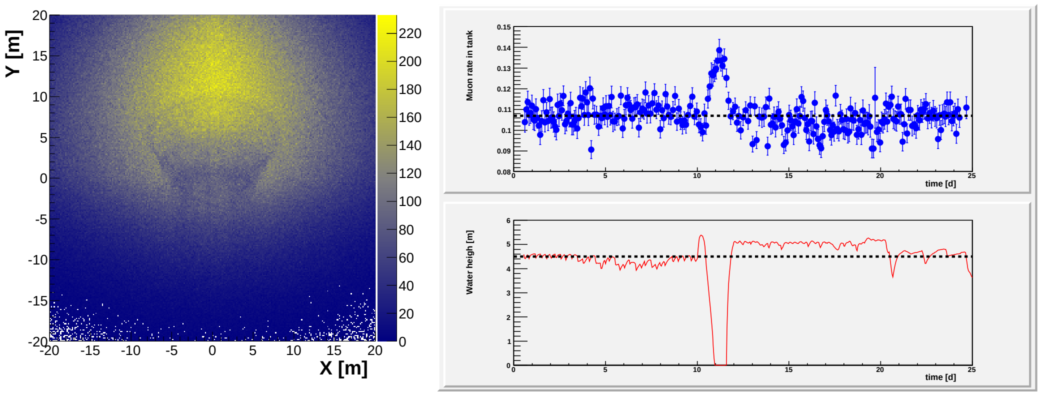

Figure 5.15: *(Left): muography of the Saclay water tower, obtained with 4 weeks of data. (Right): time variations of the muon flux in the tank normalized to the outside flux, as well as the water height.*

After 2 months of operation, the telescope was moved closer to the water tower in order to obtain a second projection. Though it is not clear whether 3D images can be extracted from the available data, we observed a long (3 days) draining of the tower which enables us to image it with and without its water, as seen in Fig. 5.16. During the experiment, temperature variations larger than 30 °C strongly affected the gain of the detectors, and thus the trigger efficiency. A temperature feedback was successfully implemented on the HV, with coefficients close to 1 V/°C. As expected from ideal gas law, the relative variation with the pressure was found to be roughly 3 times smaller, and was not corrected for. In future experiments however, a USB barometer will be added to the setup to further improve its overall stability.

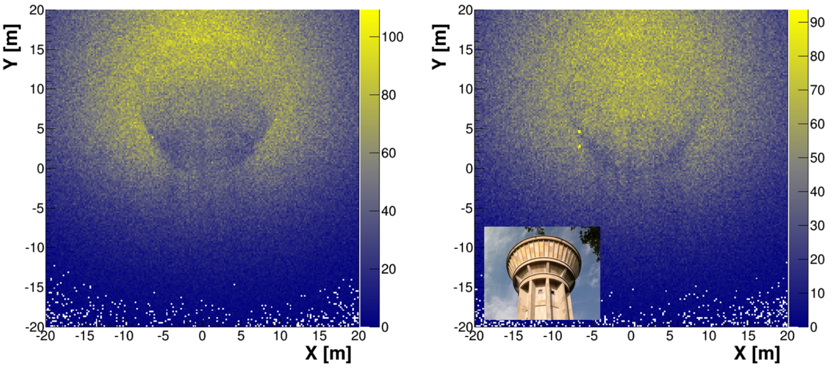

Figure 5.16: *Muography obtained before (left) and during (right) the draining of the water tower. Both images correspond to roughly 3 days of data.*

Archeology

The telescope described above can be used to scan various structures. In particular, archeologists have already expressed their interest to operate such a device in prehistoric sites, aiming at detecting holes in rocks for conservation. A potential test site has been identified with the LRMH [7], namely the Roc-Aux-Sorciers rock shelter from mid Magdalenian age. For archeological prospection of soil, such a telescope may not be adapted in most of the configurations. However, cylindrical scanners for borehole insertion may be developed to image the neighbouring soil, benefitting either from the cylindrical Micromegas developed for the Clas12 and the Asacusa experiments, or from small radius TPC designed for the Minos project. Fig. 5.17 shows a simulation of a 30 cm diameter, 50 cm long scanner located 8-meter deep in the soil with a homogeneous density of $2.4\,\mathrm{g/cm^3}$. A $40{\times}40{\times}40\,\mathrm{cm^3}$ air cavity has been added 2.5 meters away. The cavity appears as an excess of muons after approximately a week of data.

Mining exploration

The possibility to use small radius detectors with low consumption for soil inspection has also triggered some interest for mining exploration. In this case, the radius should be even smaller to fit in standard mining boreholes, typically 10 to 15 cm diameter. Another difficulty consists in operating the detector at much greater depths, *i.e.* a few hundreds meters, where the muon flux is strongly attenuated, as illustrated in Fig. 5.18.

The ScanPyramid mission

Last but not least, contacts have been established with the HIP Institute coordinating the ScanPyramid mission. Muon telescopes may be deployed in the coming months on

---

[7] Laboratoire de Recherches des Monuments Historiques

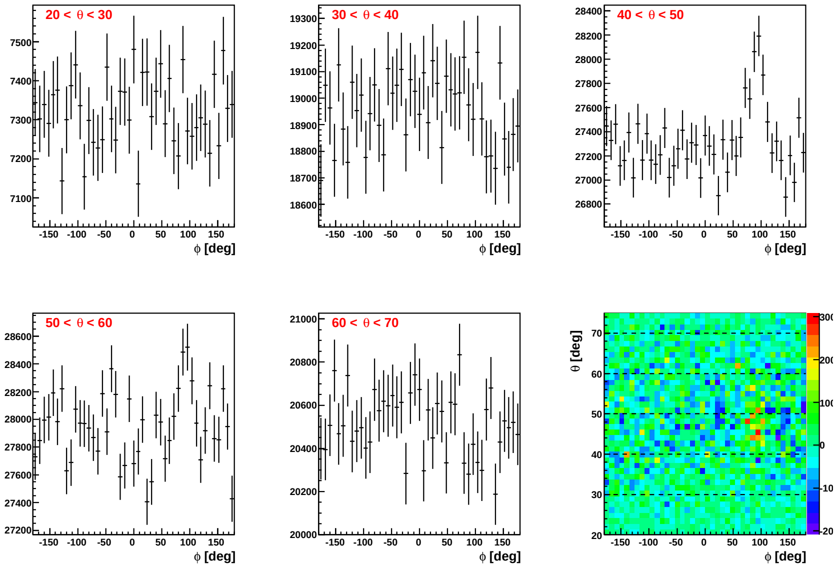

Figure 5.17: *Simulation with Cry/Geant4 of a muon flux measurement with a* $40 \times 40 \times 40\, cm^3$ *air cavity in soil. The first five plots represent the muon number as a function of the azimutal angle for different polar angles from the detector. The last plot displays the fluctuations of the muon flux around the* ϕ *average. The simulation corresponds to 2 weeks of data.*

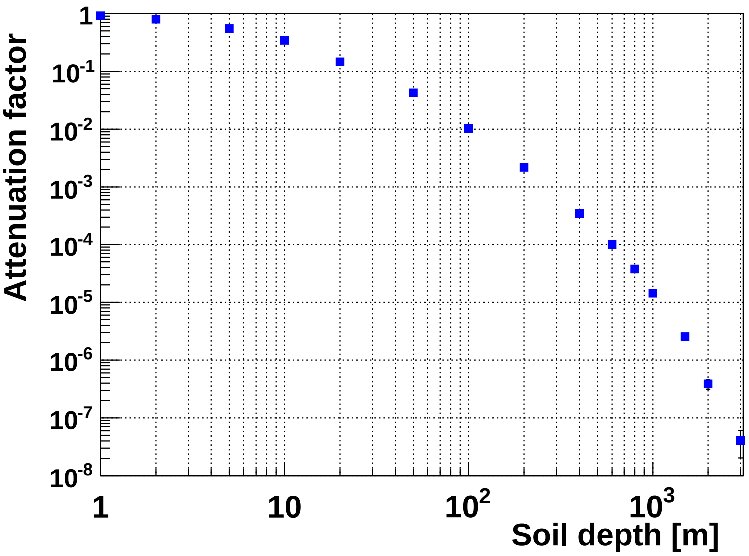

Figure 5.18: *Simulation with Cry/Geant4 of the muon flux attenuation as a function of the depth in soil, taken as limestone rock.*

the Giza site to look for unknown corridors or chambers in Khufu and Khafre pyramids. Telescopes would be installed outdoors to complement Japanese instruments located in the

Queen's Chamber. A particularly promising site would be the North-East edge which hosts a known chamber that could be linked to corridors used during the building of the pyramid. Simulations have already determined the optimal observation site, taking into account the solid angle, the absorption factor of muons in the pyramid as well as the azimutal angle. These simulations show in particular that cavities of the size of the Bob's Chamber could be detected within a few weeks of acquisition. On the technical side, challenging tests are currently ongoing to check the resistance of the whole telescope (detectors, electronics, battery, etc.) to temperatures close to 50 degrees.

Bibliography

[1] Y. Giomataris *et al.*, Nucl. Instrum. Methods A **376** (1996) 29

[2] Y. Giomataris, Nucl. Instrum. Methods A **419** (1998) 239

[3] See for example the excellent book of F. Sauli, Gaseous Radiation Detectors, Cambridge University Press (2014)

[4] H. Bethe, Ann. Phys., **397** (1930), 325

[5] H. Bethe, Zeit. Phys., **76** (1932), 293

[6] Particle Data Group, J. Beringer *et al.*, Phys. Rev. D**86** (2012), 010001

[7] L.D. Landau, J. Exp. Phys. (USSR), **8** (1944), 201

[8] see for example R. Talman, Nucl. Instrum. Methods **159** (1979) 189, and references therein

[9] W.W.M. Allison, J.H Cobb, Ann. Rev. Nucl. Part. Sci. 30 (1980), 253

[10] I.B. Smirnov, Nucl. Instrum. Methods A **554** (2005) 474

[11] P. Auger, J. Phys. Radium **6** (1925) 205

[12] F. M. Penning, Naturwissenschaften, Volume **15**, (1927) 818

[13] F. M. Penning, Zeit. Phys. **46** (1928) 335

[14] W. P. Jesse and J. Sadauskis, Phys. Rev. **88** (1952) 417

[15] N. E. Bradbury, Phys. Rev. **44** (1933) 883

[16] M. A. Harrison and R. Geballe, Phys. Rev. **91** (1953) 1

[17] J. C. Maxwell, Philosophical Magazine, 4th series, **19** (1860) 19

[18] P. Langevin, C. R. Acad. Sci. (Paris) **146** (1908) 530

[19] E. B. Wagner *et al.*, J. Chem. Phys. **47** (1967) 3138

[20] H. R. Skullerud, J. Phys. B **2** (1969) 696

[21] J. H. Parker and J. J. Lowke, Phys. Rev. **181** (1969) 290

[22] P. Colas *et al.*, Nucl. Instrum. Methods A **478** (2002) 215

[23] by courtesy of M. Vandenbroucke

[24] C. Ramsauer, Ann. Phys. **369** (1921) 513

[25] L. Huxley and R. Crompton, *The diffusion and drift of electrons in gases* (1974), John Wiley & sons, New York

[26] R. Veenhof, MPGD tutorial, Saclay, 2015

[27] S.F. Biagi, Nucl. Instrum. Methods A **421** (1999) 234

[28] http://nl.lxcat.net/home/

[29] P. Konczykowski *et al.*, Nucl. Instrum. Methods A **612** (2010) 274

[30] J. S. Townsend, Phil. Mag. **1** (1901) 198

[31] W.H. Furry, Phys. Rev. **52** (1937) 569

[32] H.S. Snyder, Phys. Rev. **72** (1947) 181

[33] R.A. Wijsman, Phys. Rev. **75** (1949) 833

[34] S.C. Curran *et al.*, Phil. Mag. **40** (1949) 929

[35] W. Legler, Z. Naturforsch. **16**a (1961) 253

[36] J. Byrne, Proc. Roy. Soc. Edinburgh A**66** (1962) 33

[37] A. Lansiart and J.P. Morucci, J. Phys. Radium **23** suppl. no. 6 (1962) 102A

[38] A.H. Cookson and T.J. Lewis, Brit. J. Appl. Phys. **17** (1966), 1473

[39] W. Legler, Brit. J. Appl. Phys. **18** (1967), 1275

[40] G. D. Alkhazov, Nucl. Instrum. Methods **89** (1970) 155

[41] T. Zerguerras *et al.*, Nucl. Instrum. Methods A **772** (2015) 76

[42] W. Shockley, J. Appl. Phys **9** (1938) 635

[43] S. Ramo, Proceedings of the IRE **27** (1939) 584

[44] R. Veenhof, Nucl. Instrum. Methods A **419** (1998) 726

[45] M. Vandenbroucke, *Development and characterization of MPGDs for intense beams of hadrons*, PhD. thesis, IRFU-12-08-T (2012)

[46] D. Thers *et al.*, Nucl. Instrum. Methods A **469** (2001) 133

[47] D. Thers, *Développement du détecteur gazeux Micromegas pour l'expérience Compass*, Thèse de Doctorat, Univ. Blaise Pascal, 7 décembre 2000

[48] I. Giomataris *et al.*, Nucl. Instrum. Methods A **560** (2006) 405

[49] S. Andriamonje *et al.*, JINST **5** (2010) P02001

[50] M.S. Dixit *et al.*, Nucl. Instrum. Methods A **518** (2004) 721

[51] T. Alexopoulos *et al.*, Nucl. Instrum. Methods A **640** (2011) 110

[52] P. Baron *et al.*, IEEE Trans. Nucl. Sci. Vol **55** (2008) 1744

[53] V. Radeka, Detector signal processing, 2014 IEEE Nuclear Science Symposium and Medical Imaging Conference

[54] by courtesy of É. Delagnes

[55] S. Anvar *et al.*, IEEE Nuclear Science Symposium Conference Record (2011), 745

[56] C. Flouzat *et al.*, Dream: a 64-channel Front-end Chip with Analogue Trigger Latency Buffer for the Micromegas Tracker of the Clas12 Experiment, TWEPP conference (2014)

[57] P. Baron *et al.*, Dream: A front end Asic for Clas12 detector, User Manual

[58] F. Sauli, Principles of operation of multiwire proportional and drift chambers, lecture in the academic training programme of Cern

[59] J. Derré *et al.*, Nucl. Instrum. Methods A **449** (2000) 314

[60] T. Zerguerras *et al.*, Nucl. Instrum. Methods A **608** (2009) 397

[61] P.I. Gutierrez, Characterization of microbulk detectors in Argon and Neon mixtures, Café du Sédi (Irfu), 2011

[62] S. Cebrian *et al.*, JINST **8** (2013) P01012

[63] Y. Wei *et al.*, IEEE Trans. Nucl. Sci. Vol **60** (2013) 3008

[64] F. Kuger *et al.*, http://dx.doi.org/10.1016/j.nima.2015.11.011

[65] G. Charles, *Mise au point de détecteurs Micromegas pour le spctromètre Clas12 au Laboratoire Jefferson*, PhD. thesis, IRFU-13-08-T (2013)

[66] U. Fano, Phys. Rev. **72** (1947) 26

[67] P. Bhattacharya *et al.*, Nucl. Instrum. Methods A **732** (2013) 208

[68] P. Abbon *et al.*, Nucl. Instrum. Methods A **577** (2007) 455

[69] T. Alexopoulos *et al.*, Nucl. Instrum. Methods A **617** (2010) 161

[70] Atlas Technical Design Review, CERN-LHCC-2013-006 (2013), page 56-57

[71] S. Procureur, Simulation of Micromegas detectors for the Clas12 central tracker, CLAS-note 2007-004 (2007)

[72] F. Georges, Détecteurs Micromegas pour Clas12, rapport de stage de Centrale (2015)

[73] S. Procureur *et al.*, Nucl. Instrum. Methods A **688** (2012) 75

[74] G. Charles, Nucl. Instrum. Methods A **718** (2013) 414

[75] J. Galan *et al.*, JINST **8** (2013) P04028

[76] M. Chefdeville, Resistive Micromegas for sampling calorimetry, 13th Pisa meeting on advanced detectors (2015)

[77] F. Thibaud, *Développement de détecteurs Micromegas pixellisés pour les hauts flux de particules et évaluation de la contribution diffractive à la leptoproduction de hadrons à Compass*, PhD. thesis, IRFU-14-17-T (2014)

[78] S. Procureur, DVCS event reconstruction for Clas12 with Socrat, CLAS-note 2012-006 (2012)

[79] http://www.cern.ch/minuit

[80] R.E. Kalman, J. Basic Eng. **82** (1960) 35

[81] P. Billoir, Nucl. Instrum. Methods **225** (1984) 352

[82] P. Billoir, R. Fruhwirth and M. Regler, Nucl. Instrum. Methods A **241** (1985) 115

[83] R. Fruhwirth, Nucl. Instrum. Methods A **262** (1987) 444

[84] E.J. Wolin and L.L. Ho, Nucl. Instrum. Methods A **329** (1993) 493

[85] G. Kitagawa, Comput. Math. Appl. **18** (1989) 503

[86] R. Fruhwirth, Comp. Phys. Comm. **100** (1997) 1

[87] M. Ohlsson, C. Peterson and A. Yuille, Comp. Phys. Comm. **71** (1992) 77

[88] R. Fruhwirth and A. Strandlie, Comp. Phys. Comm. **120** (1999) 197

[89] S. Procureur, Socrat: a SOftware for Clas12 Reconstruction And Tracking, CLAS-note 2008-015 (2008)

[90] B. Mecking, Nucl. Instrum. Methods **203** (1982) 299

[91] V. Blobel, Nucl. Instrum. Methods A **566** (2006) 5

[92] R. Fruhwirth *et al.*, Comp. Phys. Comm. **96** (1996) 189

[93] S. Agostinelli *et al.*, Nucl. Instrum. Methods A **506** (2003) 250

[94] T. Sjöstrand, S. Mrenna and P. Skands, JHEP05 (2006) 026, Comp. Phys. Comm. 178 (2008) 852

[95] F. Paschen, Annalen der Physik **273** (1889) 69-96

[96] J. S. Townsend, *Electricity in gases*, Clarendon Press, Oxford (1915)

[97] H. Raether, *Electron avalanches and breakdown in gases*, London Butterworths (1964)

[98] J. M. Meek, Phys. Rev. **57** (1940), 722

[99] W. Rogowski, Arch. f. Elek. **20** (1928), 99

[100] S. Banerjee, CHEP2009, http://geant4.cern.ch/results/talks/CHEP09/CHEP09-validation.pdf

[101] S. Procureur *et al.*, Nucl. Instrum. Methods A **621** (2010) 177

[102] F. Sauli *et al.*, Nucl. Instrum. Methods A **386** (1997) 531

[103] S. Kane *et al.*, Nucl. Instrum. Methods A **515** (2003) 261

[104] S. Procureur *et al.*, Nucl. Instrum. Methods A **659** (2011) 91

[105] G. Charles *et al.*, Nucl. Instrum. Methods A **648** (2011) 174

[106] B. Moreno *et al.*, Nucl. Instrum. Methods A **654** (2011) 135

[107] X. Yue *et al.*, arXiv:1508.03704

[108] L. J. Schultz *et al.*, IEEE Trans. Imag. Proc. Vol **16** (2007) 1985

[109] J. Marteau *et al.*, Nucl. Instrum. Methods A **695** (2012) 23